H2020 CleanSky 2
Grant Agreement n. 785419

Scientific Publication Booklet

Document version: draft

Document date: 30 June 2021

Lead beneficiary: UNICAMPANIA

Dissemination level: Public

Contribution to: WP 9

Project acronym: LABOR

Project full title: Lean robotized AssemBly and cOntrol of composite aeRostructures

Grant agreement n.: 785419

Call: H2020-CS2-CFP06-2017-01

Starting date: 1 March 2018

Duration in months: 40

Web site: www.labor-project.eu

Table of Contents

Executive Summary

This booklet includes all scientific publications produced within the LABOR project and listed in the following table.

Identifier	Publication Title	Main Author	Title of the periodical or the series	Number, or Date	Relevant pages	Permanent identifiers [1] (if available)	Is/Will open access [2] provided?
P01	Safety in human-multi robot collaborative scenarios: a trajectory scaling approach	M. Lippi, A. Marino	12th IFAC Symposium on robot control	August 2018	190-196	DOI: 10.1016/j.ifacol.2018.11.540	Yes (green)
P02	Smart Inspection Tools in robotized aircraft panels manufacturing	A. Bruni, E. Concettoni, C. Cristalli, M. Nisi	IEEE International workshop on Metrology for Aerospace	June 2019	629-634	DOI: 10.1109/MetroAeroSpace.2019.8869690	Yes (green)
P03	A fuzzy inference approach to control robot speed in human-robot shared workspaces	A. Campomaggiore, M. Costanzo, G. Lettera, C. Natale	6th International Conference On Informatics in Control, Automation and Robotics	July 2019	78-87	DOI: 10.5220/0007838700780087	Yes
P04	Robotica lean e adattativa per l'aeronautica	C. Cristalli	Platinum	n. 33 2019	102	ISSN: 2038-2596	Yes
P05	A Multimodal Perception System for Detection of Human Operators in Robotic Work Cells	M. Costanzo, G. De Maria, G. Lettera, C. Natale, D. Perrone	2019 IEEE International Conference on Systems, Man, and Cybernetics	October 2019	702-709	ISBN: 978-1-7281-4568-6/19 DOI: 10.1109/SMC.2019.8914519	Yes (green)

1 A permanent identifier should be a persistent link to the published version full text if open access or abstract if article is pay per view) or to the final manuscript accepted for publication (link to article in repository).
2 Open Access is defined as free of charge access for anyone via Internet. Please answer "yes" if the open access to the publication is already established and also if the embargo period for open access is not yet over but you intend to establish open access afterwards.

Identifier	Publication Title	Main Author	Title of the periodical or the series	Number, or Date	Relevant pages	Permanent identifiers [1] (if available)	Is/Will open access [2] provided?
P06	Human–Robot Interaction for Improving Fuselage Assembly Tasks: A Case Study	E. Laudante, A. Greco, M. Caterino, M. Fera	Applied Science	10, 2020	5757	DOI: 10.3390/app10175757	Yes
P07	Robotized assembly and inspection of composite fuselage panels: the LABOR project approach	M. Caterino, P. Chiacchio, C. Cristalli, M. Fera, G. Lettera, C. Natale, M. Nisi	IOP Conf. Series: Materials Science and Engineering 1024	2021	012019	DOI: 10.1088/1757-899X/1024/1/012019	Yes
P08	A multimodal approach to human safety in collaborative robotic workcells	M. Costanzo, G. De Maria, G. Lettera and C. Natale	IEEE Transactions on Automation Science and Engineering	2021		DOI: 10.1109/TASE.2020.3043286	Yes (Green)
P09	Planning of efficient trajectories in robotized assembly of aerostructures exploiting kinematic redundancy	F. Storiale, E. Ferrentino, P. Chiacchio	Manufacturing Review	8, 2021		DOI: 10.1051/mfreview/2021007	Yes

The publication record starts with papers containing methodological approaches but, as soon as the project has developed in terms of hardware production, papers with experimental results have been produced. A good balance between journal (3), magazine (1) and conference (5) papers characterizes the publication list.

The rest of the document contains the post-print manuscripts of all papers, all compliant with the EU Open Access requirement (4 green and 5 gold).

Safety in human-multi robot collaborative scenarios: a trajectory scaling approach

Article *in* IFAC-PapersOnLine · January 2018

DOI: 10.1016/j.ifacol.2018.11.540

2 authors:

Martina Lippi
Università Degli Studi Roma Tre

Alessandro Marino
Università degli Studi di Salerno

Safety in human-multi robot collaborative scenarios: a trajectory scaling approach

Martina Lippi, Alessandro Marino

University of Salerno, Via Giovanni Paolo II, 132, 84084, Salerno (SA), Italy (email: {mlippi,almarino}@unisa.it)

Abstract:
In this paper, a strategy to handle the human safety in a multi-robot scenario is devised. In the presented framework, it is foreseen that robots are in charge of performing any cooperative manipulation task which is parameterized by a proper task function. The devised architecture answers to the increasing demand of strict cooperation between humans and robots, since it equips a general multi-robot cell with the feature of making robots and human working together. The human safety is properly handled by defining a safety index which depends both on the relative position and velocity of the human operator and robots. Then, the multi-robot task trajectory is properly scaled in order to ensure that the human safety never falls below a given threshold which can be set in worst conditions according to a minimum allowed distance. Simulations results are presented in order to prove the effectiveness of the approach.

Keywords: Human-robot collaboration. Trajectory scaling. Multi-robot systems.

1. INTRODUCTION

The close cooperation of humans and robots is a highly desirable feature since it allows to benefit of the outperforming reasoning capabilities of humans and the extreme precision and strength of robots. However, it is straightforward to recognize that the human safety is of the utmost importance in such a scenario which requires, at least, the robots to be controlled in such a way to not harm human operators Haddadin et al. (2009). In this regard, initial regulations about human safety with respect to industrial robots can be found in the American ANSI/RIA R15.06, in the European EN 775 or in the more general international standard ISO 10218 and the technical specification document ISO/TS 15066. In detail, the latter exactly focuses on human-robot collaborative scenarios and envisages four possible safe interactions:

(1) safety-rated monitored stop, i.e. robots are required to stop when humans enter the working area;
(2) hand guiding, i.e. robots are required to follow human manual guidance;
(3) speed and separation monitoring, i.e. robots have to keep a minimum safety distance from operators;
(4) power and force limiting, i.e. robots are required to mitigate human harm in the case of impact.

It is clear that interactions 3 and 4 involve integrating the robot autonomous task with human safety requirements. As highlighted in Robla-Gómez et al. (2017), this also requires the inclusion of different sensors whose features depend on the nature of the interaction: from sensors for detecting the presence of human operators for collision prevention, e.g. motion capture systems, range sensors or artificial vision systems as in Flacco et al. (2012), to sensors for assessing force exchange when an impact occurs, e.g. force or tactile sensors as in Cirillo et al. (2016).

Although power and force limiting is crucial in the case of physical human-robot interaction where contact is unavoidable, distance monitoring would be more suitable for pure coexistence in the working area. In the latter scenario, it becomes relevant to quantify the level of human safety, looking at the overall structure of the manipulator as a source of danger to humans, so that the robots behaviour can be adapted accordingly. An index based on distance, velocity and inertial contributions is proposed in Kulić and Croft (2006) and is evaluated for the nearest point between each link and the operator; then, such danger index is exploited to generate a virtual repulsive force according to artificial potential field theory in Khatib (1985). The study presented in Lacevic et al. (2013) also focuses on defining an assessment of human safety which is now based on velocity and distance terms and is extended to the overall structure of the manipulator by a proper integration along each link; a gradient-based technique is then adopted to drive the manipulator. The previous approaches rely on pursuing evasive actions to increase safety, however, in industrial settings, it is generally recommended to follow the desired task path without deviating from it. This guideline is broadened in Zanchettin et al. (2016) where robot velocity is modulated in accordance with the distance from the operator while preserving the nominal task path. A further approach is presented in Liu and Tomizuka (2016) and Kimmel and Hirche (2017) where the safe interaction problem is modeled as an invariance control problem, i.e. it is based on defining a safe set of robot states for which no collision occurs and then on making this set invariant. The previous works show how research regarding human-robot interaction and, in particular, human safety is a hot topic; however, to the best of authors' knowledge, the case of interaction between human operators and strictly cooperative robot systems has not yet been investigated. In this context, human safety must certainly remain the highest priority task, but at the same time the coordination of the robot team must be managed.
Motivated by these considerations, this study presents a general solution for handling the human safety in a scenario composed by multiple cooperative robots. Starting

[1] Authors are in alphabetical order

[2] The research leading to these results has received funding from the European Communitys H2020 Program under grant agreement n. 785419 (EU.3.4.5.4. - ITD Airframe project LABOR - Lean robotized AssemBly and cOntrol of composite aeRostructures).

from the definition of a safety index depending on the human operator's state and on the state of a generic point of the robot structure, first the safety associated to the whole robot and, then, to whole team are computed. This safety measure is adopted to properly modify the robots trajectories in order to preserve the cooperative task and so as to not violate the safety requirements. However, because of the constraint represented by the task itself, this might result in a too restrictive strategy that might lead to the violation of the established safety requirements. If this case occurs, the task is interrupted and an impedance-based strategy is adopted; the task is then recovered when the safety conditions are restored.

The devised solution presents several desirable features with respect to other solutions cited above: (i) it works for general expressions of the safety index, (ii) it explicitly takes into account the multi-robot nature of the task, (iii) it does not modify the task path or require the task to be aborted unless if strictly necessary.

The paper is organized as follows. Section 2 introduces the mathematical background and the problem setting. In Section 3, the adopted safety index is defined and analyzed in detail, while in Section 4 this index is exploited to define a safe human-robot interaction strategy. Finally, numerical simulations and conclusions are presented in Sections 5 and 6, respectively.

2. MATHEMATICAL BACKGROUND

In this paper, we consider a multi-robot work-cell in which human and robots are allowed to share the same area. In particular, the cell is composed by N *worker* robots which execute the main work the cell is aimed to.

We assume that robots are manipulators eventually mounted on a mobile base whose general model is

$$\boldsymbol{M}_i(\boldsymbol{q}_i)\ddot{\boldsymbol{q}}_i+\boldsymbol{C}_i(\boldsymbol{q}_i,\dot{\boldsymbol{q}}_i)\dot{\boldsymbol{q}}_i+\boldsymbol{F}_i\dot{\boldsymbol{q}}_i+\boldsymbol{g}_i(\boldsymbol{q}_i)=\boldsymbol{\tau}_i-\boldsymbol{J}_i^{\mathrm{T}}(\boldsymbol{q}_i)\boldsymbol{h}_i \quad (1)$$

where $\boldsymbol{q}_i \in \mathbb{R}^{n_i}$ ($\dot{\boldsymbol{q}}_i$, $\ddot{\boldsymbol{q}}_i$) is the joint position (velocity, acceleration) vector, $\boldsymbol{\tau}_i \in \mathbb{R}^{n_i}$ is the joint torque vector, $\boldsymbol{M}_i(\boldsymbol{q}_i) \in \mathbb{R}^{n_i \times n_i}$ is the symmetric positive definite inertia matrix, $\boldsymbol{C}_i(\boldsymbol{q}_i, \dot{\boldsymbol{q}}_i) \in \mathbb{R}^{n_i \times n_i}$ is the centrifugal and Coriolis terms matrix, $\boldsymbol{F}_i \in \mathbb{R}^{n_i \times n_i}$ is the matrix modeling viscous friction, $\boldsymbol{g}_i(\boldsymbol{q}_i) \in \mathbb{R}^{n_i}$ is the vector of gravity terms, $\boldsymbol{J}_i(\boldsymbol{q}_i) \in \mathbb{R}^{p \times n_i}$ is the manipulator Jacobian matrix, and $\boldsymbol{h}_i \in \mathbb{R}^p$ is the vector of interaction forces between the robot's end-effector and the environment. Let $\boldsymbol{q}_{r,i}(t) \in \mathbb{R}^{n_i}$ ($\dot{\boldsymbol{q}}_{r,i}(t)$, $\ddot{\boldsymbol{q}}_{r,i}(t)$) be the joint position (velocity, acceleration) reference of the ith robot, the following assumption is made.

Assumption 1. Each robot is equipped with an inner motion control loop which guarantees tracking of a reference joint trajectory, i.e. $\boldsymbol{q}_{r,i} \approx \boldsymbol{q}_i$ ($\dot{\boldsymbol{q}}_{r,i} \approx \dot{\boldsymbol{q}}_i$, $\ddot{\boldsymbol{q}}_{r,i} \approx \ddot{\boldsymbol{q}}_i$).

This assumption is realistic for all commercial platforms and makes the devised solution suitable also for off-the-shelf robotic platforms for which the low level control layer is generally not made accessible to directly set the $\boldsymbol{\tau}_i$ input in (1).

The second order kinematic relationship is such as

$$\ddot{\boldsymbol{x}}_i = \boldsymbol{J}_i(\boldsymbol{q}_i)\ddot{\boldsymbol{q}}_i + \dot{\boldsymbol{J}}(\boldsymbol{q}_i)\dot{\boldsymbol{q}}_i = \boldsymbol{J}_i(\boldsymbol{q}_i)\boldsymbol{y}_i + \dot{\boldsymbol{J}}(\boldsymbol{q}_i)\dot{\boldsymbol{q}}_i \quad (2)$$

where $\boldsymbol{x}_i = \left[\boldsymbol{p}_i^{\mathrm{T}}, \boldsymbol{\phi}_i^{\mathrm{T}}\right]^{\mathrm{T}} \in \mathbb{R}^p$ is the end-effector configuration of the ith manipulator with respect to the world frame expressed in terms of position $\boldsymbol{p}_i$ and orientation $\boldsymbol{\phi}_i$, and $\boldsymbol{y}_i = \ddot{\boldsymbol{q}}_i$ is the input of the assumed virtual model. For the sake of notation compactness, the dependence of $\boldsymbol{J}_i$ from its parameter $\boldsymbol{q}_i$ is generally omitted in the following.

For the purpose of the overall description of the cell, let us introduce the collective vectors

$$\begin{aligned} \boldsymbol{x} &= \left[\boldsymbol{x}_1^{\mathrm{T}},\, \boldsymbol{x}_2^{\mathrm{T}},\, \ldots,\, \boldsymbol{x}_N^{\mathrm{T}}\right]^{\mathrm{T}} \in \mathbb{R}^{Np} \\ \boldsymbol{q} &= \left[\boldsymbol{q}_1^{\mathrm{T}},\, \boldsymbol{q}_2^{\mathrm{T}},\, \ldots,\, \boldsymbol{q}_N^{\mathrm{T}}\right]^{\mathrm{T}} \in \mathbb{R}^{n} \\ \boldsymbol{J}(\boldsymbol{q}) &= \mathrm{diag}\{\boldsymbol{J}_1(\boldsymbol{q}_1), \ldots, \boldsymbol{J}_N(\boldsymbol{q}_N)\} \in \mathbb{R}^{Np \times n} \end{aligned} \quad (3)$$

where $n = \sum_i n_i$.

In what follows, with $\boldsymbol{O}_m$ and $\boldsymbol{I}_m$ we denote the null and identity matrices in $\mathbb{R}^{m\times m}$, respectively, and with $\boldsymbol{0}_m$ we denote the column vector in $\mathbb{R}^m$ with all zero elements.

2.1 Problem setting

It is assumed that the cooperative task assigned to robots is defined by means of a task function $\boldsymbol{\sigma} = \boldsymbol{\sigma}(\boldsymbol{x}) \in \mathbb{R}^m$ as

$$\boldsymbol{\sigma} = \boldsymbol{J}_\sigma \boldsymbol{x}, \quad \dot{\boldsymbol{\sigma}} = \boldsymbol{J}_\sigma \dot{\boldsymbol{x}}, \quad \ddot{\boldsymbol{\sigma}} = \boldsymbol{J}_\sigma \ddot{\boldsymbol{x}} \quad (4)$$

being $\boldsymbol{J}_\sigma \in \mathbb{R}^{m\times Np}$ the task Jacobian matrix. A flexible formulation for the task function $\boldsymbol{\sigma}$ is given by the absolute-relative variables as in Basile et al. (2012). In detail, the absolute variables define the position and orientation of the centroid of the end-effector configurations:

$$\boldsymbol{\sigma}_1 = \frac{1}{N}\sum_{i=1}^{N} \boldsymbol{x}_i = \boldsymbol{J}_{\sigma_1}\boldsymbol{x} \quad (5)$$

with $\boldsymbol{J}_{\sigma_1} = \frac{1}{N}\boldsymbol{1}_N^{\mathrm{T}} \otimes \boldsymbol{I}_p \in \mathbb{R}^{p\times Np}$, while the relative variables represent the team formation:

$$\boldsymbol{\sigma}_2 = [(\boldsymbol{x}_N - \boldsymbol{x}_{N-1})^{\mathrm{T}} \ldots (\boldsymbol{x}_2 - \boldsymbol{x}_1)^{\mathrm{T}}]^{\mathrm{T}} = \boldsymbol{J}_{\sigma_2}\boldsymbol{x} \quad (6)$$

with

$$\boldsymbol{J}_{\sigma_2} = \begin{bmatrix} -\boldsymbol{I}_p & \boldsymbol{I}_p & \boldsymbol{O}_p & \ldots & \boldsymbol{O}_p \\ \boldsymbol{O}_p & -\boldsymbol{I}_p & \boldsymbol{I}_p & \ldots & \boldsymbol{O}_p \\ \vdots & & \ddots & & \vdots \\ \boldsymbol{O}_p & \ldots & \boldsymbol{O}_p & -\boldsymbol{I}_p & \boldsymbol{I}_p \end{bmatrix} \in \mathbb{R}^{(N-1)p\times Np} \quad (7)$$

Hence, in virtue of (5) and (6), the task function in (4) is

$$\boldsymbol{\sigma} = \begin{bmatrix} \boldsymbol{\sigma}_1 \\ \boldsymbol{\sigma}_2 \end{bmatrix} = \begin{bmatrix} \boldsymbol{J}_{\sigma_1} \\ \boldsymbol{J}_{\sigma_2} \end{bmatrix} \boldsymbol{x} = \boldsymbol{J}_\sigma \boldsymbol{x} \quad (8)$$

with $\boldsymbol{J}_\sigma \in \mathbb{R}^{Np\times Np}$ and $m = Np$.

The objective is to compute the input $\boldsymbol{y}_i$ in (2) in order to have $\boldsymbol{\sigma}$ tracking a nominal task trajectory $\boldsymbol{\sigma}_n(t)$, allowing human operators to enter the cell during execution. In such a scenario, the safety of the humans is the highest priority task and the robot trajectory must be modified accordingly. To the aim, the nominal trajectory $\boldsymbol{\sigma}_n(t)$ is first properly modified in order to generate a human-safe trajectory $\boldsymbol{\sigma}_r(t)$ which is the trajectory actually tracked as it will be detailed in the following.

Moreover, herein it is not of interest to design algorithms for human detection, while the focus is on defining a human-safe strategy for the coordination of cooperating robots. Hence, the following assumption is made.

Assumption 2. If human operators are in the nearby of the work-cell, either robots are able to detect them or this information is made available to robots. This information might concern, for instance, the position of the head or the chest of the human, or a set of representative points.

As stated above, the control input for the ith robot has to be such that, globally, the cooperative task described according to the task function in (8) tracks the reference $\boldsymbol{\sigma}_r(t)$. Hence, the ith virtual input in (2) can be selected resorting to a standard closed loop inverse kinematic law:

$$\boldsymbol{y}_i = \ddot{\boldsymbol{q}}_i = \boldsymbol{J}_i^{\dagger}\Big(\boldsymbol{\Gamma}_i\boldsymbol{J}_\sigma^{\dagger}\Big(\ddot{\boldsymbol{\sigma}}_r + k_\sigma\dot{\tilde{\boldsymbol{\sigma}}} + \lambda_\sigma\tilde{\boldsymbol{\sigma}}\Big) - \dot{\boldsymbol{J}}_i\dot{\boldsymbol{q}}_i\Big) + \ddot{\boldsymbol{q}}_{n,i} \quad (9)$$

being $\tilde{\boldsymbol{\sigma}} = (\boldsymbol{\sigma}_r - \boldsymbol{\sigma}) \in \mathbb{R}^m$ the task tracking error, $\ddot{\boldsymbol{q}}_{n,i} \in \mathbb{R}^{n_i}$ an arbitrary vector of joint accelerations such as $\boldsymbol{J}_i(\boldsymbol{q}_i)\ddot{\boldsymbol{q}}_{n,i} = \mathbf{0}_p$ which might be exploited to locally optimize secondary objectives, k_σ, λ_σ positive gains and

$$\boldsymbol{\Gamma}_i = \{\boldsymbol{O}_p \cdots \underbrace{\boldsymbol{I}_p}_{i \text{ th robot}} \cdots \boldsymbol{O}_p\} \in \mathbb{R}^{p\times Np} \tag{10}$$

a selection matrix. It is easy to recognize that in virtue of (4) and (2) it holds

$$\boldsymbol{J}_\sigma(\boldsymbol{J}\boldsymbol{y} + \dot{\boldsymbol{J}}\dot{\boldsymbol{q}}) = \boldsymbol{J}_\sigma\ddot{\boldsymbol{x}} = \ddot{\boldsymbol{\sigma}} = \ddot{\boldsymbol{\sigma}}_r + k_\sigma\dot{\tilde{\boldsymbol{\sigma}}} + \lambda_\sigma\tilde{\boldsymbol{\sigma}}$$

where $\boldsymbol{y} = \left[\boldsymbol{y}_1^{\mathrm{T}}, \ldots, \boldsymbol{y}_N^{\mathrm{T}}\right]^{\mathrm{T}}$ and which leads to the following exponentially stable linear second order dynamics

$$\ddot{\tilde{\boldsymbol{\sigma}}} + k_\sigma\dot{\tilde{\boldsymbol{\sigma}}} + \lambda_\sigma\tilde{\boldsymbol{\sigma}} = \mathbf{0}_m$$

3. HUMAN SAFETY ASSESSMENT

In this section, we focus on formulating an index to assess the level of human safety with respect to the team of robots. The devised safety strategy tries to have the robots follow the task trajectory $\boldsymbol{\sigma}_n(t)$ as much as possible in compliance with human safety requirements. The basic idea is to parameterize the nominal trajectory for $\boldsymbol{\sigma}$ in (8) through a non-negative non-decreasing scalar function

$$s_n : t \in [t_0\, t_f] \to \mathbb{R}$$

with t_0 and t_f the initial and final time instant, respectively, and to have the robots cooperatively track

$$\boldsymbol{\sigma}_r(t) = \boldsymbol{\sigma}_n(s_r(t)) \tag{11}$$

where $s_r : t \in \mathbb{R} \to \mathbb{R}$ is a properly *scaled* version of $s_n(t)$ which takes into account the human safety; obviously, this strategy allows the robots to preserve the task path.
Let us introduce a general safety index which allows to quantify the level of human safety with respect to a generic moving point P belonging to the robot structure

$$f(\boldsymbol{p}, \dot{\boldsymbol{p}}, \boldsymbol{p}_o, \dot{\boldsymbol{p}}_o) = \alpha_1(d) + \alpha_2(d, \dot{d}) \tag{12}$$

where $\boldsymbol{p} \in \mathbb{R}^3$ and $\dot{\boldsymbol{p}} \in \mathbb{R}^3$ are the position and velocity of point P, respectively, $d = \|\boldsymbol{p} - \boldsymbol{p}_o\|$ is the distance between the point and the human operator's position $\boldsymbol{p}_o \in \mathbb{R}^3$ assumed to be available (see Assumption 2), $\dot{d}$ is the distance derivative and α_1, α_2 are generic scalar functions such as the following properties hold:

Property 1. $\alpha_1(d)$ is a non negative continuous monotonically increasing function with respect to d;

Property 2. $\alpha_2(d, \dot{d})$ is a continuous monotonically increasing function with respect to $\dot{d}$ and such that:
- (a) $\lim_{\dot{d}\to+\infty} \alpha_2(d, \dot{d}) = c$, $\forall d$ with $c \in \mathbb{R}^+$;
- (b) $\frac{\partial\alpha_2(d,\dot{d})}{\partial\dot{d}} \neq 0$ $\forall d$ and $\forall \dot{d} \neq \infty$.

The ratio behind Property 1 is that the human-safety with respect the point P increases with the distance d. Concerning Property 2, function α_2 is such as the safety index increases for positive values of $\dot{d}$ with a slope that might be modulated by d. The motivation behind the asymptotic bound c in Property 2(a) for $\dot{d} \to +\infty$ is that it prevents the safety index to reach a too high value for high values of $\dot{d}$ and arbitrarily small values of the distance d; in this way, the distance parameter is always the high priority feature. Finally, Property 2(b) ensures that for finite values of $\dot{d}$ the index f is sensitive to variation of velocity $\dot{d}$ such as by changing $\dot{d}$ the value of f can be modified.

By leveraging the approach in Lacevic et al. (2013), the evaluation of the safety function in (12) can be easily extended to the entire structure of the i th manipulator by properly integrating (12) along its structure and obtain a cumulative safety index F^i. In particular, the measure of human safety with respect to the l th link of the i th manipulator can be obtained by integrating f along the volume $\mathcal{V}_l$ of link l

$$F_l^i = \int_{\mathcal{V}_l} f(\boldsymbol{p}, \dot{\boldsymbol{p}}, \boldsymbol{p}_o, \dot{\boldsymbol{p}}_o)\, d\boldsymbol{p} \tag{13}$$

In order to make the computation of (13) affordable, the generic link of the i th robot is simplified as a segment starting at $\boldsymbol{p}_{l,0}^i$ and ending at $\boldsymbol{p}_{l,1}^i$, thus (13) becomes

$$\begin{cases} F_l^i = \displaystyle\int_0^1 f(\boldsymbol{p}_{l,r}^i, \dot{\boldsymbol{p}}_{l,r}^i, \boldsymbol{p}_o, \dot{\boldsymbol{p}}_o)dr \\ \boldsymbol{p}_{l,r}^i = \boldsymbol{p}_{l,0}^i + r(\boldsymbol{p}_{l,1}^i - \boldsymbol{p}_{l,0}^i) \\ \dot{\boldsymbol{p}}_{l,r}^i = \dot{\boldsymbol{p}}_{l,0}^i + r(\dot{\boldsymbol{p}}_{l,1}^i - \dot{\boldsymbol{p}}_{l,0}^i) \end{cases} \tag{14}$$

Finally, the safety index associated to the i th manipulator with n_l^i links is

$$F^i = \sum_{l=1}^{n_l^i+1} F_l^i \tag{15}$$

where an additional virtual link is introduced to account for the end-effector and the cooperative task to achieve.

Concerning the derivative of the safety measure in (15), the following lemma holds.

Lemma 1. The derivative of the cumulative safety function (15) associated to the i th robot is linear in the path parameter acceleration $\ddot{s}_r(t)$, i.e. it is

$$\dot{F}^i = \mu_1^i\, \ddot{s}_r + \mu_2^i \tag{16}$$

where the expressions of μ_1^i, $\mu_2^i \in \mathbb{R}$ are provided in the proof.

Proof. Let us consider the time derivative of the safety function in (12) associated with a generic point $\boldsymbol{p}_{l,r}^i$ ($r \in [0\,1]$) belonging to the l th link of the i th robot; it is

$$\dot{f} = \left(\frac{\partial\alpha_1(d_{l,r}^i)}{\partial d_{l,r}^i} + \frac{\partial\alpha_2(d_{l,r}^i, \dot{d}_{l,r}^i)}{\partial d_{l,r}^i}\right)\dot{d}_{l,r}^i + \frac{\partial\alpha_2(d_{l,r}^i, \dot{d}_{l,r}^i)}{\partial\dot{d}_{l,r}^i}\ddot{d}_{l,r}^i \tag{17}$$

with $d_{l,r}^i = \|\boldsymbol{p}_{l,r}^i - \boldsymbol{p}_o\|$, whose second time derivative is

$$\ddot{d}_{l,r}^i = \boldsymbol{\beta}_1^{\mathrm{T}}\ddot{\boldsymbol{p}}_{l,r}^i + \beta_2 \tag{18}$$

where coefficients $\boldsymbol{\beta}_1 \in \mathbb{R}^3$, $\beta_2 \in \mathbb{R}$ are defined as

$$\begin{cases} \boldsymbol{\beta}_1 = \dfrac{\boldsymbol{p}_{l,r}^i - \boldsymbol{p}_o}{d_{l,r}^i} & d_{l,r}^i \neq 0 \\ \beta_2 = -\boldsymbol{\beta}_1^{\mathrm{T}}\ddot{\boldsymbol{p}}_o + \dfrac{\|\dot{\boldsymbol{p}}_{l,r}^i - \dot{\boldsymbol{p}}_o\|^2}{d_{l,r}^i} - \dfrac{\left[\boldsymbol{\beta}_1^{\mathrm{T}}(\dot{\boldsymbol{p}}_{l,r}^i - \dot{\boldsymbol{p}}_o)\right]^2}{d_{l,r}^i} & d_{l,r}^i \neq 0 \end{cases}$$

At this point, let us consider the well-known relation between the linear acceleration of a point belonging to the structure of a manipulator and its joint variables, i.e.

$$\ddot{\boldsymbol{p}}_{l,r}^i = \boldsymbol{J}_{l,r}^i(\boldsymbol{q}_i)\ddot{\boldsymbol{q}}_i + \dot{\boldsymbol{J}}_{l,r}^i(\boldsymbol{q}_i, \dot{\boldsymbol{q}}_i)\dot{\boldsymbol{q}}_i \tag{19}$$

being $\boldsymbol{J}_{l,r}^i \in \mathbb{R}^{3\times n_i}$ the positional Jacobian matrix associated to $\boldsymbol{p}_{l,r}^i$. Now, by partially deriving the reference task function in (11) with respect to s_r, it holds

$$\dot{\boldsymbol{\sigma}}_r = \frac{\partial\boldsymbol{\sigma}_r}{\partial s_r}\dot{s}_r, \quad \ddot{\boldsymbol{\sigma}}_r = \frac{\partial^2\boldsymbol{\sigma}_r}{\partial s_r^2}\dot{s}_r^2 + \frac{\partial\boldsymbol{\sigma}_r}{\partial s_r}\ddot{s}_r$$

and in virtue of (9), equation (19) can be expressed as

$$\ddot{\boldsymbol{p}}^i_{l,r} = \boldsymbol{\gamma}_1 \ddot{s}_r + \boldsymbol{\gamma}_2 \tag{20}$$

where $\boldsymbol{\gamma}_1$,$\boldsymbol{\gamma}_2 \in \mathbb{R}^3$ are defined as

$$\begin{cases} \boldsymbol{\gamma}_1 = \boldsymbol{J}^i_{l,r} \boldsymbol{J}^\dagger_i \boldsymbol{\Gamma}_i \boldsymbol{J}^\dagger_\sigma \dfrac{\partial \boldsymbol{\sigma}_r}{\partial s_r} \\ \boldsymbol{\gamma}_2 = \boldsymbol{J}^i_{l,r} [\boldsymbol{J}^\dagger_i \boldsymbol{\Gamma}_i \boldsymbol{J}^\dagger_\sigma \left(\dfrac{\partial^2 \boldsymbol{\sigma}_r}{\partial s_r^2} \dot{s}_r^2 + k_\sigma \dot{\tilde{\boldsymbol{\sigma}}} + \lambda_\sigma \tilde{\boldsymbol{\sigma}} \right) - \boldsymbol{J}^\dagger_i \dot{\boldsymbol{J}}_i \dot{\boldsymbol{q}}_i + \ddot{\boldsymbol{q}}_{n,i}] \\ \quad + \dot{\boldsymbol{J}}^i_{l,r} \dot{\boldsymbol{q}}_i \end{cases}$$

By folding (18) and (20) in (17), the term $\dot{f}$ becomes

$$\dot{f} = \lambda_1 \ddot{s}_r + \lambda_2 \tag{21}$$

where the expressions of λ_1 and $\lambda_2 \in \mathbb{R}$ are

$$\begin{cases} \lambda_1 = (\boldsymbol{\beta}_1^{\mathrm{T}} \boldsymbol{\gamma}_1) \dfrac{\partial \alpha_2}{\partial \dot{d}^i_{l,r}} \\ \lambda_2 = (\boldsymbol{\beta}_1^{\mathrm{T}} \boldsymbol{\gamma}_2 + \beta_2) \dfrac{\partial \alpha_2}{\partial \dot{d}^i_{l,r}} + \left(\dfrac{\partial \alpha_1}{\partial d^i_{l,r}} + \dfrac{\partial \alpha_2}{\partial d^i_{l,r}} \right) \dot{d}^i_{l,r} \end{cases}$$

Therefore, in virtue of (14),(15) and (21), it finally holds

$$\dot{F}^i = \mu^i_1 \ddot{s}_r + \mu^i_2$$

with μ^i_1, $\mu^i_2 \in \mathbb{R}$ defined as below

$$\begin{cases} \mu^i_1 = \displaystyle\sum_{j=1}^{n^i_l+1} \int_0^1 \lambda_1(\boldsymbol{p}^i_{l,r}, \dot{\boldsymbol{p}}^i_{l,r}, \boldsymbol{p}_o, \dot{\boldsymbol{p}}_o, \boldsymbol{q}_i, \dot{\boldsymbol{q}}_i, s_r)\, dr \\ \mu^i_2 = \displaystyle\sum_{j=1}^{n^i_l+1} \int_0^1 \lambda_2(\boldsymbol{p}^i_{l,r}, \dot{\boldsymbol{p}}^i_{l,r}, \boldsymbol{p}_o, \dot{\boldsymbol{p}}_o, \ddot{\boldsymbol{p}}_o, \boldsymbol{q}_i, \dot{\boldsymbol{q}}_i, \ddot{\boldsymbol{q}}_{n,i}, s_r, \dot{s}_r)\, dr \end{cases}$$

where the dependencies of λ_1 and λ_2 on their parameters are now made explicit for the sake of completeness. This completes the proof. ■

In the multi-robot case, the overall safety function F (and its derivative), which accounts for all the worker robots in the team, can be easily deduced by combining the safety functions in (15) associated to each manipulator

$$F = \sum_{i=1}^{N} F^i, \quad \dot{F} = \sum_{i=1}^{N} \dot{F}^i \tag{22}$$

We are now ready to formally state the following problem.

Problem 1. Let us consider a multi-robot system composed by N mobile manipulators performing the cooperative task defined as in (8) for which a desired trajectory $\boldsymbol{\sigma}_n(s_n(t))$ parametrized with respect to a scalar function $s_n(t)$ is assigned. Moreover, let us also assume that a minimum value F_{min} for function F in (22) is assigned; then, our objective is to properly scale $\boldsymbol{\sigma}_n(t) = \boldsymbol{\sigma}_n(s_n(t))$ so as to generate a new reference trajectory $\boldsymbol{\sigma}_r(t) = \boldsymbol{\sigma}_n(s_r(t))$ such as $F \geq F_{min}$, $\forall t$.

Remark 1. Problem 1 requires that a minimum value F_{min} for function F is defined; thus, the problem arises on how to choose this lower bound. A first strategy consists in tuning F_{min} via experimental trials based on the human feeling about the *experienced* level of safety resorting to techniques similar to Acharya et al. (2006). Another strategy consists in selecting F_{min} such as, defined d as the distance between the human operator and the team

$$d = \min_{\forall i, l, r} \|\boldsymbol{p}^i_{l,r} - \boldsymbol{p}_o\| \tag{23}$$

$F \geq F_{min}$ ensures that $d \geq d_{min}$ for some value $d_{min} > 0$ (Lacevic et al. (2013)). As an example, the second strategy is pursued in the Section 5.

The next section provides a possible solution to Problem 1.

4. THE HUMAN-ROBOT AVOIDANCE STRATEGY

An overview of the devised strategy for solving Problem 1 is provided in Figure 1; in particular, the proposed approach foresees tracking the nominal trajectory until the level of human safety is above the minimum accepted value, i.e. $F > F_{min}$; if the nominal trajectory leads the safety level to its minimum value, then a velocity modulation is applied while preserving the nominal path and, if this is not enough to guarantee $F \geq F_{min}$, then the requirement of preserving the path is relaxed. It is worth remarking that, in the case of redundant robots, each manipulator also exploits the extra degrees of freedom to maximize the cumulative safety index.

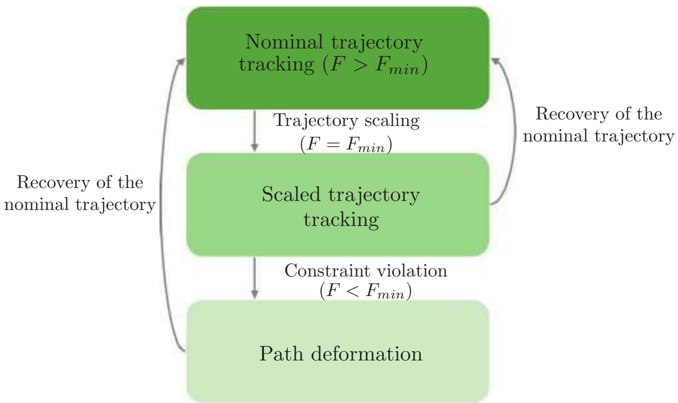

Fig. 1. High-level scheme of the human avoidance strategy; transition conditions are detailed in Section 4.

4.1 Human-robot avoidance via trajectory scaling

By leveraging the approach in Dahl and Nielsen (1990) designed for torque-limited path following of industrial robots, a scaling parameter $s_r(t)$ is introduced that is function of $s_n(t)$ according to the following relation

$$\begin{cases} s_r(t) = s_n(t) + \Delta s(t) \\ \dot{s}_r(t) = \dot{s}_n(t) + \dot{\Delta s}(t) \\ \ddot{s}_r(t) = \ddot{s}_n(t) + \ddot{\Delta s}(t) \end{cases} \tag{24}$$

where $\Delta s(t)$ ($\dot{\Delta s}$, $\ddot{\Delta s}$) might be either negative or positive and is adopted to properly scale the nominal path parameter while it is such as $\Delta s(t) = \dot{\Delta s}(t) = \ddot{\Delta s}(t) = 0$ (i.e., $s_n(t) = s_r(t)$) in nominal conditions (no safety issue arises). Moreover, it is required that at any instant

$$\dot{\Delta s}(t) \geq -\dot{s}_n(t) \tag{25}$$

$$s_n(t) + \Delta s(t) \leq s_n(t_f) \tag{26}$$

The constraints (25) and (26) ensure that no reverse motion occurs along the path and that the end-point of the nominal trajectory is not overcome, respectively.

By folding (16) in (22), the expression of $\dot{F}$ can be stated as follows

$$\dot{F} = \mu_1 \ddot{\Delta s} + \mu_2 \tag{27}$$

with μ_1, $\mu_2 \in \mathbb{R}$ defined as

$$\begin{cases} \mu_1 = \displaystyle\sum_{i=1}^{N} \mu^i_1 \\ \mu_2 = \ddot{s}_n \displaystyle\sum_{i=1}^{N} \mu^i_1 + \sum_{i=1}^{N} \mu^i_2 \end{cases}$$

and which is linear in $\Delta\ddot{s}$. At this point, we are ready to determine the scaling terms Δs, $\Delta\dot{s}$ and $\Delta\ddot{s}$ such that the minimum safety condition is met. Therefore, starting from the constraint $F \geq F_{min}$, the lower ($\Delta\ddot{s}_{min}$) and the upper ($\Delta\ddot{s}_{max}$) bounds on the parameter $\Delta\ddot{s}$ are computed as

$$\Delta\ddot{s}_{max} = \begin{cases} -\mu_2/\mu_1, & \mu_1 < 0 \wedge F = F_{min} \\ +\infty, & \text{otherwise} \end{cases} \tag{28}$$

and

$$\Delta\ddot{s}_{min} = \begin{cases} -\mu_2/\mu_1, & \mu_1 > 0 \wedge F = F_{min} \\ -\infty, & \text{otherwise} \end{cases} \tag{29}$$

The ratio behind (28) and (29) is that, as long as $F > F_{min}$, no constraint on $\dot{F}$ (and then on $\Delta\ddot{s}_{min}$ and $\Delta\ddot{s}_{max}$) is set; while, in the case $F = F_{min}$, the computed bounds are such as $\Delta\ddot{s}_{min} \leq \Delta\ddot{s} \leq \Delta\ddot{s}_{max}$ ensures that $\dot{F} \geq 0$ and, then, that F does no fall below F_{min}.
The derived bounds in (28) and (29) are used within the following dynamic system to compute $\Delta\ddot{s}$:

$$\begin{cases} \Delta\ddot{s} = -k_d \Delta\dot{s} - k_p \Delta s \\ \Delta\ddot{s} = \mathrm{sat}(\Delta\ddot{s}, \Delta\ddot{s}_{min}, \Delta\ddot{s}_{max}) \end{cases} \tag{30}$$

where $\Delta s(t_0) = \Delta\dot{s}(t_0) = 0$, k_d and k_p are positive constants and sat() is any saturation function that bounds $\Delta\ddot{s}$ in the range $[\Delta\ddot{s}_{min}, \Delta\ddot{s}_{max}]$. The first equation in (30) is such as to continuously bring Δs to zero (i.e., s_r to s_n), while, in the second equation, this value is saturated according to the computed bounds. Thus, when the saturation function does not alter the input value, the scaling term Δs ($\Delta\dot{s}$, $\Delta\ddot{s}$) asymptotically converges to zero.

Remark 2. Constraints in (25) and (26) imply that the scaling strategy does not generally guarantee the condition $F \geq F_{min}$ to be fulfilled. For example, in the case $\Delta\dot{s} = -\dot{s}_n$ and $\Delta\ddot{s}_{max} < 0$, it is evident that further scaling would violate the constraint in (25).

Because of Remark 2, a different avoidance strategy is presented in the following section which is adopted when the condition $F \geq F_{min}$ cannot be secured by the scaling strategy presented above and that, in brief, allows the path constraint to be violated (see Figure 1).

4.2 Human-robot avoidance via nominal path deformation

In the case the dynamics in (30) leads to one of the constraints (25) and (26) being violated, the cooperative task is aborted and other avoidance strategies need to be adopted. To this aim, two cases should be considered: loosely connected robots and tightly connected robots (as in a multi-robot transportation task of rigid objects). In the first case, once the task has been aborted, the human safety can be guaranteed independently by each robot adopting, for example, the approach devised in Lacevic et al. (2013). Therefore, this case is not investigated in this paper. In the more interesting case of tightly connected robots, the avoidance strategy needs to be compliant with the kinematic constraint that consists in having $\boldsymbol{\sigma}_2$ constant in any reference frame attached to the grasped object. For this reason, the avoidance strategy must consist in properly modifying $\boldsymbol{\sigma}_1$ and, as in the previous case, exploiting the local redundancy. In detail, let t_s be the time instant in which the path constraint is relaxed, then the reference trajectory is modified as

$$\begin{cases} \boldsymbol{\sigma}_r(t) = \boldsymbol{\sigma}_r(t_s^-) + \Delta\boldsymbol{\sigma}_r(t) \\ \dot{\boldsymbol{\sigma}}_r(t) = \Delta\dot{\boldsymbol{\sigma}}_r(t) \\ \ddot{\boldsymbol{\sigma}}_r(t) = \Delta\ddot{\boldsymbol{\sigma}}_r(t) \end{cases} \tag{31}$$

where the displacement $\Delta\boldsymbol{\sigma}_r(t)$ is computed according to the following dynamics

$$\begin{cases} \boldsymbol{M}\Delta\ddot{\boldsymbol{\sigma}}_r(t) + \boldsymbol{D}\Delta\dot{\boldsymbol{\sigma}}_r(t) + \boldsymbol{K}\Delta\boldsymbol{\sigma}_r(t) = \boldsymbol{f}_r(t) \\ \Delta\boldsymbol{\sigma}_r(t_s) = \mathbf{0}_m \\ \Delta\dot{\boldsymbol{\sigma}}_r(t_s) = \dot{\boldsymbol{\sigma}}_r(t_s^-) \end{cases} \tag{32}$$

with $\boldsymbol{M}$, $\boldsymbol{D}$, $\boldsymbol{K} \in \mathbb{R}^{m\times m}$ positive definite matrices and $\boldsymbol{f}_r \in \mathbb{R}^m$ a virtual force to be properly defined; the initial conditions in (32) are such that to guarantee the continuity of the reference trajectory in the switching time t_s. Regarding the virtual force in (32), it is selected as

$$\boldsymbol{f}_r = \begin{bmatrix} -k_r\, f_r(F)\dfrac{\nabla F^{\mathrm{T}}}{\|\nabla F\|} & \mathbf{0}_{m-3}^{\mathrm{T}} \end{bmatrix}^{\mathrm{T}} \tag{33}$$

where k_r is a positive gain, $\nabla F \in \mathbb{R}^3$ is the gradient of the cumulative safety function with respect to $\boldsymbol{p}_o$ and $f_r(F)$ is a monotonically non increasing function of the safety index F which converges to the origin for F sufficiently high, i.e. $F > F_{min} + \Delta F$ with $\Delta F \in \mathbb{R}^+$. Thus, the repulsive force is such to modify the reference centroid position with an intensity that increases when the safety value decreases and is zero when safety is restored; concerning the direction, it is opposite to that of the gradient ∇F since it represents the direction in which the operator should move to maximise F. A possible choice of $f_r(F)$ is shown in Figure 2.

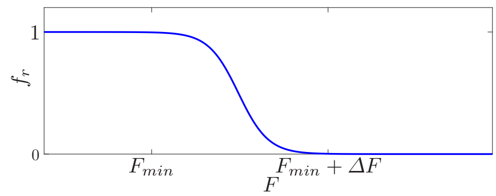

Fig. 2. Value of the intensity $f_r(F)$ in (33).

Finally, when the following conditions are met:

(1) $\boldsymbol{f}_r = \mathbf{0}_m$, i.e. repulsive forces are no longer required
(2) $\Delta\boldsymbol{\sigma}_r(t) = \Delta\dot{\boldsymbol{\sigma}}_r(t) = \mathbf{0}_m$, i.e. the transient vanished

the cooperative task can be restored (see Figure 1) starting from the condition $\boldsymbol{\sigma}_r = \boldsymbol{\sigma}_r(t_s)$.

5. SIMULATION CASE STUDY

In this simulation case study, a setup composed of $N = 3$ mobile arms is considered and is depicted in Figure 3. In detail, each worker robot is a Comau Smart Six (6-DOFs) mounted on holonomic mobile base in order to move in the xy plane (2-DOFs); the team's goal is to cooperatively transport loads from the picking conveyor belts on the left of the cell to the deposit one on the right. Such a task can be easily formulated by means of absolute and relative task variables introduced in (8) where the former are appropriate for expressing the position and orientation of the grasped object, while the latter for expressing robots formation. Simulation results are provided in the video available at the following link [3].
Moreover, in order to asses the level of human safety, the coefficients of f in (12) are chosen in compliance with Properties 1 and 2 as

$$\begin{cases} \alpha_1(d) = k_1 d \\ \alpha_2(\dot{d}) = k_2 \tanh(\dot{d}) \end{cases} \tag{34}$$

[3] www.automatica.unisa.it/video/CoopHumanSafetySYROCO.mp4

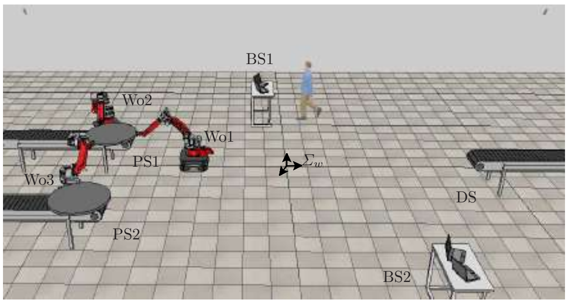

Fig. 3. Cell configuration composed by 3 workers (Woi, $i = 1, 2, 3$), load picking and depositing stations (PSi, $i = 1, 2$ and DS, respectively) and base stations for operators (BSi, $i = 1, 2$); Σ_w is the world reference frame.

with $k_1, k_2 \in \mathbb{R}^+$, leading to

$$f(\boldsymbol{p}, \dot{\boldsymbol{p}}, \boldsymbol{p}_o, \dot{\boldsymbol{p}}_o) = k_1 d + k_2 \tanh(\dot{d}) \tag{35}$$

where $\boldsymbol{p}_o$ is selected as the chest position of the human operator. The ratio behind the expression of function f is that it is a combination of a linear term with respect to the distance d and a monotonically increasing term with respect to the derivative $\dot{d}$ whose contribution to the safety f is negative when distance is decreasing ($\dot{d} < 0$) and positive for increasing values ($\dot{d} > 0$). Starting from the expression of f in (35), F^i ($i = 1, 2, 3$) and F in (22) are computed according to the procedure in Section 3. The computation of the value F_{min} such that to ensure $d \geq d_{min}$ in Remark 1 is shown in the Appendix for the selected safety function in (35). Moreover, due to the redundancy of the robots at hand, i.e. $n_i = 8$ and $p = 6$, the vector of joint accelerations $\ddot{\boldsymbol{q}}_{n,i}$ in (9) can be locally exploited to maximize the ith safety index F^i. To this aim, the acceleration vector is designed as in Hsu et al. (1988), which is standard for second order kinematics, while the desired velocity to be projected in the null space of $\boldsymbol{J}_i$ is computed with a gradient technique accordingly to the procedure in Lacevic et al. (2013).
The following gains are selected for the virtual input in (9), $k_\sigma = 20$, $\lambda_\sigma = 100$, while the following ones for the avoidance strategy, $k_d = 4.5$, $k_p = 5$, $\boldsymbol{M} = \boldsymbol{I}_{18}$, $\boldsymbol{D} = 6.5\boldsymbol{I}_{18}$, $\boldsymbol{K} = 10\boldsymbol{I}_{18}$ $k_r = 15$, $\Delta F = 15$ in equations (30), (32) and (33), respectively; finally, the minimum cumulative safety value is set as $F_{min} = 80$.
Figure 4 shows key snapshots of the simulation while detailed results are presented in Figures 5-7. In the simulation study, human behaviour mainly interferes in two phases with the robots task leading once to modify the nominal trajectory via velocity scaling and once via path deformation. In detail, the scaling phase (from $t = 8.7$ s up to $t = 20$ s) occurs when the robots move towards the operator standing at the first base station (Figure 4.b), while the impedance phase (from $t = 39.2$ s up to $t = 45.1$ s) occurs when the operator crosses the robots nominal path and the scaling trajectory is no longer sufficient for ensuring minimum safety (Figure 4.c).

Figure 5 shows the progress of the safety index during the human-robot interaction; in particular, it makes evident that, during the scaling phase (S), the safety value is almost saturated at its minimum value while an increase of it is detected at the beginning of the impedance phase (I) due to the path constraint relaxation.

Concerning the scaling strategy, Figure 6 shows how the scaling parameters vary over time; in particular, scaling phase is firstly characterized by a decrease of $\dot{\Delta}s$, i.e. a slowdown of nominal trajectory, and then an increase of

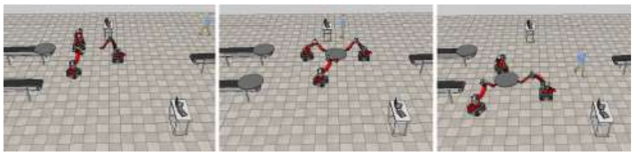

a) b) c)

Fig. 4. Simulation snapshots representing the initial system configuration (a), the scaling phase (b) and the impedance phase (c), respectively.

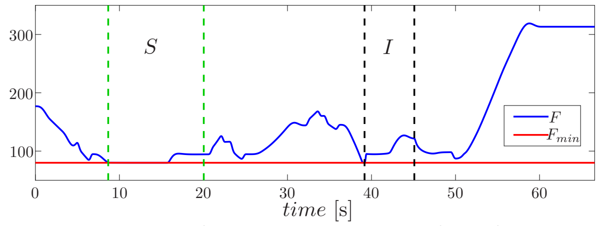

Fig. 5. Evolution of the cumulative safety function (in blue) with respect to its minimum allowed value (in red); scaling and impedance phases are marked with S and I, respectively.

it in order to restore nominal trajectory tracking (i.e. the condition $\ddot{\Delta}s = \dot{\Delta}s = \Delta s = 0$). This effect is also evident from Figure 7 where the centroid position of the nominal trajectory is compared to that of the reference one. Moreover, Figure 7 shows how trajectory is modified when path constraint is relaxed; in this case, starting from $\boldsymbol{\sigma}_r(t_s = 39.2\,\text{s})$ the reference trajectory evolves according to the impedance model in (32) and then, when repulsive action is no longer necessary, it returns again to $\boldsymbol{\sigma}_r(t_s)$ in order to restore the tracking of the nominal trajectory.

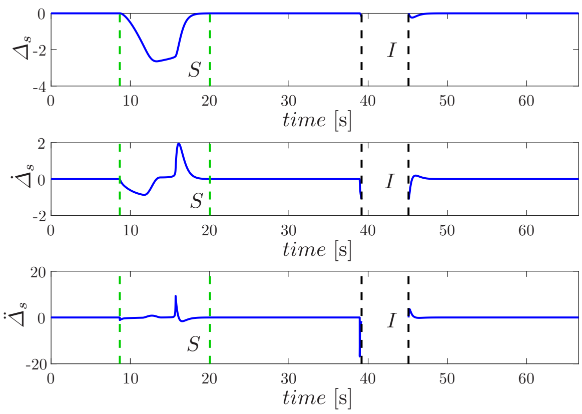

Fig. 6. Evolution of scaling terms; scaling and impedance phases are marked with S and I, respectively. In the impedance phase, no plots are provided since the nominal path is abandoned.

6. CONCLUSIONS

In this work, a general approach to achieve cooperative tasks by multi-robot systems in coexistence with human operators was presented. To this aim, the human-robot safe interaction is first assessed by the definition of a general safety index and, then, a strategy capable of ensuring a safe human-robot interaction is defined. At the same time, this strategy is such as to preserve as much as possible the desired cooperative task and, only in the case the human safety cannot be longer ensured, the task is aborted and a suitable avoidance strategy is undertaken.

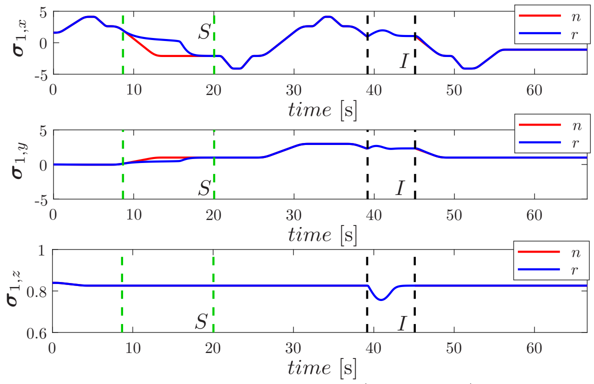

Fig. 7. Evolution of the nominal (n, in red) and reference (r, in blue) trajectories of the team centroid position; scaling and impedance phases are marked with S and I, respectively. In the impedance phase, nominal trajectory is not shown since its tracking is aborted.

As future work, the approach will be extended to cope with a decentralized architecture and will be validated through experiments on a real setup.

APPENDIX

For a given value d_{min} of d in (23), the objective is to compute F_{min} such as $F \geq F_{min}$ implies $d \geq d_{min}$. For this purpose, let us first consider the case of a single n_l link manipulator. The required F_{min} can be computed as the maximum value of F for all $\boldsymbol{p}_o$ such as $d = d_{min}$

$$\begin{aligned} F &= \sum_{l=1}^{n_l} \int_0^1 \left(k_1 d_{l,r} + k_2 \tanh(\dot{d}_{l,r}) \right) \, dr \\ &\leq \sum_{l=1}^{n_l} \left(k_1 \int_0^1 \|\boldsymbol{p}_{l,0} + r(\boldsymbol{p}_{l,1} - \boldsymbol{p}_{l,0}) - \boldsymbol{p}_o\| \, dr + k_2 \right) \\ &\leq k_1 \left(\frac{1}{2} \sum_{l=1}^{n_l} L_l + \sum_{l=1}^{n_l} \|\boldsymbol{p}_{l,0} - \boldsymbol{p}_o\| \right) + k_2 \, n_l \end{aligned} \tag{A.1}$$

where L_l is the length of the l th link. Let $\boldsymbol{p}^\star$ be the generic point on the robot structure at distance d_{min} from $\boldsymbol{p}_o$, i.e., $\|\boldsymbol{p}_o - \boldsymbol{p}^\star\| = d_{min}$, then the following inequalities holds

$$\begin{aligned} \|\boldsymbol{p}_{l,0} - \boldsymbol{p}_o \pm \boldsymbol{p}^\star\| &\leq \|\boldsymbol{p}_{l,0} - \boldsymbol{p}^\star\| + \|\boldsymbol{p}_o - \boldsymbol{p}^\star\| \\ &\leq \sum_{l=1}^{n_l} L_l + d_{min} = L + d_{min} \end{aligned} \tag{A.2}$$

where $L = \sum_{l=1}^{n_l} L_l$ and the obvious relation $\|\boldsymbol{p}_{l,0} - \boldsymbol{p}^\star\| \leq L$ has been exploited. Hence, in virtue of (A.1) and (A.2), it follows that for single robot

$$F_{min} = k_1 \left(\frac{2n_l + 1}{2} L + n_l \, d_{min} \right) + k_2 \, n_l$$

By generalizing to the case of N robots, it holds

$$F \leq \sum_{i=1}^{N} \left[k_1 \left(\frac{1}{2} L^i + \sum_{l=1}^{n_l^i+1} \|\boldsymbol{p}_{l,0}^i - \boldsymbol{p}_o\| \right) + k_2 \, (n_l^i + 1) \right] \tag{A.3}$$

where $L^i = \sum_{l=1}^{n_l^i+1} L_l^i$ also takes into account the virtual link to the team centroid. Moreover, since the robots are assumed to be in formation, the structure composed by the i th manipulator and the one at minimum distance d_{min} can be analysed in turn as an "aggregate" manipulator whose maximum sum of link lengths is $L^i + L_{max}$ with $L_{max} = \max_{i \in 1,..,N} L^i$; therefore, it holds

$$\|\boldsymbol{p}_{l,0}^i - \boldsymbol{p}_o\| \leq L^i + L_{max} + d_{min} \tag{A.4}$$

From (A.3) and (A.4), it follows that

$$\begin{aligned} F_{min} = \sum_{i=1}^{N} [k_1 & \left(\frac{2n_l^i + 3}{2} L^i + (n_l^i + 1)(L_{max} + d_{min}) \right) \\ & + k_2 \, (n_l^i + 1)] \end{aligned}$$

is such to ensure that each point on each manipulator is at least at distance d_{min} from the operator.

REFERENCES

Acharya, U.R., Joseph, K.P., Kannathal, N., Lim, C.M., and Suri, J.S. (2006). Heart rate variability: a review. *Medical and Biological Engineering and Computing*, 44(12), 1031–1051.

Basile, F., Caccavale, F., Chiacchio, P., Coppola, J., and Curatella, C. (2012). Task-oriented motion planning for multi-arm robotic systems. *Robotics and Computer-Integrated Manufacturing*, 28(5), 569–582.

Cirillo, A., Ficuciello, F., Natale, C., Pirozzi, S., and Villani, L. (2016). A conformable force/tactile skin for physical human-robot interaction. *IEEE Robotics and Automation Letters*, 1(1), 41–48.

Dahl, O. and Nielsen, L. (1990). Torque-limited path following by on-line trajectory time scaling. *IEEE Transaction on Robotics and Automation*, 6, 554–561.

Flacco, F., Krger, T., Luca, A.D., and Khatib, O. (2012). A depth space approach to human-robot collision avoidance. In *2012 IEEE International Conference on Robotics and Automation*, 338–345.

Haddadin, S., Albu-Schffer, A., and Hirzinger, G. (2009). Requirements for safe robots: Measurements, analysis and new insights. *The International Journal of Robotics Research*, 28(11-12), 1507–1527.

Hsu, P., Hauser, J., and Sastry, S. (1988). Dynamic control of redundant manipulators. In *1988 American Control Conference*, 2135–2139.

Khatib, O. (1985). Real-time obstacle avoidance for manipulators and mobile robots. In *Proceedings. 1985 IEEE International Conference on Robotics and Automation*, volume 2, 500–505.

Kimmel, M. and Hirche, S. (2017). Invariance control for safe human-robot interaction in dynamic environments. *IEEE Transactions on Robotics*, 33(6), 1327–1342.

Kulić, D. and Croft, E.A. (2006). Real-time safety for humanrobot interaction. *Robotics and Autonomous Systems*, 54(1), 1 – 12.

Lacevic, B., Rocco, P., and Zanchettin, A.M. (2013). Safety assessment and control of robotic manipulators using danger field. *IEEE Transactions on Robotics*, 29(5), 1257–1270.

Liu, C. and Tomizuka, M. (2016). Algorithmic safety measures for intelligent industrial co-robots. In *2016 IEEE International Conference on Robotics and Automation (ICRA)*, 3095–3102.

Robla-Gómez, S., Becerra, V.M., Llata, J.R., Gonzlez-Sarabia, E., Torre-Ferrero, C., and Prez-Oria, J. (2017). Working together: A review on safe human-robot collaboration in industrial environments. *IEEE Access*, 5, 26754–26773.

Zanchettin, A.M., Ceriani, N.M., Rocco, P., Ding, H., and Matthias, B. (2016). Safety in human-robot collaborative manufacturing environments: Metrics and control. *IEEE Transactions on Automation Science and Engineering*, 13(2), 882–893.

Smart Inspection Tools in robotized aircraft panels manufacturing

Andrea Bruni
Research for Innovation
Loccioni
Angeli di Rosora (AN), Italy
a.bruni@loccioni.com

Enrico Concettoni
Research for Innovation
Loccioni
Angeli di Rosora (AN), Italy
e.concettoni@loccioni.com

Cristina Cristalli
Research for Innovation
Loccioni
Angeli di Rosora (AN), Italy
c.cristalli@loccioni.com

Matteo Nisi
Research for Innovation
Loccioni
Angeli di Rosora (AN), Italy
m.nisi@loccioni.com

***Abstract*—This paper presents the Smart Inspection Tools developed for the robotic cell designed for fuselage panels manufacturing, in the LABOR project. This project has the objective to develop a small size, low-cost automatic cell for the drilling, fastening, sealing and inspection of fuselage panels for regional aircraft. This paper focuses on the development of the two Smart Inspection Tools used for referencing the robot with respect to the panel geometry and to check the quality of the manufactured holes. Different inspection technologies have been exploited to guarantee the strict project specifications. The paper presents the design of the developed tool and shows the experimental results of a prototypal versions.**

Keywords—Inspection tool, Vision system, Robotized Aircraft manufacturing, Countersink hole inspection, Fastener inspection

I. Introduction

One of the most important challenges for the next aircraft assembly lines is the increase in the level of automation. There are several reasons to pursue such an objective as the high-quality standards allowed by automatized solutions or the high production rates and flexibility. These features are more and more important since aerospace production volumes have been increasing steadily over the last three years. For instance, Boeing Commercial Airplanes built more than 700 airliners in 2014 while about 650 in 2013 and 600 in 2012. Furthermore, the annual report by Airbus (year 2016) reveals a long backlog of 6.847 aircraft, with only 688 commercial aircraft delivered, representing about 10 years of production at current rates. Airbus projects a need for about 35,000 new passenger aircraft – valued at US$5.3 trillion – over the next 20 years, based on its latest Global Market Forecast (GMF): “Growing Horizons” [1]. Overall, the total worldwide fleet of passenger and freighter aircraft will double by 2036 – with an estimated requirement for 24.810 new single-aisle aircraft, 8.690 new twin-aisle wide-bodies and 1.410 new very large aircraft [1]. For this reason, main aeronautic manufacturers are heavily investing in flexible systems to reduce costs, improve quality and boost productivity, mainly by adopting robots, Automated Guided Vehicles (AGV) and other technologies. Drilling, fastener insertion, riveting, sealing, coating and painting applications, in addition to material handling, are the most recurrent operations in aircraft assembly lines. The majority of these operations are performed by machines and big robots, i.e., high-cost rigid solutions [2-5], but still a high number of the drilling and riveting operations are performed by the operators. Therefore, it is clear that the automation of such operations would lead to great and immediate benefits to aircraft industry in terms of production rate. However, mainly because of safety motivations and government regulations, hard constraints are requested to be met, especially concerning the process tolerances.

The LABOR project [6] will approach the problem with a new concept based on Self-Adaptive Robotic Cell that combines:

- small/medium size robots to provide higher capability of adaptation and easy integration in shop floor already existing facilities as shown in [7-9],
- adaptive processing tools in order to perform in an automatic and adaptive way the different processing tasks,
- advanced vision systems in order to reference the robots and check the quality of the work performed, and distributed intelligence in order to build a more flexible solution.

In the aircraft manufacturing process, the state of the art for the inspection of holes and fasteners relies on manual mechanical instruments. Each measurement has its own gauge: height/depth gauge, chamfer gauge, grip length gauge, gap gauge, shape gage and many others that guarantee the required measurement accuracy. A first approach toward measurement automation can be the use of such probes on a robotic arm. However, the use of contact measurement system on the robot, as presented in [10], is not effective due to the difficult integration of manual probes on an automatic system and due to the reduced robot accuracy. A better approach is represented by non-contact measurement systems which allow a better integration on robot wrist, especially as regard vision measurement techniques. The measurement is usually performed in different positions to cover undercut, thus requiring the use of a robot to perform the task. High accuracy instrumentation is bulky and not really suitable to be integrated in a fast tool changer as in [11-12]. Better results can be obtained with non-contact inspection probes as represented in [13-15]. These solutions guarantee high accuracy but they are very expensive and not so rugged to be safely installed on an automatic process in an industrial environment. The most suitable solutions are thus represented by vision non-contact inspection techniques based on the use of 2D cameras and lighting systems as in [16-17]. However, solutions found in the state of art have still some limits because does not guarantee the required accuracy or they are focused on a specific and particular measurement losing in generality. The same limits have been found among commercial solutions. For example, [18] has tried to overcome these limitations by developing a series of instruments dedicated to online surface measurements for the aeronautic sector, but their line-up is limited to dent and rivet flushness measurement. For a complete measurement set, [19] has presented an instrument for diameter, countersink diameter, countersink depth, grip length and perpendicular measurement but this tool is designed to be hand held and cannot perform referencing tasks.

In conclusion, the constraints in the present applications impose a design for a tool specifically developed for the integration in an automatic process and suitable to be mounted on a robotic arm.

In this contest, the LABOR Smart Inspection Tools have been developed, with the aim of reducing costs, weights, and dimensions according to the small-scale robot integration but respecting at the same time the strict requirements of the aeronautical sector. In the following paragraphs firstly the specifications for the Smart Inspection Tools will be summarized. Then, the proposed inspection techniques will be presented and the developed tools will be described. Finally, experimental results conducted with Smart Inspection Tools prototypes will be presented and discussed.

II. PROJECT REQUIREMENTS

The panels that must be manufactured in the LABOR robotic cell are composed of a CFRP skin with frames and shear ties temporarily glued on the skin. The LABOR robotic cell must drill and fastener holes on the outer panel surface to obtain a definitive coupling. The Smart Inspection Tools developed in the LABOR project have three main objectives:

- O1: scan from the internal side of the panel the geometry of the substructure (frames and shear ties) in order to reposition and align the robot before drilling;
- O2: check the quality of the drilled holes in terms of absence of delamination (or burrs in case of metals) occurring at the joint interfaces or at the exit of the hole, the hole diameter, and countersink;
- O3: check the quality of the installed fasteners in terms of flushness and sleeve diameter and height.

In Fig. 1 the countersink hole parameters are highlighted and the fastener main components are depicted. In Fig. 2, Fig. 3 and Fig. 4 the fastener installations parameters are described. According to the project specifications, maximum acceptable limits for the parameters described above are summarized in TABLE I.

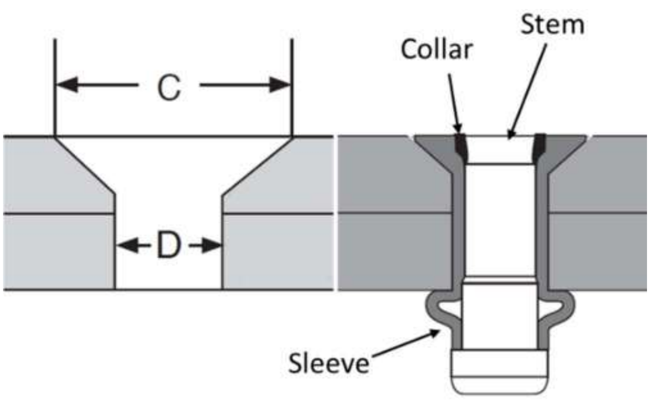

Fig. 1. Holes parameters and fasteners components

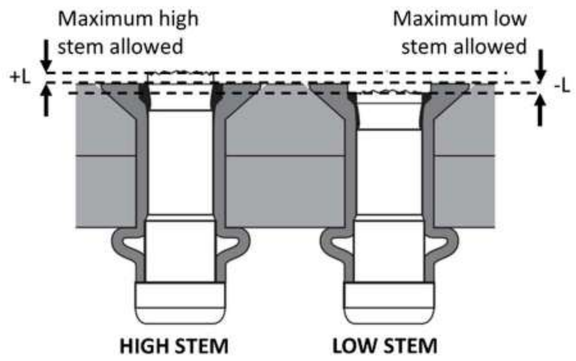

Fig. 2. Fastener Stem installation limits

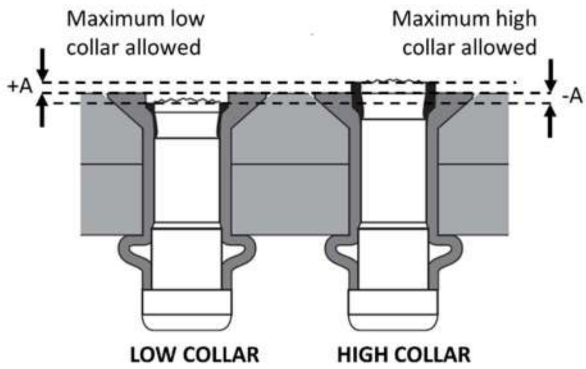

Fig. 3. Fastener Collar installation limits

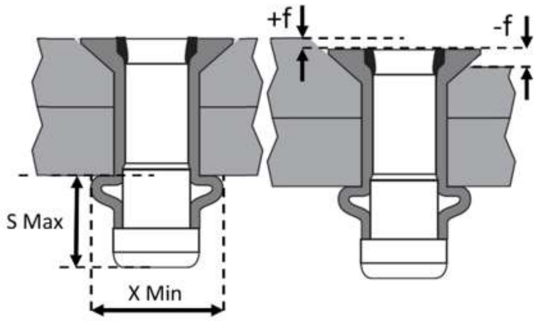

Fig. 4. Fastener Sleeve and Flushness installation limits

TABLE I. Hole dimensions and fastener installation parameter according to LABOR project specifications

Parameter	Value
Hole position tolerance	±0.2 mm
Hole diameter tollerance (D)	[0 - 0.076] mm
Countersink diameter tolerance (C)	±0.0635 mm
Flushness tolerance (f)	±0.203 mm
Maximum Sleeve height (S Max)	5.9 mm
Minimum Sleeve diameter (X Min)	5.7 mm
Stem protrusion limits (C)	±0.254
Collar protrusion limits (A)	±0.4318

III. METHODOLOGY

The different required measurements are performed with two Smart Inspection Tools mainly for geometrical and weight constraints. The small/medium size robot has a limited payload, thus two smaller and lighter tools have been preferred with respect to a single bigger tool. Each tool exploits a different inspection technique and guarantees the required measurement performances as specified in [20].

The first tool (represented in Fig. 5) uses a 2D camera for measuring the hole diameter and the countersink diameter (O2).

The tool is composed of the following parts:

- One Camera
- Telecentric Lens
- Diffusive ring light (blue 450nm)
- A band-pass filter centered on 450nm

Several lighting solutions with different wavelength have been tested mainly because the reflection of the CFRP countersink hole creates problems for a correct measurement of both diameters (hole and countersink). Spotlights due to a direct reflection of light source on the camera sensor cause the saturation of the image and reduce the quality of the diameter measurement. Thus, a different technique has been proposed based on a diffusive blue (450nm) ring light that significantly reduces the reflection thanks to a diffuser and a different incident light angle. The internal and external diameters are then measured through an edge detection analysis (Fig. 6). The measurement algorithm automatically finds the hole within the image, compares the measured diameters with the nominal tolerance defined in TABLE I and assess if the drilled hole can be accepted, otherwise requires the operator attendance. Finally, the 2D Smart Inspection Tool is mounted on an electric linear axis that allows adjusting the camera focus. Indeed, the robot position error can, affects the distance between the camera and the panel, thus causing errors in the diameter measurements. To correct this issue, autofocus techniques can be tested in order to adjust the camera distance by moving the linear axis and then improving the measuring accuracy.

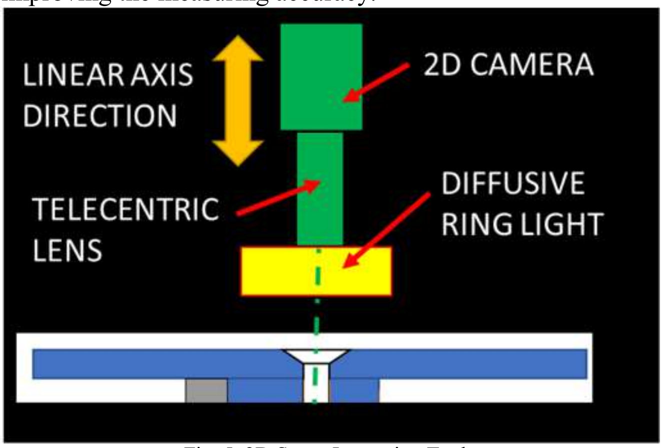

Fig. 5. 2D Smart Inspection Tool

The second Smart Inspection Tool is represented in Fig. 7; it measures the correct installation of the fastener and scans the internal panel surface for robot reference (O1 and O3). It consists of a profilometer composed of a structured LED light pattern projector and two cameras to avoid undercuts [21].

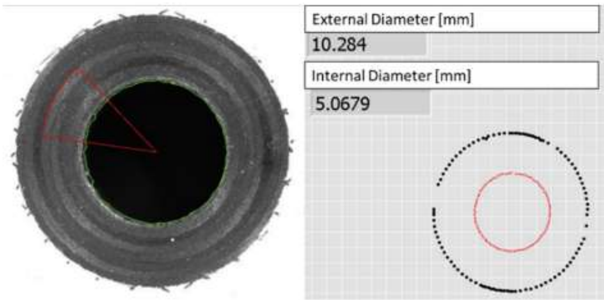

Fig. 6. Image acquired (left); Image elaboration (right)

The tool is composed of the following parts:

- Two cameras
- 35mm Lens
- A structured LED light pattern projector.

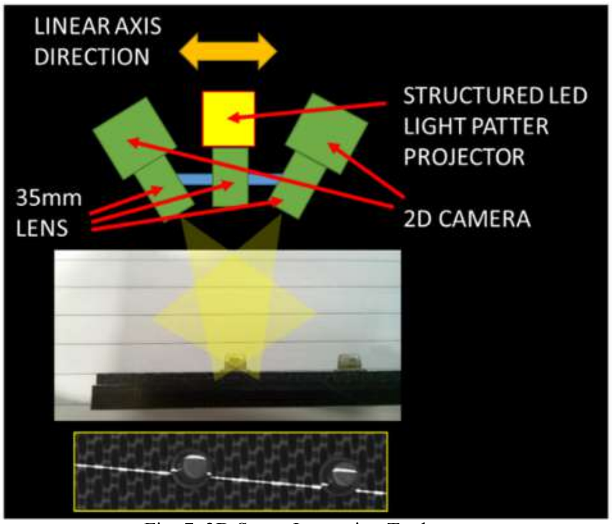

Fig. 7. 3D Smart Inspection Tool

The structured LED light projects on the target a 10μm width line. The use of a blue LED source instead of a laser reduces speckle and increases accuracy. The two cameras extract the profiles (left and right) to ensure a complete view of the target even in case of one camera has undercut or occlusions. The 3D Smart Inspection Tool is mounted on an electric linear axis that allows translating the tool on a direction perpendicular to the projected line. At regular intervals, the tool extracts two profiles like the one represented in Fig. 8. All the profiles are then combined together allowing a 3D reconstruction (point cloud) of the scanned object (Fig. 9). Finally, the left and right point clouds (extract from the left and right cameras) are merged to obtain a complete reconstruction of the target object. The obtained point cloud contains a great number of information that can be elaborated to extract the required measurement by interpolating geometrical entities.

The proposed approach allows to increase the tool flexibility, the design is not specific for a particular measurement and several quantities can be extracted by analyzing the point cloud. In detail, for the purposes of the LABOR project, the 3D Smart Inspection Tool can be used to measure all the required quantities on the fastener head and sleeve and to reconstruct the geometry of the internal panel surface.

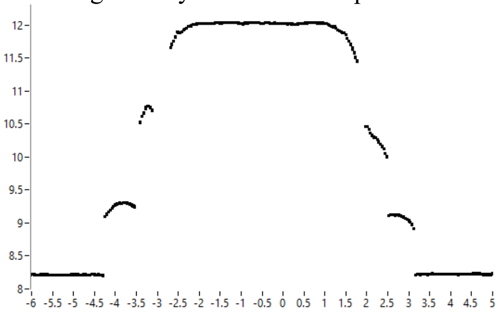

Fig. 8. Extracted profile

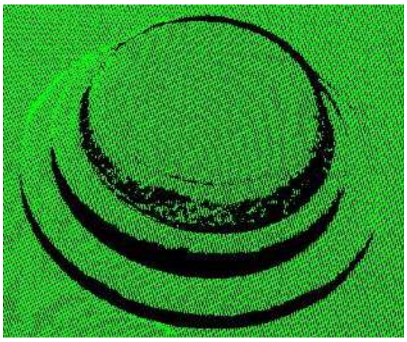

Fig. 9. Reconstructed 3D point cloud

The proposed Smart Inspection Tools, both for 2D and 3D inspection, satisfy the project requirements: small dimensions, lightweight, accurate measurements, and flexibility. In the following paragraph, a preliminary test on tool prototypes will be presented,

IV. RESULTS

In this paragraph, preliminary results of the measurements conducted with the Smart Inspection Tools prototypes are presented. In Fig. 10 a correct and incorrect installed fastener are represented for both the fastener head and sleeve. In Fig. 11 examples of extracted profiles are presented, while in Fig. 12 the point clouds of a corrected and uncorrected installer fastener head are compared.

Fig. 10. Correct installed and defected fastener head and sleeve

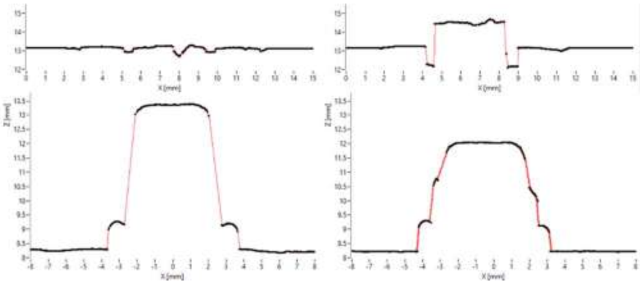

Fig. 11. Correct installed and defected fastener head and sleeve (profile)

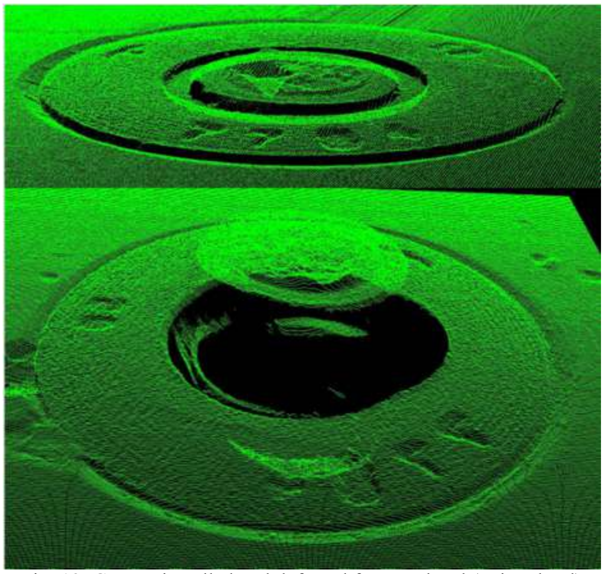

Fig. 12. Correct installed and defected fastener head (point cloud)

The profiles can thus be elaborated to extract the geometrical features that must be measured in the LABOR project as represented in Fig. 13.

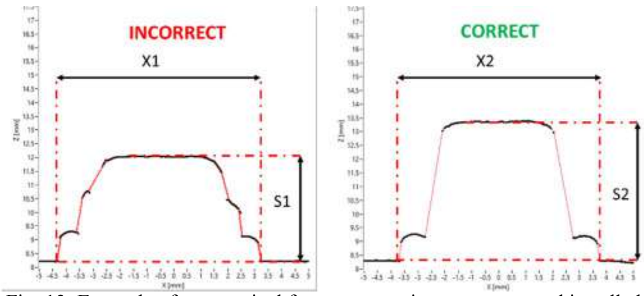

Fig. 13. Example of geometrical feature extraction on a corrected installed and defected fastener sleeve

Finally, a validation of the 2D Smart Inspection Tool measurement is given. A sample with four countersink hole has been prepared. Some defects and irregularities on the hole edge were present in order to test the Inspection Tool measurement algorithm robustness. The sample is presented in Fig. 14.

Fig. 14. Countersink hole sample

Each hole has been measured with the 2D Smart Inspection Tool (50 times) and with a CMM (coordinate measuring machine) “ZEISS O-INSPECT” as reference. In Fig. 15 and Fig. 16 results are shown for the internal and external diameters of each hole.

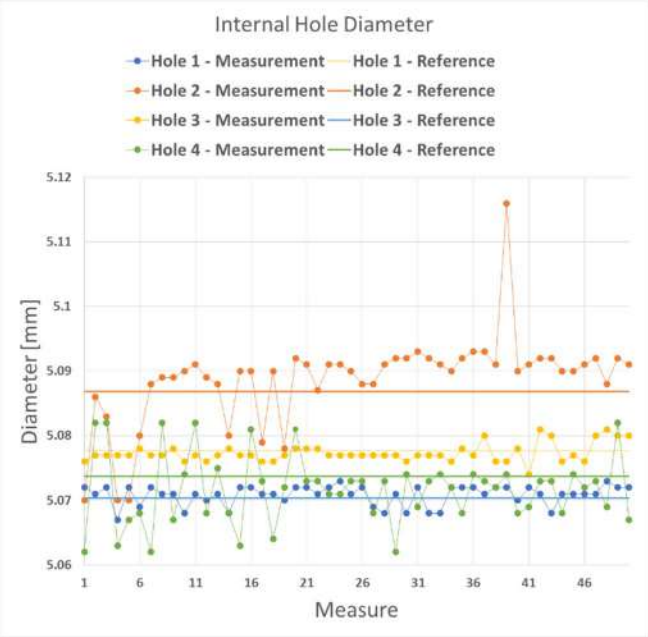

Fig. 15. Internal hole diameter measured with 2D Smart Inspection Tool

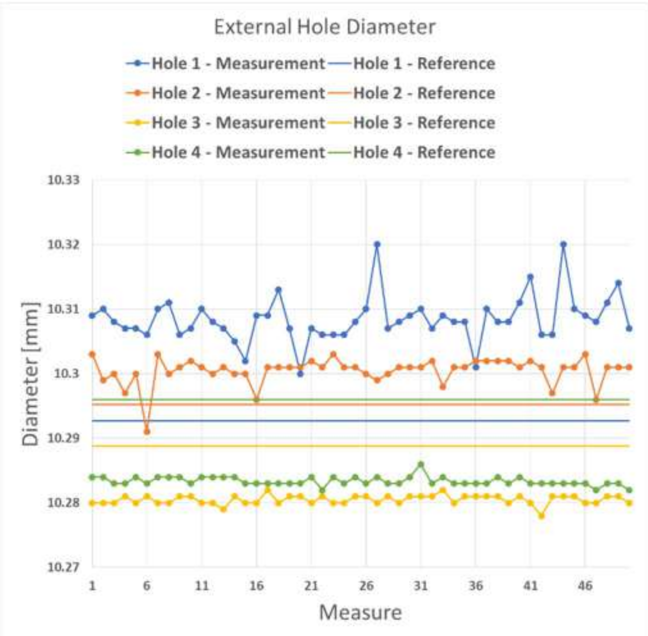

Fig. 16. External countersink hole diameter measured with 2D Smart Inspection Tool

Data has been analyzed and results are shown in TABLE II. For each hole, for both internal and external diameters, the measurement repeatability has been calculated and also the maximum deviation between the mean value and the true value from the CMM machine is given. Finally, the maximum repeatability values for all four holes are shown.

TABLE II. 2D Smart Inspection Tool Repeatability

TRUE VALUE from ZEISS O-INSPECT [mm]							
Hole 1		**Hole 2**		**Hole 3**		**Hole 4**	
INT	EXT	INT	EXT	INT	EXT	INT	EXT
5.1139	10.258	5.1105	10.251	5.127	10.257	5.1178	10.255
TRUE VALUE - MEAN VALUE [mm]							
Hole 1		**Hole 2**		**Hole 3**		**Hole 4**	
INT	EXT	INT	EXT	INT	EXT	INT	EXT
-0.042	0.0252	-0.033	0.0295	0.038	0.0431	-0.047	0.0536
REPEATABILITY (MAX VALUE - MIN VALUE) [mm]							
Hole 1		**Hole 2**		**Hole 3**		**Hole 4**	
INT	EXT	INT	EXT	INT	EXT	INT	EXT
0.02	0.004	0.007	0.004	0.046	0.012	0.006	0.02
MAX. REPEATABILITY INTERNAL DIAM. [mm]							0.046
MAX. REPEATABILITY EXTERNAL DIAM. [mm]							0.02

The results show, globally, good values for repeatability, better for the external diameter rather than the internal one. Data also show an offset between true values and measured values. The main reason for this offset can be a not precise alignment between the optical axis and the perpendicular of the target surface. This issues will be solved in the final system setup because the 2D Inspection Tool will be installed on the robot wrist that will be equipped with a normality sensor that will check and correct the correct orientation of the Inspection Tool prior to performing the measurement.

In Fig. 17 and Fig. 18 the measurements obtained with the 3D smart Inspection Tool are reported. A sample of four installed fasteners (Fig. 19) has been measured 50 times and, for each measurement, the mean value and the standard deviation have been evaluated. The graphs reports, for each quantity, the maximum admissible value (in red) according to LABOR requirements (refer to TABLE I), the mean value and the standard deviation (in black). The five quantities evaluated are flushness (a), collar protrusion (b), stem protrusion (c), sleeve height (d) and sleeve diameter (e).

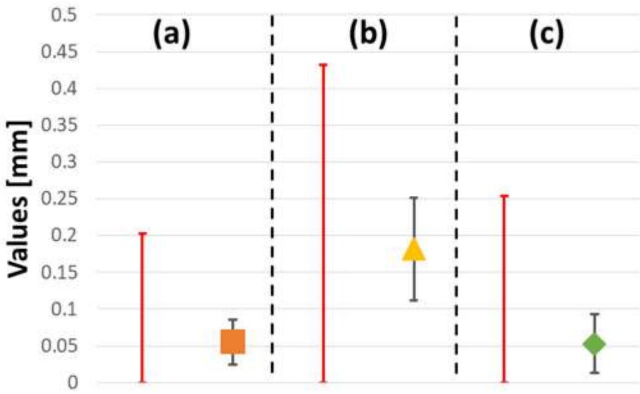

Fig. 17. 3D Smart Inspection Tool measurement results (1/2)

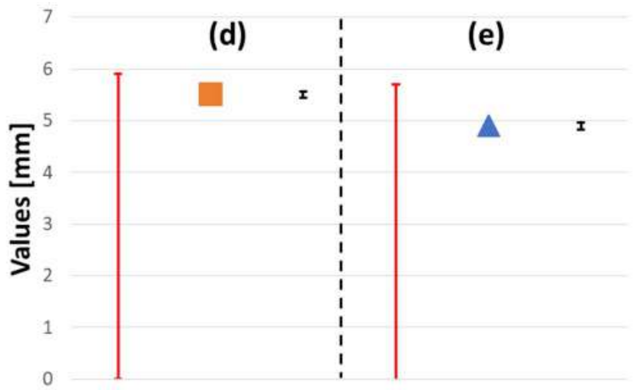

Fig. 18. 3D Smart Inspection Tool measurement results (2/2)

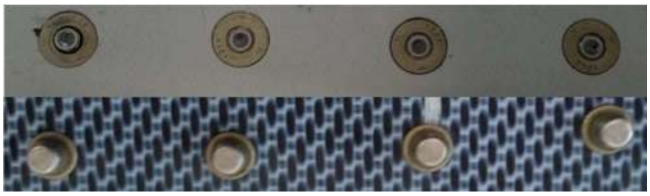
Fig. 19. Sample of installed fasteners

Also for the 3D Smart Inspection Tool, the results are positive and show that the proposed solution satisfies the project requirements. The obtained error is compatible with the required measurement accuracy. A detailed characterization of the proposed equipment will be presented in future works.

V. CONCLUSIONS

The Smart Inspection Tools presented in this paper satisfy the inspection requirements of the LABOR project and more in general the requirements usually applied in the aeronautical sector. Moreover, small dimensions and lightweight design have been guaranteed in order to mount the tools on small/medium scale robots. This is an important objective in order to pursue the automatization trend of the growing aircraft industry. In the followings, both tools will be installed on the LABOR robotic cell and thus performance on the real system will be tested and validated.

ACKNOWLEDGMENT

The research leading to these results has received funding from the European Commission H2020 Program – Clean Sky 2 JU, under GA n. 785419 LABOR - Lean robotized AssemBly and cOntrol of composite aeRostructures.

REFERENCES

[1] Airbus, "Global Market Forecast (GMF) 2017-2036," Growing horizons, Apr. 2017.

[2] S. Holt and R. Clauss, “Robotic drilling and countersinking on highly curved surfaces,” SAE Technical Paper, 2015-01-2517, Sept. 2015.

[3] http://www.loxin2002.com/software, [Accessed May 20, 2019].

[4] https://www.kuka.com/en-us/products/production-systems/aerospace-systems-engineering/material-handling-solutions/mobile-robotic-platform, [Accessed May 20, 2019].

[5] T. Dillhoefer, “Power RACe,” SAE Technical Paper, 2017-01-2093, Sept. 2017.

[6] www.labor-project.eu, European Community-Clean Sky 2 JU, [Accessed May 20, 2019].

[7] D. Massa, M. Callegari, and C. Cristalli, “Manual guidance for industrial robot programming,” Industrial Robot: An International Journal, vol. 42(5), pp. 457-465, 2015.

[8] D. W. I. J. Meißner, M. S. F. Schmatz, D. I. F. Beuß, D. W. I. J. Sender, I. W. Flügge, and D. K. F. E. Gorr, "Smart human-robot-collaboration in mechanical joining processes," Procedia Manufacturing, vol. 24, pp. 264-270, 2018.

[9] N. Jayaweera and P. Webb, "Automated assembly of fuselage skin panels," Assembly Automation, vol. 27(4), pp. 343-355, 2007.

[10] M. B. Bauza, S. C. Woody, S. T. Smith, and R. J. Hocken, "Development of a rapid profilometer with an application to roundness gauging," Precision engineering, vol. 30(4), pp. 406-413, 2006.

[11] Y. Chugui, L. Finogenov, V. Kiryanov, V. Nikitin, A. Sametov, and P. Zavyalov, "Inspection of holes parameters using a ring diffractive focuser," VDI BERICHTE, vol. 1844, pp. 433-444, 2004.

[12] L. Pilny, L. De Chiffre, M. Piska, and M.F. Villumsen, "Hole quality and burr reduction in drilling aluminium sheets," CIRP Journal of Manufacturing Science and Technology, vol. 5(2), pp. 102-107, 2012.

[13] Z. Usman, R.P. Monfared, N. Lohse, and M.R. Jackson, "An investigation of highly accurate and precise robotic hole measurements using non-contact devices," International Journal of Metrology and Quality Engineering, vol. 7(2), pp. 204, 2016.

[14] N. Wu, W. Zhao, X. Wang, Y. Tao, and Z. Hou, "A novel design of through-hole depth on-machine optical measuring equipment for automatic drilling and riveting," Applied Sciences, vol. 8(12), pp. 2671, 2018.

[15] E. Hong, H. Zhang, R. Katz, and J. S. Agapiou, "Non-contact inspection of internal threads of machined parts", The International Journal of Advanced Manufacturing Technology, vol. 62, pp. 221-229, Sept. 2011.

[16] M. Baeg, S. Baeg, C. Moon, G. Jeong, H. Ahn, and D. Kim, "A new robotic 3D inspection system of automotive screw hole," International Journal of Control, Automation, and Systems, vol. 6 (5), pp. 740-745, Oct. 2008.

[17] G. S. Spagnolo, L. Cozzella, and F. Leccese, "Viability of an optoelectronic system for real time roughness measurement," Measurement, vol. 58, pp. 537-543, 2014.

[18] http://8-tree.com [Accessed May 20, 2019]

[19] http://www.unitedsciences.com/aeroscan [Accessed May 20, 2019]

[20] ISO 10360-7:2011 “Geometrical production specifications (GPS) - Acceptance and reverification tests for coordinate measuring machines (CMM) - Part 7: CMMs equipped with imaging probing systems”, International Standard Organization, 2011.

[21] G. Frankowsky, “Fast and contactless optical measurement of the 3D shape and surface roughness by projected micro fringes,” Proceedings of the XIth Int. Coll. on Surf., Germany (2004).

A fuzzy inference approach to control robot speed in human-robot shared workspaces

Angelo Campomaggiore, Marco Costanzo, Gaetano Lettera and Ciro Natale
Dipartimento di Ingegneria, Università degli Studi della Campania "Luigi Vanvitelli", Via Roma 29, Aversa, Italy
angelo.campomaggiore@studenti.unicampania.it, {marco.costanzo, gaetano.lettera, ciro.natale}@unicampania.it

Keywords: Human-robot collaboration, Workspace monitoring, Fuzzy logic

Abstract: Nowadays, human-robot collaboration (HRC) is an important topic in the industrial sector. According to the current regulations, the robot no longer needs to be isolated in a work cell, but a collaborative workspace in which human operators and robots coexist can be acceptable. Human-robot interaction (HRI) is made possible by proper design of the robot and by using advanced sensors with high accuracy, which are adopted to monitor collaborative operations to ensure the human safety. Goal of this article is to implement a fuzzy inference system, based on the ISO/TS 15066, to correctly compute the minimum protective separation distance and adjust the robot speed by considering different possible situations, with the aim to avoid any collisions between operators and robots trying to minimize cycle time as well.

[1]

1 INTRODUCTION

The research paper tackles the human-robot collaboration problem by following the line of the current regulations and introducing a new approach to be used in manufacturing industry. The novel method assures human operators safety, without modifying the robot predefined path and defining a safety metric to scale robot trajectory only when indispensable, thus trying to maximize the production time.

The research work is carried out in the framework of a European project (The LABOR project, 2019), which has the objective to propose novel robotized assembly paradigms of aircraft fuselage panels. Until recently, the aerospace industry was still conservative and companies tended to use successful assembly methods that had already been proven to work in the past. Nowadays, many assembly sub-operations try to exploit robotics, e.g., drilling, fastening and sealing tasks. These operations are no longer manually performed by human operators but by industrial robots equipped with dedicated tools or by large automated machines dedicated to assembly of specific parts. However, there are some detailed operations which require human capabilities and that must be still executed by operators. This is the case of hybrid metal and composite structures, where, after the drilling operation, some parts have to be manually removed for further manual operations, like deburring, and then re-installed on the skin panel before the sealing and riveting operations, as shown in Figure 1.

This requires to setup a robotic cell that has to foresee the presence of a human operator, hence the necessity to monitor the shared workspace. Real-time workspace monitoring for human-robot coexistence is not an easy problem to solve. Even more, implementing strategies to maximize the production time and preserve human safety at the same time is a research challenge. The approach proposed here is to adopt a fuzzy inference logic that can update the planned robot velocity in real-time according to robust perception data and a set of rules formulated based on a risk analysis. This can lead to a novel, acceptable solution.

Ensuring the safety of a human operator is the main purpose of the current research of industrial collaborative robotics. The safety standards for applications of industrial robots are laid out by the International Organization for Standardization (ISO) (ISO 10218-1, 2011), (ISO 10218-2, 2011), and by the upcoming ISO proposed draft Technical Specification (TS) (ISO/TS 15066, 2016), which addresses four collaborative scenarios:

1. *Safety-rated Monitored Stop* (SMS), which re-

[1] ©2019 Scitepress. Presented @ICINCO 2019. DOI: http://dx.doi.org/10.5220/0007838700780087

quires that the robot stops when a human is in the collaborative workspace;

2. *Hand Guiding* (HG), which allows the operator to hand-guide the robot through an hand guiding equipment (e.g., an analog button cell attached to the robot) and an emergency stop conforming to International Electrical Commission (IEC) (IEC 60204-1, 2009);
3. *Speed and Separation Monitoring* (SSM), which monitors the robot speed according to the separation distance from the operator;
4. *Power and Force Limiting* (PFL), which limits the momentum of the robot such that the potential for operator injury upon impact is minimized, according to the established injury standards (Bicchi et al., 2008).

In this paper, a strategy to handle the operators safety in industrial SSM scenarios is investigated. The main goal is to reasonably scale down the size of the protective zone around the robot and improve productivity, taking into account safety regulations. The robot behavior is modified, in terms of trajectory scaling, only if there is a real and imminent risk of collision. The operator approach into the collaborative workspace is deeply analyzed to generalize the computing method of the safety index and face the extreme variability and unpredictability of human behaviours. The devised solution computes the points at minimum distance between the robot and the closest human and presents several desirable features with respect to other solutions, e.g., (Zhang et al., 2016),(Bascetta et al., 2011),(Lippi and Marino, 2018),(Bjerkeng et al., 2014); many of these approaches rely on evasive actions to increase safety. However, in industrial setting, it is generally recommended to follow the robot predefined path without deviating from it, especially in complex work cells, where clashes are likely to occur. The main characteristics of the proposed approach are:

- it considers the whole surface of human operators, without using skeleton-based techniques and without approximating the body to a single point;
- it considers the whole robot kinematic chain, the entire volume and possible tools, without factoring only a singular representative element of the robot (e.g., the end effector);
- it explicitly takes into account the regulations;
- it predicts the human velocity v_H, by estimating it from perception data without assuming it constant;
- it is based on a risk analysis that considers the relative directions of velocities, which are not taken into account in the equation proposed by the current regulations;
- it does not modify the robot programmed path and it does not require the task to be aborted.

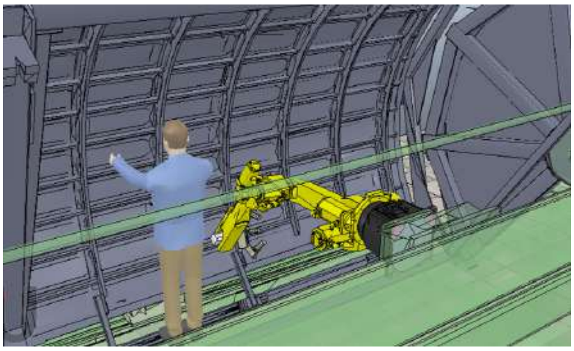

Figure 1: Example of a manual assembly operation where the operator shares the workspace with a robot.

2 ISO ANALYSIS: SSM

SSM allows the robot system and the operator to move concurrently in the collaborative workspace. Risk reduction is achieved by maintaining at least the minimum protective separation distance, S, between the human operator and the robot all the time. During robot motion, the robot system never gets closer to the operator than S. When the Euclidean separation distance, d, is equal to or less than S, the robot system stops, before it can impact the operator. When the operator moves away from the robot system, the robot system can resume the motion automatically while maintaining at least the protective separation distance.

(ISO 13855, 2010) is the first document which investigates the issue of safeguards positioning for human safety in stationary, active machinery. The document suggests to compute S as

$$S = vT + C, \tag{1}$$

where v is the approach speed of human body parts and its value is assumed to be as the maximum operator speed of 2.0 m/s, unless d is greater than 0.5 m, in which case may be set at 1.6 m/s. T is the total system stopping performance time, in seconds, and it is a combination of the time required by the machine to respond to the operator's presence (i.e., T_R) and the response time of the machine which brings the robot to a safe, controlled stop (i.e., T_S). C is the intrusion distance safety margin, which represents an additional distance, based on the expected intrusion toward the critical zone prior to the actuation of the protective equipment.

From eq. (1), ISO/TS 15066 updates the S meaning by including robot dynamic properties. When the robot system reduces its speed, the protective separation distance decreases correspondingly, i.e.,

$$S(t_0) \geq \int_{\tau=t_0}^{\tau=t_0+T_R+T_S} v_H(\tau)d\tau + \int_{\tau=t_0}^{\tau=t_0+T_R} v_R(\tau)d\tau + \int_{\tau=t_0+T_R}^{\tau=t_0+T_R+T_S} v_S(\tau)d\tau + (C+Z_S+Z_R) \tag{2}$$

In (2), v_H is the "directed speed" of the closest operator which travels toward the robot, v_R is the speed of the robot in the direction of the operator, v_S is the directed speed of the robot in course of stopping. The remaining terms represents uncertainties: the intrusion distance C is based on the operator reach, Z_R is the robot position uncertainty, and Z_S is the operator position uncertainty (i.e., the sensor uncertainty). Finally, t_0 is considered the current time.

The main issue of (ISO 13855, 2010) is that the separation distance was initially intended for static machinery, not for dynamic and reconfigurable robotic systems. Therefore, extending what is contained in the standard to the case of industrial robotics is not trivial. Nevertheless, ISO/TS 15066 tries to make a contribution to the HRC problem and describes S using the linear function

$$S = (v_H T_R + v_H T_S) + (v_R T_R) + (B) + (C + Z_S + Z_R) \tag{3}$$

where B is the Euclidean distance travelled by the robot while braking. Note the one-to-one correlation between eq. (2) and the linear relationship (3). The first term in parentheses describes the contribution attributable to the operator's change in location in the time necessary to bring the robot to a full stop from its current speed. The second term describes the contribution attributable to the robot system reaction time, before it initiates the braking sequence. The third term describes the distance travelled by the robot during its braking. Finally, the fourth term describes the possible distance of intrusion into the robot work volume as a function of the operator reach and the uncertainty of the sensory system and robot kinematics. The values of v_H, T_S, B and C can be found in the safety standards: the values of v_H and C are given in ISO 13855, while guidelines for evaluating T_S and B are given in Annex B of ISO 10218-1 and they result from measurements that directly depend on the robot system under test.

This paper decomposes and assesses the performance of ISO/TS 15066 SSM minimum protective distance metric and adds a contribution to improve some aspects to allow its applicability in industrial scenarios. The following sections widely discuss four main areas that are directly pertinent to SSM: human detection and tracking, prediction of human and robot motions, safety separation maintenance and robot speed monitoring.

3 HUMAN-ROBOT INTERACTION

The robot control system must be able to adapt the robot trajectory to the current observed scene and to perform its task efficiently and safely. This means that the control system must be able to detect the presence of human operators inside the collaborative workspace, to track the human closest to the machine and, finally, to modulate the robot speed according to the minimum protective distance S.

The HRC has been addressed dividing it into two distinct problems: human detection and tracking (HDT) and intention estimation (IE).

3.1 Perception System

The experimental set-up of this work is composed by two depth cameras, which have been used to monitor the collaborative workspace: a *Microsoft Kinect v1* and an *Intel RealSense D435* (see Figure 2a). At least two views become necessary to minimize the occlusions of the observed area, as shown in Figure 2b and Figure 2c.

An intrinsic calibration is necessary to update the rough intrinsic default parameters, as well as, a sphere-tracking procedure has been developed for extrinsic calibration. The obtained homogeneous transformation matrices, $T_{camera1}^{robot}$ and $T_{camera2}^{robot}$, express the poses of the camera frames with respect to the robot base frame.

The goal of the extrinsic calibration is to obtain an accurate identification of the camera pose, which guarantees the minimum relative positioning error when the two camera views are merged.

Therefore, a 3D tracking technique has been developed by using a polystyrene sphere of 0.12 m diameter. The red sphere has been mounted at the robot end effector, so as to match the center of the sphere with the origin of the end-effector frame, as shown in Figure 2. The calibration procedure uses the *M-estimator SAmple Consensus* (MSAC) algorithm (Torr and Murray, 1997) (which is an extension of the best known *RANdom SAmple Consensus* (RANSAC) algorithm (Fischler and Bolles, 1981)), to find a sphere within a radius constraint, and to provide its geometric model. The robot has been positioned at specific configurations, which allow to correctly

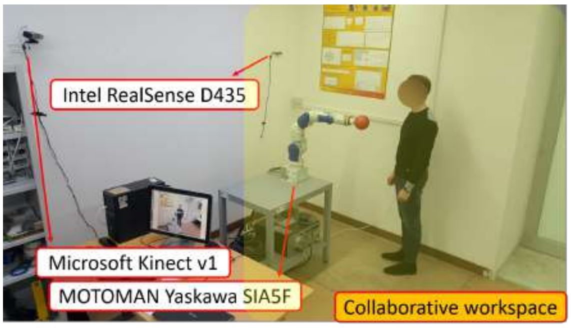

(a) Perception system.

(b) Kinect RGB view. (c) RealSense RGB view.

Figure 2: Experimental set-up.

distinguish the target within the two camera views. From the robot joint states, the forward kinematics computes the pose of the center of the red sphere. At the same time, the developed procedure acquires the depth images, converts them into point clouds (Rusu and Cousins, 2011) and estimates the target model. The method is iterated to cover the entire collaborative workspace and to minimize the positioning error. Finally, the transformation matrices have been evaluated through an optimization algorithm with a cost function that combines the data of both cameras.

3.2 Human Detection and Tracking

Realizing a safe HRC application requires a very fast HDT algorithm, which detects human operators in real time. In this study, a novel point cloud-based methodology is presented to compute the minimum distance between the whole body of the detected operators and a robot. Since this operation is computationally heavy, a *Background Segmentation* (BS) algorithm is developed to subtract the static environment from the observed scene and to process exclusively the information related to the dynamic objects. The developed pipeline is shown in Figure 3.

The perception system described in Section 3.1 observes the surroundings of the manipulator and the robot kinematic chain is fully visible. While the workspace is monitored, the robot executes its task, thus it becomes a dynamic entity. Therefore, the *Realtime URDF Filter* (Blodow, 2012) is used to remove the robot from the scene.

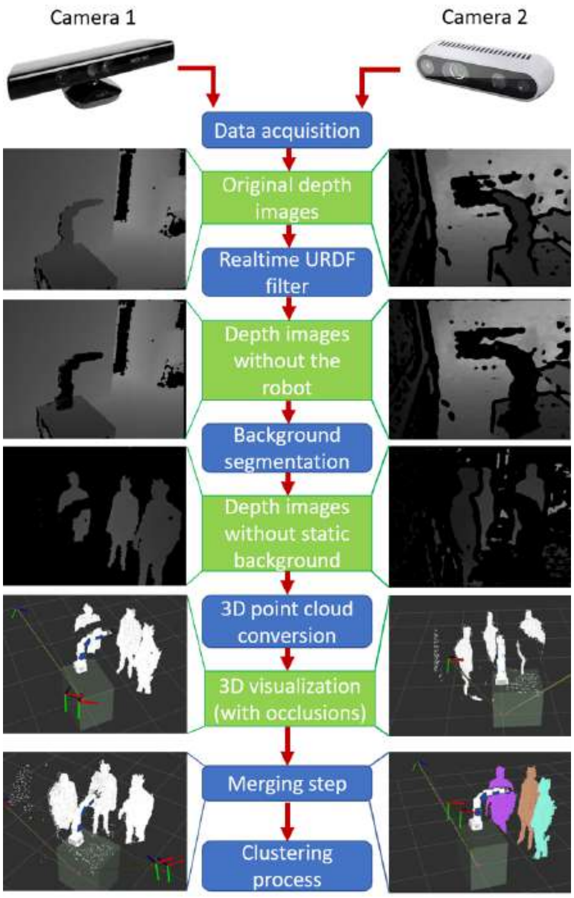

Figure 3: Implemented HDT pipeline.

The implementation of the BS step consists of an efficient algorithm that performs the subtraction of a stored background, at pixel level: 50 frames of a static scene in the absence of human workers are initially captured and the mean value of each pixel is stored in a memory area. Therefore, the stored frame is subtracted from the current frame at every acquisition.

The algorithm makes use of PCL: the depth information is converted into Point Cloud Data (PCD) and a uniform sampling filter can be applied to make the algorithm more reactive, by decreasing the PCDs density.

Subsequently, a reference camera has been selected to express the entire output of the perception system relative to a single camera frame, in this case, the Kinect camera. The point clouds have been combined through the *merging step* (MS). The accuracy reached during the extrinsic calibration procedure, described in Section 3.1, allowed to obtain a satisfying correspondence.

Finally, the *clustering process* (CP) provides as many clusters as single dynamic areas are detected in the foreground. The *Euclidean cluster extraction* method is performed to highlight all the human clusters of the collaborative workspace. The bottom right image of Figure 3 shows three detected human operators, whose shapes are distinguishable by different colors. To compensate the sensors measurement noise that could sometimes provide false clusters, the areas in the foreground should be large enough to represent a human body. Therefore, a valid cluster should have a minimum PCD cardinality, empirically determined.

3.3 Human-Robot Separation Distance

The goal of the proposed HRC strategy is to identify the nearest pair of points, one belonging to the robot (P_R) and the other one belonging to the operator (P_H), that minimize the distance, i.e.,

$$P_H \in \mathcal{H}, P_R \in \mathcal{R} \mid d(P_H, P_R) \leq d(P'_H, P'_R) \quad \forall P'_H \in \mathcal{H}, P'_R \in \mathcal{R} \tag{4}$$

where $d(\cdot,\cdot)$ is the Euclidean distance between two points, $\mathcal{H}$ and $\mathcal{R}$ represent the set of all points that belong to the operator and to the robot, respectively.

Therefore, alongside the HDT strategy, a robot modeling method has been also implemented. To the best of authors knowledge, the typical SoA assumption is to consider only a representative elements of the robot (e.g., the end effector), introducing only an approximate estimation of the distance between the operators and the robot kinematic chain. Other solutions report the pose of the robot only in terms of either joint configurations or in terms of the Cartesian pose of the robot link frames, without taking into account the link shapes but considering only specific points. On the contrary, the proposed solution models the entire robot kinematic chain with its volume. A computationally efficient way to represent the whole robot is to use primitive shapes, e.g., ellipses and spheres (Choi and Kim, 1999). A similar convention was proposed in (Bosscher and Hedman, 2009) . This work is inspired by the same idea, but pays attention to some aspects: since the robot links can have different lengths, its kinematic chain has been padded through dummy frames to protect the robot homogeneously, and a 0.10 m diameter security sphere has been created around each frame, taking into account the last frame that can incorporate an end-effector tool.

Under such assumptions, the pair of human-robot points that are closest to each other can be immediately identified. This step strongly justifies the choice of a point cloud-based pipeline. In fact, the point cloud provides much more detailed information, accuracy and precision if compared to the major HDT techniques present in the SoA literature cited in Section 1. Unlike common skeleton-based techniques, the proposed approach allows tracking humans also when they are carrying objects. Moreover, it is not necessary that human operators are in front of the camera view: the point cloud will recognize them anyway. Furthermore, detecting the pair of human-robot points at minimum distance (4) is particularly immediate. The algorithm calculates the distance between all points of a cluster point cloud and the origin of every robot frame. Eventually, the robot point P_R will be the one on the surface of the virtual sphere, around the identified frame, which lies on the line connecting the origin of this frame and the closest point in the cluster. From these results, the closest human cluster is indirectly selected if more than one human have been detected.

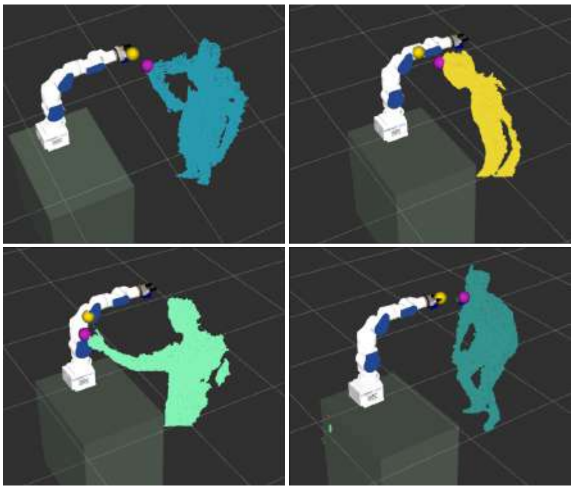

Figure 4: Identification of the minimum distance points: the yellow sphere is the robot point closest to the human and the purple one is the human point closest to the robot.

Figure 4 shows the results. Note that the proposed approach is able to identify more detailed body parts, e.g., a elbow, the head, an hand, the chin or the chest, and also that P_R can be detected along the whole robot kinematic chain. Figure 5 demonstrates the effectiveness of the proposed approach in multi-humans scenarios. The results of the experimental tests described in Section 6 will be used to evaluate the performances of the algorithm.

3.4 Estimation of Operator and Robot Velocities

Another fundamental function of the HRC problem is represented by IE, i.e., the prediction of human movement. From such information, the robot control system will select the most appropriate value of its joint

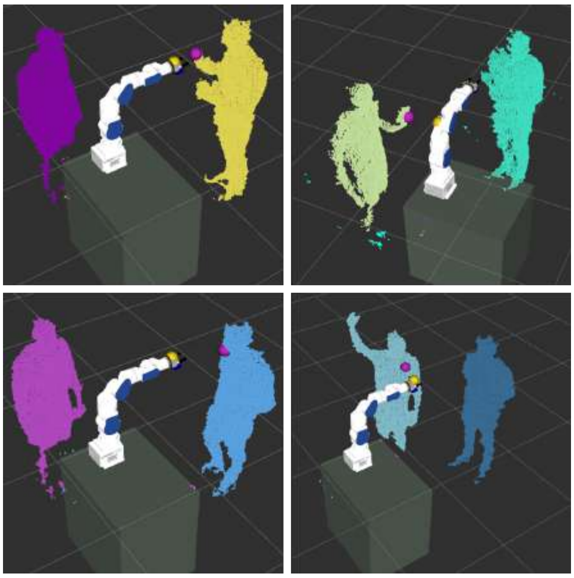

Figure 5: Multi-humans tracking.

speeds to avoid a potentially dangerous situation, as explained in Section 5.

IE consists in estimating the next position and velocity of the trajectory performed by the operator on the basis of a series of positions previously acquired.

The sensor fusion strategy that has been integrated into this work is based on a Linear Kalman Filter (LKF), which tries to solve the problem of estimating the state of a discrete-time process governed by the equations

$$\boldsymbol{x}_{k+1} = \begin{bmatrix} \boldsymbol{I}_3 & \Delta t \boldsymbol{I}_3 \\ \boldsymbol{O}_3 & \boldsymbol{I}_3 \end{bmatrix} \boldsymbol{x}_k + \boldsymbol{w}_k, \tag{5}$$

$$\boldsymbol{y}_k = \begin{bmatrix} \boldsymbol{I}_3 & \boldsymbol{O}_3 \end{bmatrix} \boldsymbol{x}_k + \boldsymbol{n}_k \tag{6}$$

where Δt is the sampling time, $\boldsymbol{I}_3$ and $\boldsymbol{O}_3$ are the identity and zero matrices of size 3×3, respectively; $\boldsymbol{w}$ and $\boldsymbol{n}$ are the process and measurement noises with covariance matrices $\boldsymbol{W}$ and $\boldsymbol{N}$, respectively. Finally, $\boldsymbol{x}$ is the state vector of the system, i.e., the position and the velocity of the operator $\boldsymbol{x} = \begin{bmatrix} \boldsymbol{p}_H^T & \dot{\boldsymbol{p}}_H^T \end{bmatrix}^T$, and the measured output $\boldsymbol{y}$ is a vector containing the coordinates of the point P_H described in Section 3.3. The covariance matrix $\boldsymbol{N}$ is experimentally estimated, while the covariance matrix $\boldsymbol{Q}$ has been chosen as

$$\boldsymbol{Q} = \begin{bmatrix} \boldsymbol{I}_3 \Delta t^2 & \boldsymbol{O}_3 \\ \boldsymbol{O}_3 & \boldsymbol{Q}_2 \end{bmatrix} \tag{7}$$

where $\boldsymbol{Q}_2$ quantifies the uncertainty on the velocity dynamics (assumed constant) of the state equations.

Based on the vector nature of the velocity, it is possible to make some considerations about the direction (trend) of the operator, that is to say, to predict in which direction he/she is travelling to. Section 4 describes how to take advantage from these considerations for industrial collaborative applications with the aim to maximize productivity.

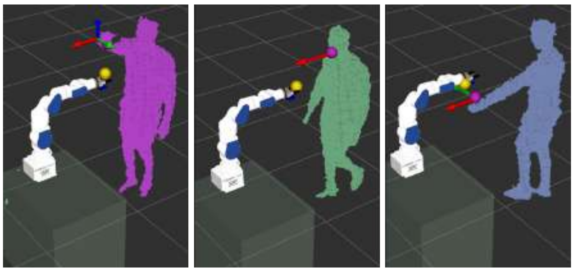

Figure 6: Estimation of operator velocity.

The LKF equations implemented in this work are the standard ones and thus are not reported for brevity, while the tuned parameters are fully described in Section 6.

Figure 6 shows sample movements of the operator and the three components of his/her estimated speed.

The linear velocity $\dot{\boldsymbol{p}}_R$ of the point on the robot closest to the operator can be computed according to the differential kinematics equation

$$\dot{\boldsymbol{p}}_R = \boldsymbol{J}_p(\boldsymbol{q})\dot{\boldsymbol{q}}, \tag{8}$$

where $\boldsymbol{q}$ [rad] and $\dot{\boldsymbol{q}}$ [rad/s] are the robot joint position and velocity vectors, respectively; while, $\boldsymbol{J}_p$ is the position part of the Jacobian matrix calculated till the closest point.

The (ISO/TS 15066, 2016) states that the "directed speeds" of the robot and the human should be used to compute S. This means that, in eq. (3), v_h is the operator speed in the direction of the moving part of the robot and v_R is the robot speed in the direction of the selected operator. Note also that these speeds are vector magnitudes, hence they are always grater or equal to 0. Therefore, the velocity terms of (3) can be computed as

$$v_H = \left| \dot{\hat{\boldsymbol{p}}}_H^T \left(\frac{\boldsymbol{p}_R - \hat{\boldsymbol{p}}_H}{\|\boldsymbol{p}_R - \hat{\boldsymbol{p}}_H\|} \right) \right| \tag{9}$$

$$v_R = \left| \dot{\boldsymbol{p}}_R^T \left(\frac{\hat{\boldsymbol{p}}_H - \boldsymbol{p}_R}{\|\hat{\boldsymbol{p}}_H - \boldsymbol{p}_R\|} \right) \right|, \tag{10}$$

where $\hat{\boldsymbol{p}}_H$ and $\dot{\hat{\boldsymbol{p}}}_H$ are the operator position and velocity estimated by the LKF, respectively, and $\boldsymbol{p}_R$ is a vector containing the coordinates of the point P_R defined in Section 3.3.

4 FUZZY INFERENCE SYSTEM

The protective separation distance S in (3), computed by using the speeds of (9)–(10), does not take into account the relative travel direction of the robot and the operator. This means that, if the robot and the operator are going away from each other, the value of S unnecessarily increases (proportionally to the computed speed). To improve the production time considering also this situation, the protective separation distance has been redefined as follows

$$S = \alpha[(v_H T_R + v_H T_S) + (v_R T_R)] + (B) + (C + Z_S + Z_R), \tag{11}$$

where α is a coefficient in the interval $[0,1]$ that is 1 when the operator and the robot are actually approaching to each other and is smaller than 1 otherwise.

To chose the value of α, a fuzzy inference approach has been implemented. The fuzzy logic, also called *faded logic*, is a methodology in which each proposition possesses a degree of truth into the interval $[0,1]$ (Ross, 2010). The variable α must be classified taking into account some qualitative attributes and it may have varying levels of validity between a maximum (1) and a minimum (0). Hence, it is necessary to generate linguistic rules of fuzzy inference to realize a mapping of the inputs to the desired output.

The fuzzy inference process has been developed as a two-input, one-output, three-rule problem, as shown in Figure 7.

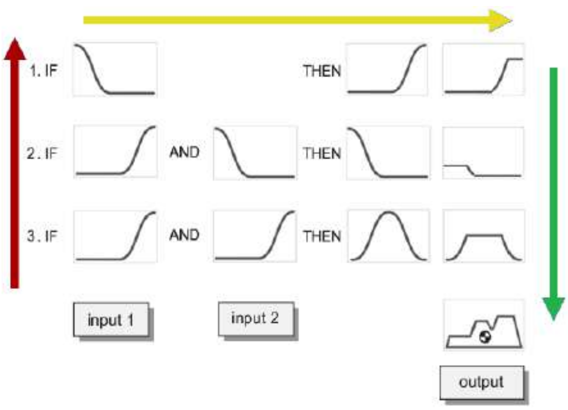

Figure 7: Fuzzy inference system: the fuzzification step (red arrow), the implication step (yellow arrow) and the aggregation step (green arrow).

The first step is to select the inputs. Two data inputs have been selected:

1. the time derivative of the distance between human and robot, i.e., $\dot{d} = \frac{\mathrm{d}\|\hat{p}_H - p_R\|}{\mathrm{d}t}$;
2. the scalar product between the robot and the human velocity vectors, i.e., $\dot{p}_R^T \dot{\hat{p}}_H$.

The first input is useful to distinguish cases when the operator and the robot are getting closer and cases when they are moving away from each other. The scalar product specifies the relative direction of travel of the operator and the robot.

The next step is the *fuzzification step* (red arrow of Figure 7). The ranges of variability of each input have been defined, and the appropriate membership function of each interval has been selected. This step requires attention to correctly determine the degree to which the input belongs to each of the appropriate fuzzy set, by assigning a fuzzy degree of membership in the interval from 0 to 1. Two membership functions have been selected to represent positive (P) and negative (N) values, a Z-shape and a S-shape, respectively. These functions, with different parameters, have been chosen to describe both $\dot{p}_R^T \dot{\hat{p}}_H$ and $\dot{d}$.

After the inputs are fuzzified, the *implication step* (yellow arrow of Figure 7) determines the degree to which each part of the antecedent is satisfied for each rule. The antecedent of the developed fuzzy inference rules has three parts, combined through an AND method (*min*) to obtain an implicated number that represents the result of the rule antecedent. Each rule is designed to consider one possible risk scenario.

Since the final decision is based on the result of all the tested rules, the outputs of the rules must be combined in some way. The *aggregation step* (green arrow of Figure 7) is the process by which the fuzzy sets representing the outputs of each rule are combined into a single fuzzy set, before the last *defuzzification step*. For each interval of the consequent, the maximum value of the fuzzy set is chosen and the defuzzification method is the centroid, as shown at the end of Figure 7.

The output value, α, has been generated by analyzing different possible risk situations, with the twofold aim of avoiding any collisions between human and robot, and being in line with the current ISO/TS 15066. With reference to the second rule: if the human-robot distance is increasing and they are moving further from each other, than the safety distance can be decreased. The three rules are summarized in Table 1.

Table 1: Fuzzy rules: [S] Small, [M] Medium, [H] High, [N] Negative, [P] Positive, [$\sim$] any.

antecedent		consequent
$\dot{d}$	$\dot{p}_R^T \dot{\hat{p}}_H$	α
N	$\sim$	H
P	N	S
P	P	M

Note that the scalar product between the operator velocity and the robot velocity (second input) is a complementary information to the time derivative of the distance between human and robot (third input). Since $\dot{p}_R^T \dot{\hat{p}}_H = \|\dot{p}_R\| \|\dot{\hat{p}}_H\| \cos\theta$, when $\theta = 180°$,

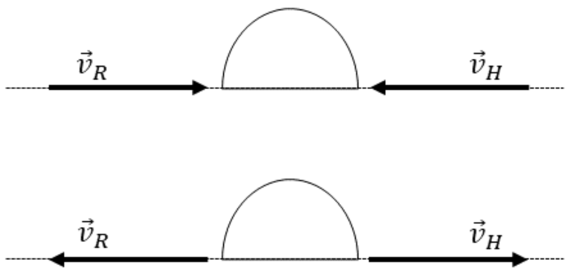

Figure 8: Problem of the scalar product.

a critical situation is possible. The result of the scalar product is negative, $\dot{\boldsymbol{p}}_R^T \hat{\dot{\boldsymbol{p}}}_H < 0$, but it is not possible to distinguish the cases shown in Figure 8, in which the directions are opposite but it is not known if the human and the robot are getting closer or are moving away from each other. This is the reason why it is necessary to combine the scalar product information with the time derivative of the distance between the human operator and the robot.

5 TRAJECTORY SCALING

SSM scenarios usually sacrifice the production time because a lot of time is spent in low speed mode when a human operator is inside the collaborative workspace. On the contrary, the proposed strategy ensures human-robot coexistence according to the standard regulations, and also guarantees the task efficiency by using a time-scaling approach to change robot operating speed without introducing acceleration discontinuities.

A typical industrial pre-programmed task, $\mathcal{T}$, is composed by N positions $\tilde{q}_i$, associated to velocities $\dot{\tilde{q}}_i$, accelerations $\ddot{\tilde{q}}_i$ and time instants $\tilde{t}_i$ with $i = 1,\ldots,N$. Typically, the pre-programmed joint positions have to be interpolated according to the sampling time T_c required by the robot control interface. In this work a quintic interpolation is used, i.e., the planned interpolated trajectory is

$$\tilde{q}_h = p_5(t_h; \mathcal{T}) \tag{12}$$
$$\dot{\tilde{q}}_h = p_4(t_h; \mathcal{T}) \tag{13}$$
$$t_{h+1} = t_h + T_c, \tag{14}$$

where t_h is the h-th discrete time instant, p_4 is the derivative of the polynomial p_5, $\tilde{q}_h$ and $\dot{\tilde{q}}_h$ are the *planned* joint position and velocity at time t_h, respectively.

The proposed method modulates the robot speed by scaling the time with a *safety scale factor* k, which can assume values in the interval $[0,1]$. The scale factor is related to d (Section 3.3) as shown in Figure 9.

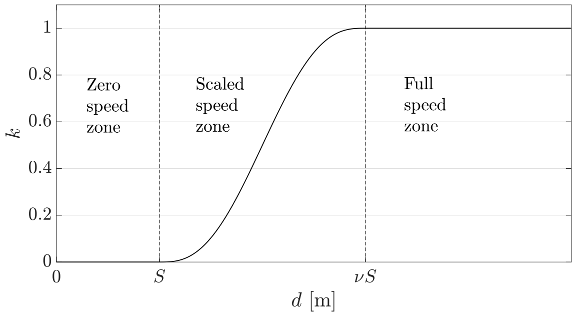

Figure 9: Relation between d and k.

When d is below the minimum protective distance S, k is 0 and the robot stops. When the distance d is far from S, i.e. $d > \nu S$ ($\nu > 1$), the robot can move at full speed to improve the production time. Between S and νS the function in Figure 9 smoothly varies to avoid acceleration discontinuities. Obviously, ν is another design parameter that changes the size of the scaled speed mode zone.

Practically, the trajectory is scaled computing (12) using a scaled time τ_h, i.e.,

$$q_h = p_5(\tau_h; \mathcal{T}) \quad \tau_{h+1} = \tau_h + kT_c, \tag{15}$$

where q_h is the actual joint command at time t_h. Obviously, the joint command q_h, as well as the scaled time τ_h, are generated with sampling time T_c.

This approach effectively scales the joints velocities. In fact, using (15), it is

$$\dot{\tau} \approx \frac{\tau_{h+1} - \tau_h}{T_s} = k. \tag{16}$$

By time differentiating (15), (17) demonstrates that the velocity is scaled by the *safety factor* k,

$$\dot{q}_h = p_4(\tau_h; \mathcal{T})k.. \tag{17}$$

This approach guarantees that the task $\mathcal{T}$ remains the same in position, but, simultaneously, the resulting velocity is scaled according to k.

When the operator is going to be into a dangerous situation, the robot operates at diminished capacity with limits on velocity that respect human-robot collaboration norms, until restoration of the safety conditions. Note that the side effect of the velocity reduction is the reduction of the minimum protective distance S, since this value is proportional to the robot velocity. Experimental results are shown in Section 6.

6 EXPERIMENTAL RESULTS AND VALIDATION

This section shows an example of experimental results obtained by simulating an SSM human-robot collaboration task inside the collaborative workspace of Figure 2. A manufacturing industrial sealing operation has been virtually realized: the robot executes a pre-planned path at a given nominal speed, while, suddenly, a human operator enters the collaborative workspace to perform some manual operation close to the robot, at different distances.

The main goal of this experiment is to prove the efficiency of the fuzzy inference approach into industrial applications to better handle the production time and, at the same time, to guarantee the safety of the operators when they are inside the collaborative workspace.

Table 2 summarizes the used hardware and the experimental case study.

Table 2: Case study and available hardware.

Robot	Yaskawa SIA5F
Collaborative workspace	4x2 m
Depth camera (1)	Microsoft Kinect v1
Depth camera (2)	Intel RealSense D435
Robot simulated task	Sealing operation
Operator simulated task	Manual piece change

The covariance matrix $\boldsymbol{Q_2}$ in (7) has been chosen as

$$\boldsymbol{Q}_2 = \mathrm{diag}(0.02,\ 0.05,\ 0.05)\,\mathrm{m}^2/\mathrm{s}^2, \qquad (18)$$

while the noise covariance has been estimated by acquiring a constant human position as

$$\boldsymbol{N} = \mathrm{diag}(0.0009,\ 0.0008,\ 0.001)\,\mathrm{m}^2. \qquad (19)$$

The parameters to compute the protective separation distance S of (3) and (11) are reported in Table 3. The value of C has been chosen to better appreciate the zero speed zone.

Table 3: Constant parameters of S.

T_R	0.10 s
T_S	0.08 s
B	0.563 mm
Z_R	0.001 m
Z_S	0.1067 m
C	0.20 m

Figure 10 shows the results of the experiment. The graph at the top of the figure shows the distance between the human operator and the robot and it can be compared with the minimum protective distance computed as in 3 (S_{ISO} in the legend) and the two thresholds proposed in this paper: S in the legend is the protective distance computed as in (11) and νS is the threshold used in the trajectory scaling algorithm (Section 5). The bottom plot of Figure 10 shows the two inputs of the fuzzy inference system ($\dot{d}$ and $\dot{\boldsymbol{p}}_R^T\dot{\boldsymbol{p}}_H$) and the trajectory scale factor k. In this experiment S_{ISO} is not used and it is showed in the plot for comparison purposes. A video of the experiment is available at `https://youtu.be/RzLZ6RQBPCY`.

The robot executes a planned task, suddenly (at about 16 s) an operator enters into the workspace simulating a manual task. This is visible in the top plot of Figure 10, where the human-robot distance decreases. Note that for almost the whole task duration the separation distance robot-operator is below the S_{ISO} signal, this would have caused frequent starts and stops of the robot. Instead, through the proposed trajectory scaling algorithm, the robot reduces its velocity according to the observed separation distance. This is visible in the k signal of the bottom plot that varies according to d. Notice that k goes to 0 only when the distance d goes below the protective distance S. Moreover, another property of the proposed solution is that S increases only when the distance decreases (i.e., when $\dot{d} < 0$) and not when the distance increases. This is due to the computation of the directed speed and the fuzzy rules. The shown experiment and the related video demonstrate how the proposed approach guarantees a safe human-robot coexistence in the collaborative workspace. This is achieved both in accordance with the ISO/TS regulations and minimizing dead times in the production process.

7 CONCLUSIONS

The human-robot interaction and their intentions to compete or cooperate in collaborative workspaces are challenging research fields. The purpose of this work is to improve the current regulations both to maximize the production time and guarantee the safety of human operators inside the shared workspace. The expected human movements relative to the robot are classified to identify all possible industrial SSM scenarios from which fuzzy rules for the robot reactions are derived. Collisions between robot and human operators are avoided by identifying human-robot intersections through a detection algorithm which processes data obtained by merging two depth camera images. Results obtained from experimental data show the applicability of the presented methods to many common manufacturing industry applications.

ACKNOWLEDGEMENTS

This work has received funding from the Clean Sky Horizon 2020 Programme under the LABOR project, grant agreement n. 785419.

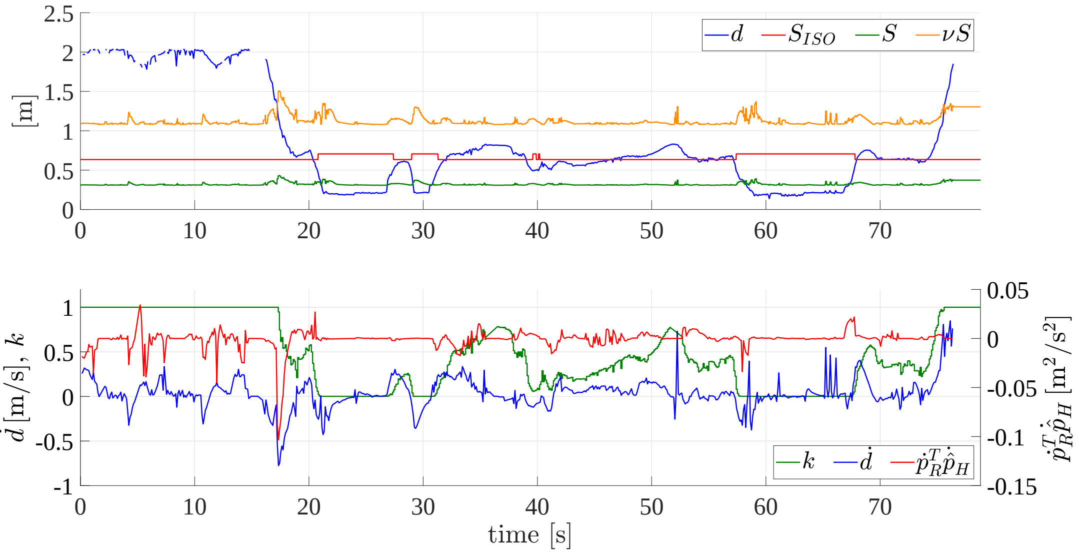

Figure 10: Experiment: an operator enters the shared workspace while the robot is moving. The top plot shows the estimated distance robot-operator (d), the protective distances proposed by the regulation without sensing (S_{ISO}) and the protective distances proposed by the paper (S and νS). The bottom plot shows the trajectory scaling factor k, the time derivative of the distance $\dot{d}$ and the scalar product of velocities.

REFERENCES

Bascetta, L., Ferretti, G., Rocco, P., Ardo, H., Bruyninckx, H., Demeester, E., and Lello, E. D. (2011). Towards safe human-robot interaction in robotic cells: An approach based on visual tracking and intention estimation. In *2011 IEEE/RSJ International Conference on Intelligent Robots and Systems*. IEEE.

Bicchi, A., Peshkin, M. A., and Colgate, J. E. (2008). Safety for physical human–robot interaction. In *Springer Handbook of Robotics*, pages 1335–1348. Springer Berlin Heidelberg.

Bjerkeng, M., Falco, P., Natale, C., and Pettersen, K. Y. (2014). Stability analysis of a hierarchical architecture for discrete-time sensor-based control of robotic systems. *IEEE Transactions on Robotics*, 30(3):745–753.

Blodow, N. (2012). Realtime urdf filter.

Bosscher, P. and Hedman, D. (2009). Real-time collision avoidance algorithm for robotic manipulators. In *2009 IEEE International Conference on Technologies for Practical Robot Applications*. IEEE.

Choi, S. I. and Kim, B. K. (1999). Obstacle avoidance control for redundant manipulators using collidability measure. In *Proceedings 1999 IEEE/RSJ International Conference on Intelligent Robots and Systems. Human and Environment Friendly Robots with High Intelligence and Emotional Quotients (Cat. No.99CH36289)*. IEEE.

Fischler, M. A. and Bolles, R. C. (1981). Random sample consensus: a paradigm for model fitting with applications to image analysis and automated cartography. *Communications of the ACM*, 24(6):381–395.

IEC 60204-1 (2009). Safety of machinery - Electrical equipment of machines - Part 1: General requirements. Technical report, International Electrotechnical Commission.

ISO 10218-1 (2011). Robots and robotic devices - Safety requirements for industrial robots. Part 1: Robots. Technical report, International Organization for Standardization.

ISO 10218-2 (2011). Robots and robotic devices - Safety requirements for industrial robots. Part 2: Robot system and integration. Technical report, International Organization for Standardization.

ISO 13855 (2010). Safety of machinery - Positioning of safeguards with respect to the approach speeds of parts of the human body. Technical report, International Organization for Standardization.

ISO/TS 15066 (2016). Robots and robotic devices - collaborative robots. Technical report, International Organization for Standardization.

Lippi, M. and Marino, A. (2018). Safety in human-multi robot collaborative scenarios: a trajectory scaling approach. *IFAC-PapersOnLine*, 51(22):190–196.

Ross, T. J. (2010). *Fuzzy Logic with Engineering Applications*. John Wiley & Sons, Ltd.

Rusu, R. B. and Cousins, S. (2011). 3d is here: Point cloud library (PCL). In *IEEE International Conference on Robotics and Automation*. IEEE.

The LABOR project (2019). https://www.labor-project.eu/.

Torr, P. and Murray, D. (1997). The development and comparison of robust methods for estimating the fundamental matrix. *International Journal of Computer Vision*, 24(3):271–300.

Zhang, P., Jin, P., Du, G., and Liu, X. (2016). Ensuring safety in human-robot coexisting environment based on two-level protection. *Industrial Robot: An International Journal*, 43(3):264–273.

CLEANSKY2 GREEN REGIONAL AIRCRAFT

CONCEPT DI CELLA ROBOTICA LABOR

Robotica lean e adattativa per l'aeronautica

Un progetto tutto italiano per assemblare componenti di pannelli in composito di fusoliera grazie alla robotica

La robotica è la strada da seguire per aumentare la produttività dell'industria aeronautica: ma in questo settore la sua adozione è ancora relativa (a causa dei rigidi requisiti e delle difficoltà nelle operazioni da svolgere), e quindi le sfide aperte sono molte. Una di queste riguarda la possibilità di introdurre robot di media taglia a coesistere con l'operatore. È l'obiettivo di "LABOR", un progetto inserito nel programma Clean Sky 2 dalla partnership tutta italiana: lo coordina Loccioni, ha per partner l'Università di Salerno e l'Università della Campania "Luigi Vanvitelli", e come Topic Manager, lato Clean Sky 2 Joint Undertaking, LEONARDO Aircraft. Il progetto porterà alla costruzione, installazione e validazione di una cella robotica lean - basata su diversi componenti intelligenti che agiscono come sistemi Cyber Physical, ovvero con flessibilità, modularità, autonomia, affidabilità, sicurezza ed efficienza - per l'assemblaggio di componenti di pannelli in composito di fusoliera. Due robot si adatteranno all'ambiente in cui operano e alle operazioni da fare, integrando sistemi di controllo della qualità delle operazioni; e mediante sistemi di visione artificiale, per guidare in maniera autoadattativa la lavorazione (grazie alla scansione in tempo reale dei componenti) e per verificarne la qualità. Una soluzione che consente agli operatori umani di condividere l'area con i robot durante il processo di produzione: uno degli aspetti chiave dell'Industria 4.0.

"Per noi è davvero un progetto sfidante, che ci dà la possibilità di fare un salto tecnologico, in linea con i trend che vive oggi l'aeronautica: e potrebbe rappresentare una pietra miliare per chi lo ha commissionato", confermano Cristina Cristalli e Alessandro Ragnoni, responsabili rispettivamente di Innovazione e Aerospace per Loccioni.

Il progetto è al primo dei tre anni previsti. "Per ora abbiamo definito tutte le parti funzionali della cella robotica: nel secondo anno passeremo all'implementazione, e in quello conclusivo installeremo la cella nello stabilimento di Pomigliano d'Arco della Leonardo S.p.A., con i due robot che faranno le operazioni sui pannelli della fusoliera.

Il progetto LABOR è finanziato (contratto n.785419) dalla CS 2 JU nell'ambito del programma di ricerca ad innovazione H2020 della Commissione Europea.

Funded by the Horizon 2020 Framework Programme of the European Union

A Multimodal Perception System for Detection of Human Operators in Robotic Work Cells*

Marco Costanzo, Giuseppe De Maria, Gaetano Lettera, Ciro Natale and Dario Perrone

Abstract— **Workspace monitoring is a critical hw/sw component of modern industrial work cells or in service robotics scenarios, where human operators share their workspace with robots. Reliability of human detection is a major requirement not only for safety purposes but also to avoid unnecessary robot stops or slowdowns in case of false positives. The present paper introduces a novel multimodal perception system for human tracking in shared workspaces based on the fusion of depth and thermal images. A machine learning approach is pursued to achieve reliable detection performance in multi-robot collaborative systems. Robust experimental results are finally demonstrated on a real robotic work cell.**

I. INTRODUCTION

The paper proposes a sensor fusion strategy which combines depth and thermal images to robustly detect human operators, e.g., in industrial work cells or in professional service robotics scenarios, and realize safe human-robot collaboration (HRC) tasks. The main focus of the current safety regulations is operators safety during industrial robotic operations. The safety standards for these applications are laid out by the International Organization for Standardization (ISO) 10218-1 [1], 10218-2 [2] and by the upcoming ISO Proposed Draft Technical Specification (TS) 15066 [3]. Four types of collaborative scenarios are identified, which are addressed in *post-collision* and *pre-collision* scenarios [4]. Industrial safety requirements do not permit to have the use of *post-collision* systems because the physical impact between the robot and the human operator occurs before the complete stop of the machinery. Otherwise, a *pre-collision* scheme makes use of appropriate exteroceptive sensors to detect humans and prevent collisions. A *Speed and Separation Monitoring* (SSM) scenario requires that the robot speed should be monitored according to the robot separation distance from the human operator. In this paper the SSM scenario has been selected with the aim to maximize the production time in industrial work cells or in any professional service task, and preserve human safety at the same time. However, it combines two uncertain worlds: the distance monitoring, which requires an accurate and robust human detection algorithm, and the robot speed monitoring, which should be reactive and efficient.

Distance monitoring can be solved through motion capture systems, range sensors or artificial vision systems [5]. Nevertheless, localizing human operators robustly is not an easy task. It is often necessary to fuse several sensors with different properties. Originally developed for military applications, thermal cameras provide relevant data to perform breast cancer diagnostic [6], infrastructure and electrical systems monitoring, gas or liquid detection [7], inspection and control tasks in industrial applications [8]. Thermal cameras are ideal for finding objects of a certain temperature: human detection and tracking (HDT) well fits for this case, as the body temperature is about 37°C. Unfortunately, thermal cameras do not support depth information, which are necessary to correctly compute the separation distance between the operator and the robot and apply the current regulations. The main difficulty of fusing spatial and thermal images is that a correspondence between corresponding pixels needs to be found. Similar sensor fusion approaches for indoor human detection combine RGB data with depth information [9], using the Histogram of Oriented Gradients (HOG) proposed in [10] together with depth feature that describes the self-similarity of an image. Different strategies are based on Convolutional Neural Networks (CNN), widely used for object recognition [11] and human detection [12]. A CNN-based RGB-D human detector exploiting the depth information to develop a region of interest selection method (ROI) is proposed in [13]. However, the fusion of thermal and spatial information has gained attention in the last few years, especially in fields where the spatial data are used as the main source of information [14], but nowadays there are no standardized methods to robustly combine them.

The State-of-Art (SoA) publications propose some methods to deal with the HRC safety: a volumetric representation of the areas occupied by operators and by the robot has been studied in [15] to stop the robot when these areas overlap; as well as, [16] proposes a potential field method to be used to generate a collision free path. A further approach is presented in [17] where a safety index is modeled to modify the robot trajectories and preserve the cooperative task. Many of these approaches rely on evasive actions to increase safety. However, in industrial setting, it is generally recommended to follow the robot predefined path without deviations.

This research paper tackles the HRC problem by introducing a novel approach to robustly detect human operators in collaborative work cells through a multimodal perception system aimed at minimizing false positives to avoid unnec-

*This work was supported by the European Commission under the H2020 Framework Cleansky 2 JTI – project LABOR, ID n. 785419 https://www.labor-project.eu.

M. Costanzo, G. De Maria, G. Lettera, C. Natale and D. Perrone are with Dipartimento di Ingegneria, Università degli Studi della Campania Luigi Vanvitelli, 81031 Aversa, Italy marco.costanzo@unicampania.it, giuseppe.demaria@unicampania.it, gaetano.lettera@unicampania.it, ciro.natale@unicampania.it, dario.perrone1@studenti.unicampania.it

 DOI: https://doi.org/10.1109/SMC.2019.8914519

essary robot stops. The paper guarantees human safety in general multi-robot scenarios. In fact, the algorithm allows computing the minimum separation distance between every human operator and every robot within the collaborative work cell, following the line of the current regulations. The applicability of the approach in the manufacturing industry has been obtained not by modifying the robot predefined path but by scaling down the robot trajectory only when indispensable, thus trying to maximize the production time even in presence of humans.

II. HUMAN-ROBOT SEPARATION DISTANCE

This section proposes a novel point-cloud based methodology to compute the separation distance between a moving robot and the closest human operator. Strong emphasis has been devoted to the proposed HDT strategy which realizes a robust algorithm to correctly detect human operators into a HRC scenario in real-time. According to the current ISOs, the robot speed must be modulated to eventually slow down the robot pre-programmed trajectory when a dangerous situation for the human operator occurs.

A. Experimental setup and camera calibration

Nowadays, thermal imaging provides relevant data to perform specific robotic applications that require thermal information. When combining two or more sources of acquisition, the resulting multi-sensor system has to be extrinsically calibrated to find the relative pose between the adopted sensors. This step can be performed by using a calibration target. The section explains two developed methods for camera calibration. The objective is to obtain the pose of the two cameras as accurate as possible both for the success of the next merging step and for the final separation distance computation. Two steps have been necessary.

The first one reliably localizes the pose of the depth camera with respect to the robot base frame. In literature, this problem is solved by different calibration procedures, especially for object recognition applications. Their typical target is to recognize objects located at about 0.5 m from the camera frame. On the contrary, for the proposed experimental application, the robot and the operators work about 2.5 m far from the camera. To obtain the desired accuracy, the novelty of the depth camera extrinsic calibration procedure consists in exploiting a sphere tracking as detailed below.

The experimental setup of this work is shown Fig. 1 and consists of two cameras rigidly attached to each other. They have been arranged in a way that their optical axes are aligned. The adopted cameras have different field of views (FOVs) and this implies that some depth pixels (*Microsoft Kinect v1*, Focal length: 6.1 mm, FOV: 57x45, image size: 640x480) are outside the thermal image (*Optris PI 450*, Focal length: 15 mm, FOV: 38x29, Spectrum: 7.5 to 13 m, image size: 382x288) and they are not used in the merging step (see Section II-C.1). The goal of the extrinsic calibration is to obtain an accurate identification of the camera poses, which guarantee the minimum accuracy error when the two camera views are merged.

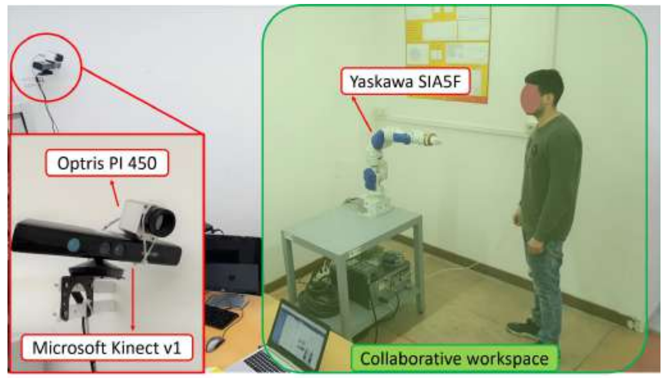

Fig. 1. The experimental perception system composed of a depth camera (Microsoft Kinect v1) and a thermal camera (Optris PI 450).

A 3D tracking technique has been developed to calibrate the depth sensor, by tracking a polystyrene sphere of 0.12 m diameter. The red sphere has been mounted at the robot end effector, so as to match the center of the sphere with the end effector frame origin. The developed procedure uses the *M-estimator SAmple Consensus* (MSAC) algorithm [18] (which is an extension of the best known *RANdom SAmple Consensus* (RANSAC) algorithm [19]), to find a sphere which satisfies a radius constraint and provides its geometric model. The robot has been positioned at specific configurations, which allow to correctly distinguish the target within the camera view. From the robot joint states, the forward kinematics immediately computes the position of the red sphere. At the same time, the developed procedure acquires the depth image, converts it into point-cloud data [20] (PCD) and estimates the target model. The method is iterated to try to cover the entire collaborative workspace and to minimize the calibration error. Finally, the transformation matrix $\boldsymbol{T}_d^r$, between the robot frame Σ_r and the depth camera frame Σ_d, has been evaluated through an optimization algorithm of a cost function, which combines the corresponding data.

After the depth camera calibration, the extrinsic calibration of the thermal camera with respect to the depth camera has been solved. In [21] and [22] a thermal camera and a depth camera are calibrated by using a perforated grid placed in front of the sensors. The procedures assume that the target is located close enough to the sensors lenses because the objective is to practically solve the calibration but the approach revealed unsuitable for the application scenario at hand. The solution consists in using three spheres attached to a flat cardboard support and heated to be distinguishable by both the depth and the thermal cameras.

To obtain an estimation of the transformation matrix $\boldsymbol{T}_t^d$, between the depth camera frame Σ_d and the thermal camera frame Σ_t, the spheres have been moved inside the collaborative workspace by placing the support in 10 configurations at distances from the camera in the range where the human operator is expected to act during the collaborative task. At every acquisition, the calibration target has been suitably heated to be detectable from both cameras. The coordinates $\boldsymbol{p}_k^d = \begin{bmatrix} x_k^d & y_k^d & z_k^d \end{bmatrix}^T$ of the kth center of the target sphere have been directly calculated from the depth image, while the corresponding thermal point coordinates have been calculated from the thermal image, assuming the distance from the lens equal to the depth value, i.e., $z_k^t = z_k^d$ and

$$x_k^t = \frac{(a_k - c_{x_t})z_k^t}{f_{x_t}} \tag{1}$$

$$y_k^t = \frac{(b_k - c_{y_t})z_k^t}{f_{y_t}}, \tag{2}$$

where a_k and b_k are the pixel coordinates of the sphere center in the thermal image, c_{x_t}, c_{y_t} are the pixel coordinates of the thermal image center and f_{x_t}, f_{y_t} are the focal lengths expressed in pixel-related units. Finally, the transformation matrix $\boldsymbol{T}_t^d$ has been estimated by minimizing a cost function that combines the corresponding data.

Note that, the intrinsic calibrations have been performed by using common patterns, i.e., a chessboard pattern for the depth camera and an heated circular pattern grid for the thermal camera. These procedures return the intrinsic calibration matrices of the cameras, thus, the parameters c_{x_t}, c_{x_d}, c_{y_t}, c_{y_d}, f_{x_t}, f_{x_d}, f_{y_t}, f_{y_t} (index d refers to the depth camera), which are needed to compute the PCD and (1)-(2).

B. Segmentation pipeline

The basic assumption of the proposed segmentation algorithm (blue pipeline in Fig. 2) is to process exclusively the information related to the dynamic objects present into the observed scene. This is because every point-cloud based strategy always represents a computationally heavy operation, then a *Background Segmentation* step has been initially adopted to subtract the static environment.

Section II-A describes the experimental setup in which the cameras monitor the surroundings of the manipulator and the robot kinematic chain is fully visible, as shown in Fig. 2A. While the collaborative workspace is observed, the robot executes its task, thus becoming a dynamic entity. Therefore, the package *Real-time URDF Filter* [23] has been integrated at the beginning of the pipeline to distinguish the depth pixels belonging to the robot model from those belonging to other dynamic entities and assign them a Not-a-Number (NaN) value, see Fig. 2B.

The background filtering has been developed through an efficient algorithm that performs the subtraction of a stored background, at pixel level: 50 frames of the static background are initially captured and the mean value of each pixel is stored in a memory area. At every acquisition, the current frame subtracts the static frame, as shown in Fig. 2C. The depth image is then converted to PCD and a uniform sampling filter is applied to make the algorithm more reactive, by reducing the clouds density. Finally, the detection of dynamic entities is executed through a *PCD Clustering* step, which processes the point-cloud scene and provides some clusters as many as single dynamic areas are detected in the foreground. The *Euclidean cluster extraction* method is performed to distinguish all the clusters into the collaborative workspace. Figure 2D shows two detected dynamic entities visualized in RViz together with the robot model. To compensate the sensors measurement noise that could sometimes provide false clusters, a first constraint is enforced by defining a minimum cardinality that the areas in the foreground should have, to be large enough to represent a human entity. However, the correct discrimination about validity of the cluster as a real human entity is done through a novel developed HDT algorithm described in Section II-C. The *Human Validation* step waits for the cluster check from the HDT pipeline, which executes the human detection as explained in Section II-C.

C. Human Detection and Tracking

The proposed human detection approach makes use of a Convolutional Neural Network (CNN), whose innovative input is obtained by combining depth and thermal images. The two information have been processed though a simple and intuitive pixel-by-pixel technique, never presented elsewhere. This choice did not allow the authors to use pre-existing data-sets and pre-trained CNNs but the CNN had to be trained with a novel, multi-sensory data-set.

A depth camera is suitable for different kinds of environments because of its adaptability to different lighting conditions: in this work it is adopted to compute the minimum distance between the human operator and the robot to apply regulations, but a depth image lets also to distinguish and localize human surface shapes and their volume, so it is appropriate to the HDT problem. On the other hand, the thermal camera distinguishes temperatures and it is ideal for finding objects of a specific temperature as the human body, which is about 37°C.

CNN solutions which process only thermal images can be often not sufficient in those applications where large, hot objects, e.g., tools used in the manual task or, more generally, small temperature gradients could be present. On the contrary, CNN trained to detect human shapes into pure depth images can confuse human operators with objects of similar shapes, e.g., a plastic mannequin, a coat rack, a lamp. Therefore, merging depth and thermal images makes the HDT approach more robust, avoiding false positives and making correct decisions about human classification. Moreover, the proposed CNN strategy allows also to correctly localize the human operators into the observed scene. This information is then sent to the segmentation pipeline to select who is the human cluster which is the closest to the robot and continue the computation of the separation distance from the manipulator. In these terms, thermal imaging is used as complementary information to spatial ones and represents a vision strategy that goes beyond SoA human detection approaches based on background subtraction.

1) Depth-Thermal mapping: The extrinsic calibrations explained in Section II-A are a first step towards a correct mapping, that means finding matches between the depth image and the thermal image. Since the adopted cameras have different FOVs and resolutions, the resulting map size must correspond to the smallest one. According to the experimental setup shown in Fig. 1, the mapping step builds

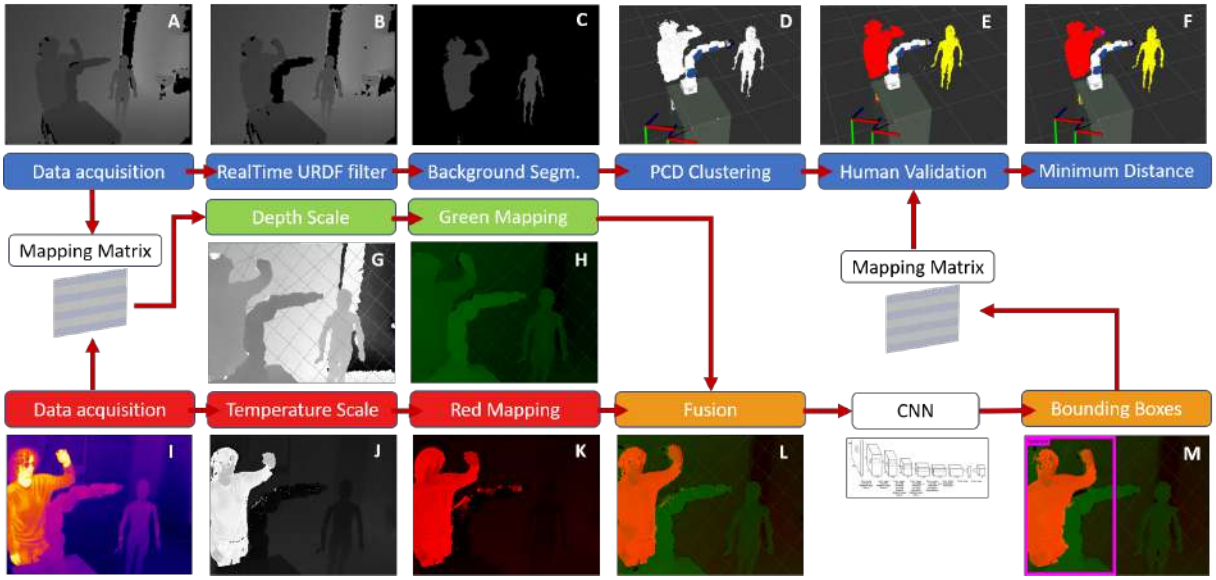

Fig. 2. Implemented human detection and tracking pipeline: the background segmentation (first three blue labels) processes the depth image to subtract the static environment and to highlight only dynamic shapes. At the same time, the depth image and the corresponding thermal image are merged into a single RGB channel (green and red labels, respectively). The obtained images are then combined through a mapping matrix to reliably localize workers (orange labels) and distinguish them from non-human clusters (human validation step); eventually, the minimum distance between the closest human operator and the robot is computed.

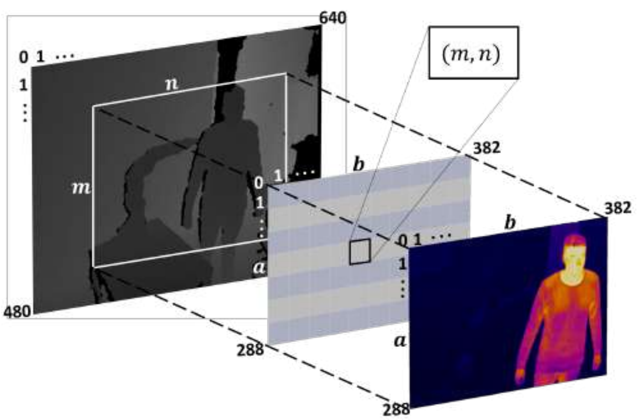

Fig. 3. The algorithm for mapping depth and thermal images finds pixel-by-pixel matches between the two images: the result is a 382×288 matrix.

a 382×288 matrix, the size of the thermal image shown in Fig. 3.

The mapping step has been solved through a pixel-by-pixel procedure: the pixel of the depth image, of indices (m,n), contains the depth value, $z^d_{m,n}$, which can be acquired to compute the corresponding Cartesian point coordinates $\boldsymbol{p}^d_{m,n} = \begin{bmatrix} x^d_{m,n} & y^d_{m,n} & z^d_{m,n} \end{bmatrix}^T$, similarly to (1)-(2),

$$x^d_{m,n} = \frac{(m - c_{x_d}) z^d_{m,n}}{f_{x_d}} \tag{3}$$

$$y^d_{m,n} = \frac{(n - c_{y_d}) z^d_{m,n}}{f_{y_d}}. \tag{4}$$

The Cartesian point is then expressed with reference to the thermal camera frame through the relation

$$\begin{bmatrix} \boldsymbol{p}^t_{m,n} \\ 1 \end{bmatrix} = \boldsymbol{T}^t_d \begin{bmatrix} \boldsymbol{p}^d_{m,n} \\ 1 \end{bmatrix}. \tag{5}$$

Using the intrinsic parameters of the thermal camera, the corresponding pixel indices of the point $\boldsymbol{p}^t_{m,n}$ into the thermal image (a,b) are finally computed by inverting (1)-(2). If they are contained in the FOV of the thermal image, the corresponding depth pixel indices (m,n) are written into the mapping matrix at the indices (a,b); otherwise, they are discarded because they are outside the mapping image size. Note that, if the observed object is far enough, the mapping matrix does not depend on the distance. Thus the mapping matrix can be computed offline by using a fixed value of $z^d_{m,n}$ compatible with the working area, hence saving computational load.

2) Sensor fusion: Multimodal sensor images can be combined through different image fusion techniques, which work at different merging levels: pixel-by-pixel, combining signals, using relevant features or at symbol levels. This paper provides an image fusion algorithm at pixel level but represents a novel approach with respect to the most widely used pixel-level image fusion algorithms [24] which never merge depth and thermal information.

The first requirement of the proposed sensor fusion approach is to preserve all valid and useful information from the two sources to be combined, while not introducing distortions. For the purpose of this work, the depth image and the corresponding thermal image have been merged to provide an enhanced single view of a scene with extended information content, through the mapping matrix of Section II-C.1. The proposed approach, callable *RGB Mapping Approach* (RGB-MA), consists in defining the intensities of empty RGB channels. This is also because, to the best of the authors knowledge, CNNs work better with RGB images. RGB-MA strength is that it assigns the same priority to the input sources. The result is no longer a grayscale, as a depth image alone could be, or a weighted average image which assigns different priorities to the sources, but it is an RGB image where the depth data have been mapped on the green channel (see Fig. 2H) and the temperature values have been mapped on the red channel (see Fig. 2K). Specifically, the original depth sensor value, s^d, and the corresponding temperature sensor value, s^t, have to be normalized into the interval $[0, 1]$ (see Fig. 2G and J). To do this, a *minimum* and a *maximum* variability ranges of the source values have been defined for both thermal, min_t, max_t, and depth, min_d, max_d, cameras. They do not actually correspond to the ranges of the sensors technical specifications, but they have been chosen according to the values detectable into the considered workspace. More in detail, the detectable depth values are included between 0.30 m and 4.0 m, while the detectable temperature values are within the range $[0, 50]^\circ$C, which are suitable for any type of human detection task.

The color information inserted into the specific channel of the *(i,j)-th* pixel of the output image must be mapped to 8 bits. The *R* (red) value is computed, by acquiring $s^t_{i,j}$ from the thermal image, as

$$R_{i,j} = \text{round}\left(255\frac{s^t_{i,j} - min_t}{max_t - min_t}\right); \quad (6)$$

the *G* (green) value is computed by acquiring $s^d_{m,n}$ from the depth image, where m and n are contained into the *(i,j)-th* value of the mapping matrix (Section II-C.1),

$$G_{i,j} = \text{round}\left(255\frac{s^d_{m,n} - min_d}{max_d - min_d}\right); \quad (7)$$

the *B* (blue) value of the resulting image is always zero.

The result is shown in Fig. 2L. Note that the proposed image fusion technique leaves another channel that could be used for a further input source. Section IV report the results of the approach for a typical SSM scenario.

3) CNN for Human Detection: To assess the effectiveness of the fused images of Section II-C.2, YOLOv3 [25] has been used for real-time human detection. The selected framework is an off-the-shelf SoA 2D object detector pre-trained on ImageNet [26] and fine-tuned on the MS-Coco [27] data-set. It is an extremely fast and accurate object detection system, which is born to detect semantic objects of a certain class, e.g., humans, buildings and cars, in RGB images. Nowadays, there are no neural networks which have been trained on combined images such as those proposed by this paper, so the YOLOv3 CNN model has been re-trained to adapt the detection system to the Depth-Thermal (D-T) images. The following steps have been executed:

- definition of a *Human class*;
- exclusion of the YOLOv3 pre-trained classes from the prediction;
- building of the training data-set acquiring frames from D-T video stream;
- manual labelling of each frame;
- retrain of the YOLOv3 CNN weights.

After the training step, the CNN has been applied to the real time D-T video stream to obtain the human prediction. A bounding box is estimated around each detected human and its coordinates are finally sent to the point-cloud pipeline, as shown in Fig. 2M. Note that both the training and the prediction process need high computational cost and they have been executed on a proper GPU (NVIDIA Titan V).

D. Human-Robot separation distance

Once the predicted bounding boxes are sent to the segmentation pipeline, each cluster is verified: each point of the cluster is transformed into depth pixel coordinates (by inverting (3)-(4)). Since the bounding box is expressed in the thermal image plane, the selected pixel is converted into depth image coordinates through the mapping matrix (Section II-C.1). If at least 50% of the cluster points belong to a bounding box, the cluster is labeled as human and passes the check. Figure 2E shows two clusters: the *red* human operator, which is correctly detected by the CNN, and the *yellow* plastic mannequin, which is correctly not labeled as human.

The *Human Validation* check is a fundamental step to compute the correct separation distance between human operators and the robot to apply the actual regulations of industrial robotic applications. Therefore, the last step of the segmentation pipeline (Fig. 2F) identifies the nearest pair of points, one belonging to the robot (P_R) and the other one belonging to the operator (P_H), that minimize the distance, i.e.,

$$\begin{aligned} P_H \in \mathscr{H}, P_R \in \mathscr{R} \mid d(P_H, P_R) &\leq d(P'_H, P'_R) \\ \forall P'_H \in \mathscr{H}, P'_R &\in \mathscr{R}, \end{aligned} \quad (8)$$

where $d(\cdot,\cdot)$ is the Euclidean distance between two points, $\mathscr{H}$ and $\mathscr{R}$ represent the set of all points that belong to the operator and the robot, respectively.

If P_H is detected through the HDT strategy, a robot modeling method has been implemented to detect P_R. To take into account the link volumes and not only specific points, the proposed solution uses spheres as in [28] and [29] to model robot links. The kinematic chain has been padded through 12 dummy frames to include the robot homogeneously, creating a virtual 0.10 m diameter safety sphere around each of them.

Therefore, the pair of closest points can be immediately identified: the algorithm calculates the distance between all points of the verified clusters point clouds and the origin of every robot frame. The robot point P_R will be on the closest virtual sphere along the line connecting the origin with P_H.

This step strongly justifies the choice of a point cloud based approach. In fact, it provides satisfactory accuracy and precision: it allows tracking humans also when they are not completely visible from the camera view, unlike common skeleton-based techniques; it is not necessary that human operators are in front of the camera view because the point

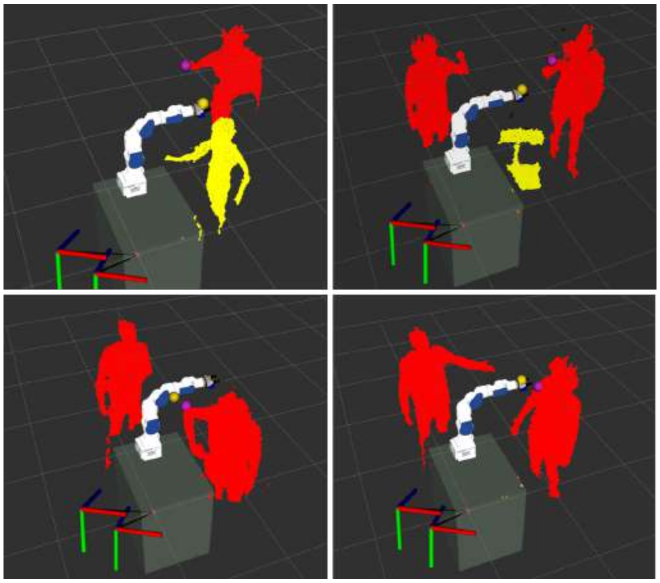

Fig. 4. Identification of the minimum distance points between the whole robot (yellow sphere) and the closest human operator (purple sphere).

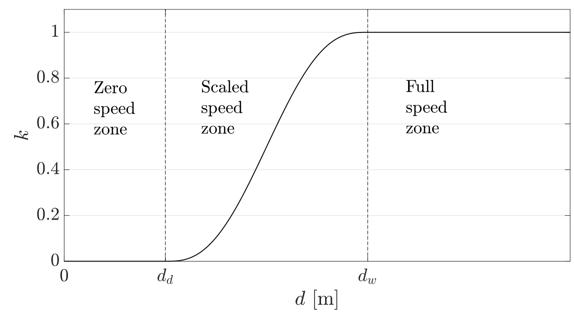

Fig. 5. Relation between the computed separation distance d (x axis) and the scale factor k (y axis).

cloud-based approach will recognize them anyway; more detailed body parts can also be detected, e.g., a elbow, the head, an hand, the chin or the chest. Figure 4 shows the results: the developed CNN distinguishes human operators belonging to the *Human class* (in red) from other clustered objects (in yellow), i.e., a plastic mannequin and a chair, which are not labeled as humans and they are not considered for the safety separation distance computation, even if they are possibly closer to the robot. Note that the closest human cluster is selected in case of many human operators.

III. TRAJECTORY SCALING

Industrial SSM scenarios allow the robot system and the human operator to move concurrently in the collaborative workspace. Risk reduction is achieved by maintaining at least the minimum protective separation distance, S, between the operator and the robot [3], assumed constant here. During robot motion, the robot system never gets closer to the operator than S. When the separation distance, d, is less than S, the robot system stops, before it can impact the operator. When the operator moves away from the robot system, it can resume the motion automatically while maintaining at least the protective separation distance.

The proposed strategy ensures human-robot coexistence according to the standard regulations methodology, introducing a low speed mode which slows down the robot nominal velocity when the operator is inside a hazardous workspace. The approach guarantees the robot task efficiency by using a time-scaling method to change robot operating speed without introducing acceleration discontinuities.

A. Single robot work cell

With reference to a single robot case, a typical industrial pre-programmed task, $\mathscr{T}$, is composed by N positions, $\tilde{\boldsymbol{q}}_i$, associated to velocities $\dot{\tilde{\boldsymbol{q}}}_i$, accelerations $\ddot{\tilde{\boldsymbol{q}}}_i$ and temporal instants $\tilde{t}_i$. Typically the pre-programmed joint positions have to be interpolated according to the sampling time T_c required by the robot. In this work a quintic interpolation is used, i.e., the *planned* interpolated trajectory is

$$\tilde{\boldsymbol{q}}_h = \boldsymbol{p}_5(t_h; \mathscr{T}) \tag{9}$$

$$\dot{\tilde{\boldsymbol{q}}}_h = \boldsymbol{p}_4(t_h; \mathscr{T}) \tag{10}$$

$$t_{h+1} = t_h + T_c \tag{11}$$

where t_h is the h-th discrete time instant, $\boldsymbol{p}_4$ is the derivative of the polynomial $\boldsymbol{p}_5$, $\tilde{\boldsymbol{q}}_h$ and $\dot{\tilde{\boldsymbol{q}}}_h$ are the *planned* joint position and velocity at time t_h respectively.

The proposed algorithm modulates the robot speed by scaling the time with a *safety scale factor* k, which can assume values inside the interval $[0,1]$. The scale factor is related to d (Section II-D) as shown in Fig. 5. When d is below the danger distance $d_d = S$, k is 0 and the robot stops. When the distance d is far from the warning distance $d_w > S$, i.e., $d > d_w$, the robot can move at full speed to improve the production time. Between d_d and d_w the function in Fig. 5 smoothly varies to avoid acceleration discontinuities.

Practically, the trajectory is scaled by computing (9) with a scaled time τ_h, i.e.,

$$\boldsymbol{q}_h = \boldsymbol{p}_5(\tau_h; \mathscr{T}) \tag{12}$$

$$\tau_{h+1} = \tau_h + kT_c \tag{13}$$

where $\boldsymbol{q}_h$ is the *actual* joint command at time t_h. Obviously, the joint command $\boldsymbol{q}_h$, as well as the scaled time τ_h, are generated with sampling time T_c. The effect of this approach is the actual scaling of the joints velocities. In fact, using (13),

$$\dot{\tau} \approx \frac{\tau_{h+1} - \tau_h}{T_s} = k. \tag{14}$$

By differentiation (12), the following equation demonstrates that the velocity is scaled by the *safety factor* k

$$\dot{\boldsymbol{q}}_h = \boldsymbol{p}_4(\tau_h; \mathscr{T})k. \tag{15}$$

This approach guarantees that the task $\mathscr{T}$ remains the same in position, but, simultaneously, the resulting velocity is scaled according to k. When the operator is going to be into a dangerous situation, the robot operates at diminished capacity with limited velocity according to human robot collaboration norms, until restoration of safety conditions. Experimental results are shown in Section IV.

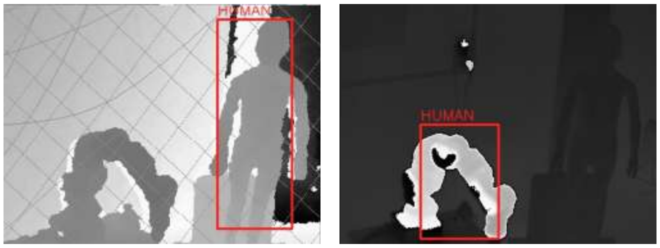

Fig. 6. Two cases of human false positives: a dummy labeled as human in the depth CNN approach (left); a hot moving robot labeled as human in the temperature CNN approach (right).

TABLE I
CNNs Testing Results

CNN	mAP %	False Positives %	False Negatives %
D-CNN	65.09	36.87	17.53
T-CNN	62.76	64.35	4.37
DT-CNN	57.54	2.47	11.85

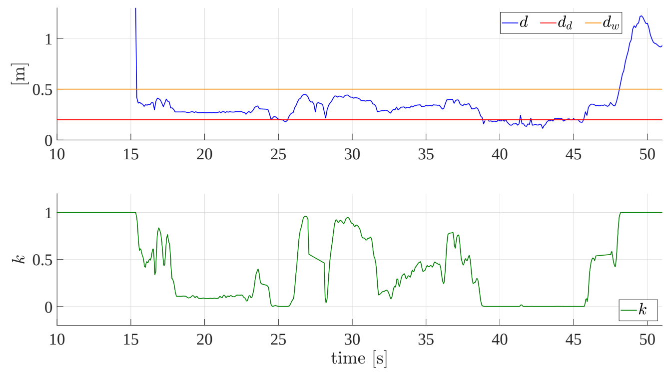

Fig. 7. Experiment: an operator enters the shared workspace while the robot is moving. The top plot shows the estimated distance robot-operator d, the dangerous distance d_d and the warning distance d_w. The bottom plot shows the trajectory scaling factor k adopted to scale the robot velocity.

B. Multi-robot work cell

The strategy discussed so far can be easily extended to multi-robot work cells. It is necessary to pay close attention to distinguish the independent robots case from the cooperating robots case.

If the work cell is composed by robots which execute independent taskseach robot must be slowed down according to the separation distance with the proper closest human operator. Thus, the whole pipeline proposed in this paper is executed for each robot and each robot speed is scaled independently from the others. This solution has a positive impact on the production time because it reduces the speed only of the robots involved in dangerous situations.

On the contrary, if the work cell is composed by cooperating robots, e.g., an assembly line or the transportation of a commonly held object as in [17],the application of the strategy to the single robots independently can compromise the task execution. Whereas, the perception pipeline must be executed for each robot worker until the computation of the scaling factors, Then, the scale factor corresponding to the most dangerous robot is applied to all the configuration variables of the whole robotic system to preserve the cooperative task. Suitable danger metrics can be defined to take this decision, e.g., the scale factor of the robot closest to the human can be selected.

IV. EXPERIMENTAL RESULTS

The section shows a complete experiment that represents a typical SSM collaborative scenario to describe the advantages of the approach. Emphasis has been devoted to the proposed DT-CNN to better highlight the performance.

A. Performances of DT-CNN

To test the performance of the *Sensor Fusion* approach, two others CNNs have been trained based on the depth (D-CNN) and temperature (T-CNN) information, respectively. The networks have been trained and tested with the same input data-set. Note that the training phase needed about 1000 training samples to reach the presented performance. This observation represents another great advantage of using the proposed approach if compared with many pre-trained CNNs, which usually needed tens of thousands of images to be trained.

The Mean Average Precision (maP) has been adopted as a metric to measure the accuracy of each CNN [30]. Considering the bounding boxes returned from the prediction and the ground truth, the estimation of mAP is based on the calculation of various metrics such as precision, recall and Intersection over Union (IoU). Since the mAP does not consider false positives and negatives, the percentage of the erroneous detection has been estimated as an additional metric.

Comparing the results of Table I, the DT-CNN provides a mAP slightly lower than other two methods since it is computed by considering only true positives. Whereas, the percentage of false positives is considerably lower than the others. In all cases the percentage of false negatives remains low. The high percentage of false positives of single-source approaches is to be found in cases where hot objects (T-CNN) or objects with shapes comparable to human ones (D-CNN) can be confused with a human (Fig. 6).

B. Complete experiment

To evaluate the combined approach (human detection and trajectory scaling) a SSM scenario has been experimentally tested. A video of the experiment is available at `https://youtu.be/BrcvKmSiR9Q`. A collaborative manufacturing industrial operation has been considered. The robot executes a pre-planned task at a given nominal speed. Suddenly, an operator enters the robot workspace to perform some manual operations (see the accompanying video). Results are shown in Fig. 7. At about 15 s the operator enters the collaborative workspace and the system starts to measure the separation distance d (blue line). When d goes below the warning distance d_w the trajectory scaling factor k becomes lower than 1 and the robot reduces its velocity without changing its path. In some intervals of the experiment d goes below the dangerous distance d_d thus k becomes 0 and the robot stops.

In the accompanying video the DT-CNN has been also compared with the networks that use single sources (depth or thermal). It is clear that the DT-CNN ensures a better human detection minimizing the false positives.

This experiment demonstrates how the proposed approach is able to automatically detect human operators in collaborative workspaces and modulate the robot velocity according to the current regulations.

V. CONCLUSIONS

This work shows a multimodal perception system based on a thermal and a depth camera adopted to detect human operators in general multi-robot work cells. The cameras have been coupled in a fixed way and calibrated. Results show that the calibration error is small enough to implement a new sensor fusion technique to process the camera images and robustly detect humans into the observed scenario. The fusion technique consists in defining an RGB image by combining depth and thermal images on two channels. The fused image is then processed by a CNN specifically trained to detect humans in the workspace. The approach based on the fused images has been demonstrated to be more efficient than single source perception data in a real collaborative scenario. Future developments will be devoted to devise an SSM strategy where, rather than assuming a constant minimum protective distance, it is computed based on the actual robot and human velocities estimated through the same perception data used for distance computation. A risk analysis based on the real velocity information can lead to the definition of a less conservative minimum protective distance, hence maximizing productivity.

REFERENCES

[1] "Robots and robotic devices - Safety requirements for industrial robots. Part 1: Robots." International Organization for Standardization" Technical report, 2011.

[2] "Robots and robotic devices - Safety requirements for industrial robots. Part 2: Robot system and integration." International Organization for Standardization" Technical report, 2011.

[3] "Robots and robotic devices - collaborative robots." International Organization for Standardization" Technical report, 2016.

[4] J. Heinzmann and A. Zelinsky, "Quantitative safety guarantees for physical human-robot interaction," *The International Journal of Robotics Research*, vol. 22, no. 7-8, pp. 479–504, jul 2003.

[5] F. Flacco, T. Kroger, A. D. Luca, and O. Khatib, "A depth space approach to human-robot collision avoidance," in *2012 IEEE International Conference on Robotics and Automation*. IEEE, may 2012.

[6] N. Arora, D. Martins, D. Ruggerio, E. Tousimis, A. J. Swistel, M. P. Osborne, and R. M. Simmons, "Effectiveness of a noninvasive digital infrared thermal imaging system in the detection of breast cancer," *The American Journal of Surgery*, vol. 196, no. 4, pp. 523–526, oct 2008.

[7] M. Vollmer and K.-P. Mllmann, *Infrared Thermal Imaging*. Wiley-VCH Verlag GmbH & Co. KGaA, dec 2017.

[8] H. Kaplan, *Practical Applications of Infrared Thermal Sensing and Imaging Equipment*. SPIE Publications, 2007.

[9] B. Li, H. Jin, Q. Zhang, W. Xia, and H. Li, "Indoor human detection using RGB-d images," in *2016 IEEE International Conference on Information and Automation (ICIA)*. IEEE, aug 2016.

[10] N. Dalal and B. Triggs, "Histograms of oriented gradients for human detection," in *2005 IEEE Computer Society Conference on Computer Vision and Pattern Recognition (CVPR'05)*. IEEE, 2005, pp. pp. 886–893 vol. 1.

[11] M. Liang and X. Hu, "Recurrent convolutional neural network for object recognition," in *2015 IEEE Conference on Computer Vision and Pattern Recognition (CVPR)*. IEEE, jun 2015.

[12] P. Sermanet, D. Eigen, X. Zhang, M. Mathieu, R. Fergus, and Y. LeCun, "Overfeat: Integrated recognition, localization and detection using convolutional networks," *CoRR*, vol. abs/1312.6229, 2013. [Online]. Available: http://arxiv.org/abs/1312.6229

[13] K. Zhou and A. Paiement, "Detecting humans in rgb-d data with cnns," in *15th IAPR International Conference on Machine Vision Applications (MVA), Nagoya University, Nagoya, Japan*. IEEE, 2017.

[14] S. Vidas, P. Moghadam, and M. Bosse, "3d thermal mapping of building interiors using an RGB-d and thermal camera," in *2013 IEEE International Conference on Robotics and Automation*. IEEE, may 2013.

[15] P. Rybski, P. Anderson-Sprecher, D. Huber, C. Niessl, and R. Simmons, "Sensor fusion for human safety in industrial workcells," in *2012 IEEE/RSJ International Conference on Intelligent Robots and Systems*. IEEE, oct 2012.

[16] P. Zhang, P. Jin, G. Du, and X. Liu, "Ensuring safety in human-robot coexisting environment based on two-level protection," *Industrial Robot: An International Journal*, vol. 43, no. 3, pp. 264–273, may 2016.

[17] M. Lippi and A. Marino, "Safety in human-multi robot collaborative scenarios: a trajectory scaling approach," *IFAC-PapersOnLine*, vol. 51, no. 22, pp. 190–196, 2018.

[18] S. Choi, T. Kim, and W. Yu, "Performance evaluation of ransac family," in *Procedings of the British Machine Vision Conference 2009*. British Machine Vision Association, 2009.

[19] C. Papazov and D. Burschka, "An efficient ransac for 3d object recognition in noisy and occluded scenes," in *Computer Vision – ACCV 2010*. Springer Berlin Heidelberg, 2011, pp. 135–148.

[20] R. B. Rusu and S. Cousins, "3d is here: Point cloud library (PCL)," in *IEEE International Conference on Robotics and Automation*. IEEE, may 2011.

[21] T. Luhmann, J. Piechel, and T. Roelfs, "Geometric calibration of thermographic cameras," in *Thermal Infrared Remote Sensing*. Springer Netherlands, 2013, pp. 27–42.

[22] J. Rangel and S. Soldan, "3d thermal imaging: Fusion of thermography and depth cameras," in *Proceedings of the 2014 International Conference on Quantitative InfraRed Thermography*. QIRT Council, 2014.

[23] N. Blodow, "Realtime urdf filter," 2012. [Online]. Available: http://github.com/blodow/realtime_urdf_filter

[24] B. Yang, Z. liang Jing, and H. tao Zhao, "Review of pixel-level image fusion," *Journal of Shanghai Jiaotong University (Science)*, vol. 15, no. 1, pp. 6–12, feb 2010.

[25] J. Redmon and A. Farhadi, "Yolov3: An incremental improvement," *CoRR*, vol. abs/1804.02767, 2018. [Online]. Available: http://arxiv.org/abs/1804.02767

[26] J. Deng, W. Dong, R. Socher, L.-J. Li, K. Li, and L. Fei-Fei, "ImageNet: A Large-Scale Hierarchical Image Database," in *CVPR09*, 2009.

[27] T.-Y. Lin, M. Maire, S. Belongie, J. Hays, P. Perona, D. Ramanan, P. Dollár, and C. L. Zitnick, "Microsoft COCO: Common objects in context," in *Computer Vision – ECCV 2014*. Springer International Publishing, 2014, pp. 740–755.

[28] S. I. Choi and B. K. Kim, "Obstacle avoidance control for redundant manipulators using collidability measure," in *Proceedings 1999 IEEE/RSJ International Conference on Intelligent Robots and Systems. Human and Environment Friendly Robots with High Intelligence and Emotional Quotients (Cat. No.99CH36289)*. IEEE, 1999.

[29] P. Bosscher and D. Hedman, "Real-time collision avoidance algorithm for robotic manipulators," in *2009 IEEE International Conference on Technologies for Practical Robot Applications*. IEEE, 2009, pp. 113–121.

[30] W. Su, Y. Yuan, and M. Zhu, "A relationship between the average precision and the area under the roc curve," in *Proceedings of the 2015 International Conference on The Theory of Information Retrieval*, ser. ICTIR '15. New York, NY, USA: ACM, 2015, pp. 349–352. [Online]. Available: http://doi.acm.org/10.1145/2808194.2809481

applied sciences

Article

Human–Robot Interaction for Improving Fuselage Assembly Tasks: A Case Study

Elena Laudante, Alessandro Greco *, Mario Caterino and Marcello Fera

Department of Engineering, University of Campania Luigi Vanvitelli, via Roma, 29–81031 Aversa (CE), Italy; elena.laudante@unicampania.it (E.L.); mario.caterino@unicampania.it (M.C.); marcello.fera@unicampania.it (M.F.)

* Correspondence: alessandro.greco@unicampania.it; Tel.: +39-081-50-10-318

Received: 17 July 2020; Accepted: 17 August 2020; Published: 20 August 2020

Abstract: In current industrial systems, automation is a very important aspect for assessing manufacturing production performance related to working times, accuracy of operations and quality. In particular, the introduction of a robotic system in the working area should guarantee some improvements, such as risks reduction for human operators, better quality results and a speed increase for production processes. In this context, human action remains still necessary to carry out part of the subtasks, as in the case of composites assembly processes. This study aims at presenting a case study regarding the reorganization of the working activity carried out in workstation in which a composite fuselage panel is assembled in order to demonstrate, by means of simulation tool, that some of the advantages previously listed can be achieved also in aerospace industry. In particular, an entire working process for composite fuselage panel assembling will be simulated and analyzed in order to demonstrate and verify the applicability and effectiveness of human–robot interaction (HRI), focusing on working times and ergonomics and respecting the constraints imposed by standards ISO 10218 and ISO TS 15066. Results show the effectiveness of HRI both in terms of assembly performance, by reducing working times and ergonomics—for which the simulation provides a very low risk index.

Keywords: aerospace production; ergonomics; human–robot interaction; simulation

1. Introduction

In the new industrial era, ergonomics is crucial for occupational safety and productivity improvement in different manufacturing sectors such as the automotive and aerospace industry, which is one of the largest and most demanding production areas. Therefore, safety is a fundamental aspect that is sought through the use of improved tools in production processes, and the implementation of efficient and safe techniques to adapt people to work in order to optimize well-being and to increase productivity.

Focusing on the aerospace field, the design of appropriate workstations is essential to improve occupational health, safety and work efficiency [1]. Even if aerospace production is not as systematized as automotive production—with much longer cycle times—it is equally affected by ergonomic issues. On the contrary, in many working activities characterizing aerospace production lines, the biomechanical load is very high due to awkward postures, lifting heavy components, exerting high forces and repetitive actions. Even in the case of the aerospace industry, if workers are subject to these factors, the risk of injury and muscle fatigue is high [2].

Many studies show that interactions among humans, technologies, organizations and working environments are strictly influenced by ergonomics. Often, the main causes of quality deficiencies are associated with ergonomic issues in terms of environmental conditions, suitable design of technology and an inappropriate organization [3].

Therefore, ergonomics may become the driving force for the improvement of new quality processes and production strategies. In aerospace field, improving ergonomics allows reaching the aim of producing high quality aircraft through the study of human specifications for the suitable design of the living and working environment [4]. Tools, devices, machines, appliances and the environment all lead to the advancement of the safety levels, well-being and human performances, as suggested by Kroemer et al. [5].

In industry, humans represent the primary production resource, and their efficiency in performing working tasks represents the main factor of productivity, a primary factor of economic activity [6].

In the literature concerning aerospace applications, it is possible to find many studies on the analysis of ergonomic aspects such as the safety and comfort in the passenger cabin and passenger compartment. These studies are mainly focused on the assessment of key factors, such as head and legroom and the ease with which the stowage can be reached. However, from the production process point of view, rarely ergonomic factors have been analyzed during the assembly phases, applying ergonomics principles only in borderline situations and in limited space, a typical condition to which the operators are exposed, which increase the risk of musculoskeletal injuries [7].

In this sense, studies were conducted during the wing assembly phases which, as most aerospace components, require static and uncomfortable postures that increase the risk of physical illness and hinder the execution of tasks. Different solutions to optimize the assembly process were investigated [8,9], by changing the orientation and accessibility of the product through the introduction of a rotating device capable of keeping the entire wing in an open box condition and allowing the operator to assume ergonomic postures.

However, except in rare case, since ergonomics has never been adequately considered, the need to design new production lines, based on ergonomics principles, arises; in this case, simulation tools and virtual ergonomics are essential to design safe and high-performance workstations [10]. Indeed, in the recent years the industrial world is experiencing a massive implementation of digital technological systems. These could be useful for better verifying and validating the ergonomic factors in the design, production and maintenance processes and, in general, for testing the design solutions and the functionality of machines or robots. This allows detecting certain errors before the real production phases.

About ergonomics, simulation and digital twin (DT) allow considering human factors preventively, since the design phase. This is a fundamental aspect of the Industry 4.0 paradigm, which has the human-centered design as one of its main pillars.

In the literature, there are many studies focused on the use of virtual simulation for investigating the ergonomic issues in manufacturing production processes, especially for the automotive sector [11–15], even if, as demonstrated by Cimino et al. [16], in the current literature, DTs have many missing elements to be compliant to their description. The numeric approach provided by DT and simulation, gives the opportunity to simulate manual or automatized working tasks and, hence, to evaluate the performance indices and to identify critical issues in a virtual scenario, without any real experimental test.

A further potential contribution for reducing exposure to occupational risk and at the same time increasing production efficiency is certainly the introduction of robots into the production system.

The use of high-tech industrial robotics, now widespread in all manufacturing sectors, is finding its way into almost all phases of the production process, from automated and flexible assembly to component processing, from production control to final palletization in order to guarantee control, quality and flexibility. Obviously, the use of robots is also changing the human role, which in the era of Industry 4.0 is becoming smarter than before, leaving to robots and machines the hardest tasks [17].

In aerospace, this implementation is currently not comparable to other production fields. Assembly in aircraft production is among the least automated sectors of the industry for different reasons. These are large and complex systems that involve a very wide variety of activities to be carried out in the production phases, whose aerospace components require low production numbers, with processes that require hours of work for the single component.

The workspace is limited and with the presence of obstacles and technical barriers in compliance with the need to achieve high levels of quality and precision and to satisfy safety and reliability. In response to the relative difficulties in introducing robotics in the aerospace sector, research is moving towards the implementation of robotic instrumentation initially tested through artificial visions and virtual prototyping, offering new perspectives to aerospace production.

In different studies, the strong benefits that the use of robotics can bring within the aerospace process are being understood, as in the case of Tingelstad et al. [18]. They have shown how the use of industrial robots, associated with a high precision noncontact measurement system, allows automating some assembly and spot welding operations for aerospace components.

The application of the human-centered design approach and the introduction of robots that can interact with humans in the production system could represent a challenge for the aerospace industry which, as demonstrated by the lack of literature, is still linked to essentially manual and no repeatable production systems. In particular, the use of virtual simulation, being an open issue for aerospace applications, will allow technical data to be transformed into three-dimensional designs with a strong visual impact covering all phases of the design cycle.

Aim of this study, part of a Clean Sky Horizon 2020 research project, is to present a methodology that, by using simulation, enables users to evaluate advantages due to the introduction of a HRI in a completely manual work cell before the cell is physically realized. Results from a real case are presented. Case study is about the reorganization of the working activity carried out in a workstation in which a composite fuselage panel is assembled no more only by humans. In detail, robots will be introduced for carrying out several operations, sharing the same working space with the worker and respecting all the safety requirements. As already partially presented in [19], the introduction of HRI enables both a working times reduction and also an improvement of the workload for humans, as demonstrated in the following sections. By performing a simulation, the adopted solution was verified and the ergonomic index related to postures assumed by workers during manual tasks was evaluated by mean of OWAS (Ovako working posture analysis system) method.

The use of digital models and simulation represents a fundamental step for solving validation studies for the introduction of automatic processing systems instead of the traditional systems used for composite materials, which are very often manual and not repeatable.

The reminder of this study is organized as follows: Section 2 focused on the Human–Robot Interactions and its advantages for industrial applications. Moreover, a wide overview about the regulatory framework in robotics is provided. Section 2.1 describes the methodology herein used to assess benefits of HRI introduction. Section 3 describes the investigated case study regarding a real workstation in aerospace production line, that will be only described using words or misaligned data to preserve the confidentiality of the project results; in particular, a composite fuselage panel is assembled and riveted, with a detailed description about a numeric simulation and the data provided. Section 4 presents results analyses and discussion while Section 5 further concludes the study.

2. Human–Robot Interaction and Regulatory Frameworks

Recently, there has been a massive growth of the interest by industries about the possibility to introduce safe robots in their production lines in order to improve the production itself by letting robots share common space with humans. Humans and robots could potentially execute a variety of useful tasks under safety premises [20]. The study of robotic systems capable of perceiving the environment in a complex way and to interact with it is a recurring topic especially in the human–robot interaction field and represents the starting point for advanced research and technology transfer, considering interfaces and human–robot interaction one of the main research objects of the discipline of robotics.

Typically, HRI is often associated with the use of collaborative robots. However, an interesting differentiation has been proposed by Schmidtler et al. [21], which identifies three kinds of interaction: coexistence, cooperation and collaboration. Coexistence occurs when human and robot are in the same space at the same time. In cooperation, humans and robots share the same aim. However, by adding a physical contact (auditory or haptic), it is possible to talk about collaboration.

Other levels of interaction have been introduced by Shi et al. [22]: (i) low—when the human does not enter the working space of robotic system; (ii) medium—characterized by a de-energization of servo drives when human is close; (iii) high—when the robot can move near humans.

Bender et al. [23] even proposed five levels of interaction: cell—when the robot is in a cage; coexistence—when human and robot does not share the workspace not shared; synchronized—when only one between human and robot is present at a time; cooperation—when human and robot share the workspace, but they do not perform simultaneous tasks; collaboration—when human and robot work on the same product simultaneously.

As a still open issue, many other differentiations have been proposed in the literature—even if none of them is exhaustive [24]. Regardless, in the future, HRI will surely tend increasingly towards replicating human–human interactions.

The introduction of robots into a workspace to carry out assembly operations allows to achieve several benefits, especially regarding the quality of operations, task repeatability, reduction of working times and reduction of ergonomic risk. Table 1 describes the pros and the cons considering three modes of working in a workstation: only human, only robot and human and robot together (HRI).

Table 1. Pros and cons of human–robot interaction (HRI).

	Pros	Cons
Human	Perception of operations Decision making Working-process control	Working times Ergonomic issues Task repeatability not ensured Quality of operations Fatigue Working load Risk of injuries High full cost
Robot	Reduction of working times Quality of operations Task repeatability Not ergonomic issues Continuous working Scale economy	No perception of operations Low control of working process
Human–Robot Interaction	Reduction of working times Quality of operations Task repeatability Reduction of ergonomic issues Continuous working Decision making Perception of operations Working-process control	Continuous safety control

However, improved quality of life and increased levels of occupational safety are the basis for the massive introduction of flexible automation in current production processes. In the case of repetitive, monotonous and dangerous tasks, the implementation of robotic systems makes it possible to increase the quality and precision of work [25] as well as reduce production costs and the relationship between humans and robots that defines the morphology of increasingly flexible, sustainable, ergonomic, intelligent and smart factories [26]. Sensors, machines, workers and IT systems connected to each other along the value chain, give rise to countless technical and economic benefits for future manufacturing through the use of different technologies that fit into the different industrial phases, starting from product/process design, monitoring and control, production operations, services.

The factory of the future will be characterized by human–machine coexistence, cooperation and coordination where the latter adapts to human's times and ways and through which advantages such as production flexibility, high performance and competitiveness on the global market are generated. The autonomy of "evolved" robots derives from the ability to process information collected by sensors and to plan the sequence of actions to be taken.

Thanks to numerous studies on safety in HRI that are being conducted [27], it is plausible to argue that robots interacting with humans will not require perimeter security fences. The will replace human in performing repetitive or dangerous working tasks, increasing the efficiency of industrial plants and ensuring the workers' safety. Among these types of robots, currently Collaborative Robots are undoubtedly the most widespread in innovative industrial contexts, representing the avant-garde of robotics in the industry. However, as anticipated, there is concern about its impact on occupational health and safety management [28].

In the complexity of a HRI, the physical viewpoint is mainly focused on the risks of collisions occurring between the robot and its user [29].

Human–robot collaboration needs to deep-in safety aspects, comfort of use, safety perception and ergonomic guidelines. Technical specifications and standards, such as ISO TS/15066 [30], are taken into account, which provides guidance for the use of robots in collaborative operations based on safety requirements. ISO TS/15066 integrates the provisions and guidelines on the operation of collaborative industrial robots indicated in ISO 10218-1 [31] and ISO 10218-2 [32]. The current safety standards related to the discipline of robotics are actively updated in order to respond to any problems encountered in working environments.

ISO 12218 is divided into two parts: ISO 10218-1:2011 Robots and robot equipment—safety requirements for industrial robots; Part 1: Robots; ISO 10218-2: 2011 Robots and robot equipment—Safety requirements for industrial robots; Part 2: Robot systems and robot integration.

In the first part, a guidance for safety in design, protective measures and instructions about the use of industrial robots are introduced, describing the basic hazards and providing characteristics needed to eliminate or, at least, reduce the risks associated with them. The second part specifies the hazards arising from the integration of industrial robots into production lines and identifies the minimum safety requirements from undertaken by manufacturer, supplier and user to ensure a safe working environment.

Going into detail about the type of robots, the standard that concerns specific collaborative robots is ISO/TS 15066:2016, specifying the safety requirements for industrial collaborative robotic systems and the working environment. Designers of robotic systems must have full knowledge of current safety standards and must proceed according to the concept of awareness, fault tolerance and explicit communication, relying on the needs of research in the safety area [33]. This attention enables to move scientific progresses achieved in the field of HRI to an industrial level [34].

From ISO 10218 to ISO/TS 15066:2016

Currently, this specification is the most detailed document which gives guidelines about safety requirements in the field of collaborative industrial robot work cells and it is mainly focused on mechanical risk.

According to the specification, to ensure a safe collaboration among human workers and robot systems, mechanical risks must be minimized in order to avoid unexpected contacts in terms of gravity and/or probability. ISO/TS 15066 introduces four different methods for safe HRI: *Safety-rated monitored stop* which provides for the stop of robot motion when an operator enters the collaborative workspace. Then, only when the operator leaves the zone, the robotic task can automatically resume. *Hand guiding* method takes into account the operator that is able to fully control the robot motion by direct physical interaction. Hence, the operator can guide manually the robotic task, simply by moving the robotic arm by mean of a tool located at or near the end-effector. The operator can enter in the collaborative working zone only once the robot has achieved a safety-rated monitored stop condition. For the *speed and separation monitoring* method, the speed and distance among human and robots must be continuously monitored by means of a control system. Thus, the robot is able to dynamically maintain a correct combination of speed and distance in order to avoid the possibility of any hazardous motion which may be the cause for unexpected contacts.

The last one is *power and force limiting* in which the biomechanical risk of unexpected human–robot contacts is sufficiently reduced either through inherently safe means in the robot or through a safety-related control system [35].

Since the case study here-in presented falls within the speed and separation monitoring context, some additional information is provided below.

In particular, the protective separation distance (S_p), defined in Equation (1), is a function f(.) of:

- the robot-system reaction time (T_r): the time required for detecting the operator, elaborating the signal and activating the stop;
- the stopping time of the robot (T_s): the time among the start of stop signal and the instant in which the robot halts;
- the speed of the human worker in direction of the robot's moving tool (V_h);
- the speed of robot in course of stopping (V_s): the time between the stop signal activation and the real stopping instant;
- the intrusion distance (C): the distance that a part of the body can intrude into the sensing area of the robot before it is detected;
- the position uncertainty of the operator in the shared workspace (Z_d) and the position uncertainty of the robot system (Z_r):

$$S_p = \mathrm{f}(T_r, T_s, V_h, V_s, C, Z_d, Z_r) \tag{1}$$

Thus, while the ISO 10218 describes in general terms the 4 types of collaborative operations, ISO 15066 adds new information to improve the design criteria of a collaborative system. Although not normative, the technical specification accurately describes the state of the art of safety of collaborative actions and provides specific guidance for risk assessment. ISO 10218, which focuses on industrial robots in general, leaves room for ISO/TS 15066, which focuses on collaborative robots and the definition of requirements to ensure the safety of production operators interacting with robotic systems. A further step forward is the presence of data on injury levels through the identification of pain thresholds in the different parts of the body in contact with the robot and the related force and pressure levels that lead to the improvement of the design of the systems avoiding the exceeding of these thresholds in case of human–robot contact.

2.1. Methodology

This section proposes the methodology herein used to assess benefits due to the introduction of robots in work cells in which the current job is completely manual. The procedure is generally applicable, and it is represented in Figure 1.

The procedure consists of three main steps, each one composed by others sub-steps.

The first step concerns the evaluation of the current job (blue box in Figure 1), which is manually performed. In particular, the procedure starts by evaluating the methods used to carry out manual tasks and the related working times. This part of the procedure is assessed by an expert analyst by means of traditional techniques used to estimate working times. This first evaluation gives the possibility to identify the parts of the working cycle in which robots can replace humans, preferring high precision tasks.

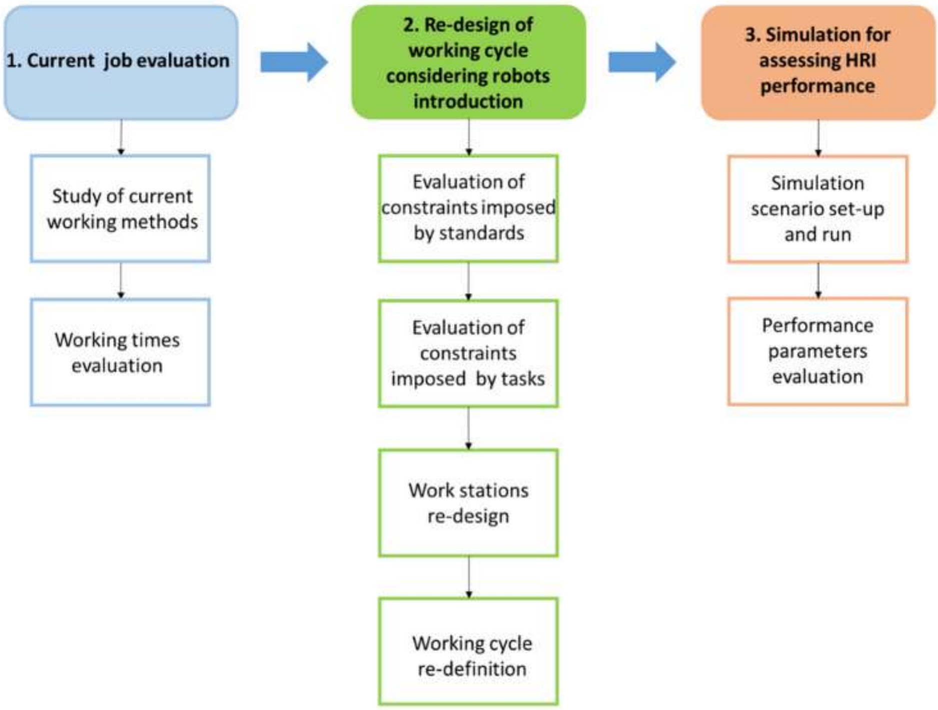

Figure 1. Methodological procedure for HRI definition.

The second step of the procedure (green box in Figure 1) aims to redesign the workstation layout and redefine the working cycle, by considering the introduction of robots. In detail, robots are introduced in order to improve the working cycle by reducing working times and increasing the quality of the performed tasks, thus minimizing the probability to produce defective components. In order to achieve these results, a redesign of the working cell as well as a redefinition of the working tasks may be necessary to implement the HRI. Hence, this step requires to take into account the definition of constraints imposed by both working tasks and by Standards regulating the HRI implementation, as described in the previous Section 2. Thus, the design of the new working cell and the assignment of tasks to human and robots can be achieved only once some parameters (T_r, T_s, V_s, C, ...) and the kind of robots have been defined.

The last step of the procedure (orange box in Figure 1) is about the assessment of the new work cell and working cycle performance by means of simulation. In order to perform the simulation, the real working environment must be reproduced in a virtual scenario; this implies the implementation of:

1. parts belonging to the real working station (by means, for instance, of CAD files), such as tools, handling lines, work benches, etc.;
2. digital human models (DHMs) which reproduce the anthropometric characteristics of the real workers;
3. digital robots, which reproduce the models of robots that will be used, including the kinematics.

Once the simulation environment has been defined, it is possible to assess the desired performance parameters (such as working times or ergonomics) and to put in evidence eventual critical issues.

3. Case Study

This section focuses on the investigation about HRI application for improving working times and ergonomics of a working process for composite fuselage panel assembly.

The case study derives from a European Clean Sky Horizon 2020 Project, named "Lean robotized AssemBly and cOntrol of composite aeRostructures (LABOR)" that is coordinated by Loccioni and with Leonardo SpA as topic manager. The goal of the project is to redesign a workstation in order to implement a HRI for a working cell currently characterized by manual working tasks. In detail, the new cell provides for the sharing of the same workspace by human and robots. As proposed in the procedure represented in Figure 1, an investigation was conducted numerically, by means of simulation.

After assessing the method and times of the current manual workstation (Step 1 of the procedure in Figure 1), the new solution implementing HRI, was designed by all project partners who have shared their knowledge in order to achieve the best possible solution for new work cell creation (Step 2 of the procedure in Figure 1). Then, the DT of the new HRI cell was created and simulation was used to evaluate its feasibility, considering working times and ergonomics (Step 3 of the procedure in Figure 1).

The working cycle in the HRI case was redesigned on the base of the manual one, whose characteristics were provided by the project leader company. In order to create the new working cycle for HRI, constraints imposed by ISO 10218 [31,32] and ISO/TS 15066 [30] and the sequence of operations were considered.

It is worth to note that, in the new configuration, the macro assembling operations remain the same, even if reorganized in order to ensure the human–robot coexistence. Because of the confidentiality, sharing of all the assembly cycle subtasks is not allowed; so, in Table 2, only the macro tasks of the assembly cycle, named Before HRI and After HRI, are described.

Table 2. General aircraft panel assembling operations before and after HRI.

	Before HRI		After HRI	
Operation Code	**Human**	**Robot**	**Human**	**Robot**
OP10	Assembly of shear ties, frames and aluminum stringers on CFRP skin	NA	Assembly of shear ties, frames and aluminum stringers on CFRP skin	NA
OP20	Drilling the entire fuselage panel	NA	NA	Drilling the entire fuselage panel
OP30	Countersinking the entire fuselage panel	NA	NA	Countersinking the entire fuselage panel
OP40	Hole inspection	NA	NA	Hole inspection
OP50	Disassembling of aluminum stringers	NA	Disassembling of aluminum stringers	NA
OP60	Cleaning of aluminum stringers	NA	Cleaning of aluminum stringers	NA
OP70	Deburring of aluminum stringers	NA	Deburring of aluminum stringers	NA
OP80	Application of sealant	NA	Application of sealant	NA
OP90	Reassembling of stringers on skin	NA	Reassembling of stringers on skin	NA
OP100	Riveting the entire fuselage panel	NA	NA	Riveting the entire fuselage panel

NA–Not Available.

As specified in the previous Section 2.1, robots are introduced to improve the quality of performed operations. Hence, as shown in Table 2, drilling, countersinking and riveting operations are performed on a carbon-fiber-reinforced polymer (CFRP) panel by robots in HRI configuration due to the high precision and quality needed, especially for drilling operations, whose tolerances are very strict. In fact, it has been demonstrated that robots working in specific distance areas (namely best working area) are able to respect very strict tolerances [36].

The robots selected by the company are the FANUC M 20iA. To satisfy the requirements of the standard ISO/TS 15066, all the parameters of Equation (1) were considered, assuming V_h and V_s as constant, even though the speed modulation system proposed in [37] is able to optimize these values, relying on a risk analysis performed online through a fuzzy inference system.

Figure 2b shows an example of the end effector normalized speed trend as function of the distance between the robot and the human hands (Figure 2a) when these last are detected according to the multimodal system proposed in [38]. It is worth to note that the robot has not a 1 or 0 condition of speed, but its speed is modulated according to the distance from the worker and even the minimum separation distance S is adjusted in real time again on the basis of the actual robot and human relative positions and velocities (see [38] for more details).

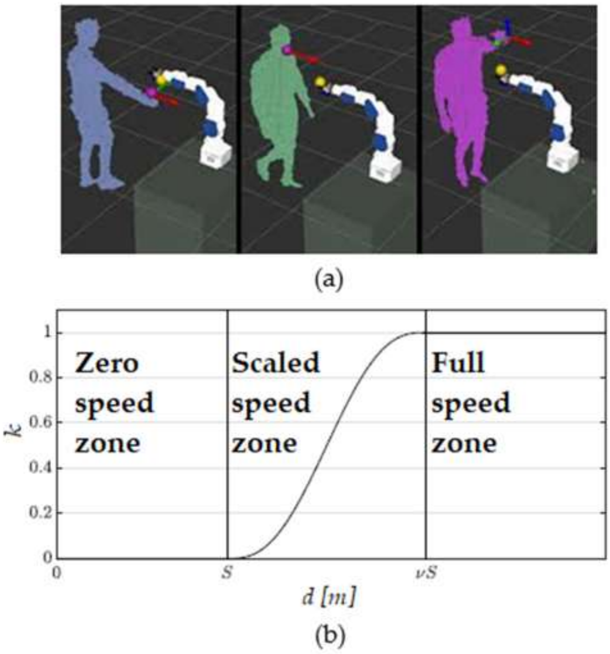

Figure 2. (**a**) Human-hand detection by robot sensors and cameras; (**b**) trend of normalized robot speed in proximity of human (plot courtesy of [37]).

As suggested by the Step 2 of the procedure in Figure 1, also the constraints due to operations precedencies were considered for each working zone and for the whole fuselage panel in order to create a feasible working cycle. The typical sequence performed in assembling a fuselage panel is represented in Figure 3, where operations code reported in Table 2 are represented.

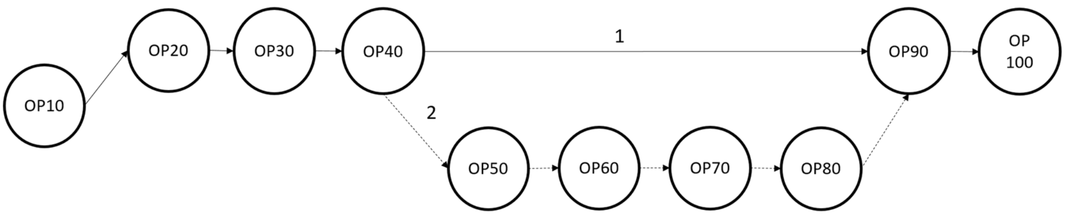

Figure 3. Precedence graph for operations of Table 2.

OP10 is a preliminary operation, not considered for the analyses in this study. In some areas, the panel is reinforced with aluminum elements (see Figure 4) and the human carries out working tasks only in these areas. For this reason, in Figure 3, two paths are represented:

1. Path 1 is followed when there are not aluminum elements in the working zone and human operations are not required;
2. Path 2 is followed when aluminum elements, such as stringers or frames, are in the working zone and also human operations are required.

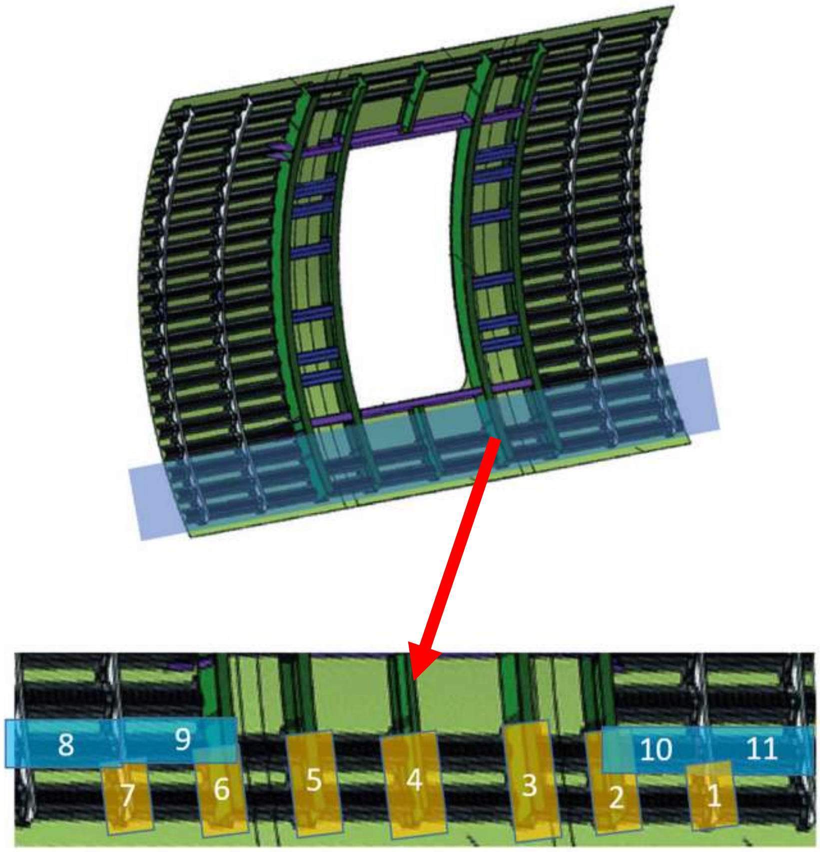

Figure 4. Aircraft panel considered in the case study (CAD drawing courtesy of [39]).

The entire working cycle for HRI was defined by respecting both constraints due to standards and due to operations precedence and it was simulated in order to evaluate the working times for panel assembling and ergonomics issues.

Moreover, according to Step 3 of the procedure in Figure 1, the 3D CAD models representing the new workstation were implemented for simulation in Tecnomatix Process Simulate by Siemens® software environment.

Figure 4 represents a generic fuselage panel, for privacy reasons. In figure, a zoom of one of the working sections is represented at the bottom. Here, different working zones are visible, namely yellow and blue to indicate, respectively, the zones where only robots' operations are needed (path 1 of Figure 3), and zones where also human operations must be performed (path 2 of Figure 3). This approach has been used for each section of the panel: robots work in small areas in order to respect tolerances.

Figure 5 shows a schematic configuration of the workstation in which the human and the robot share the same working area. For privacy reason, it is not represented the real station, which is provided with a scaffolding, which allows human to reach far working zones, and one of the two robots moves on a horizontal support. The panel can rotate as well as shown in Figure 5.

Concerning the worker, a DHM, representing the male P50 of Italian anthropometric database [40], was set for carrying out manual operations.

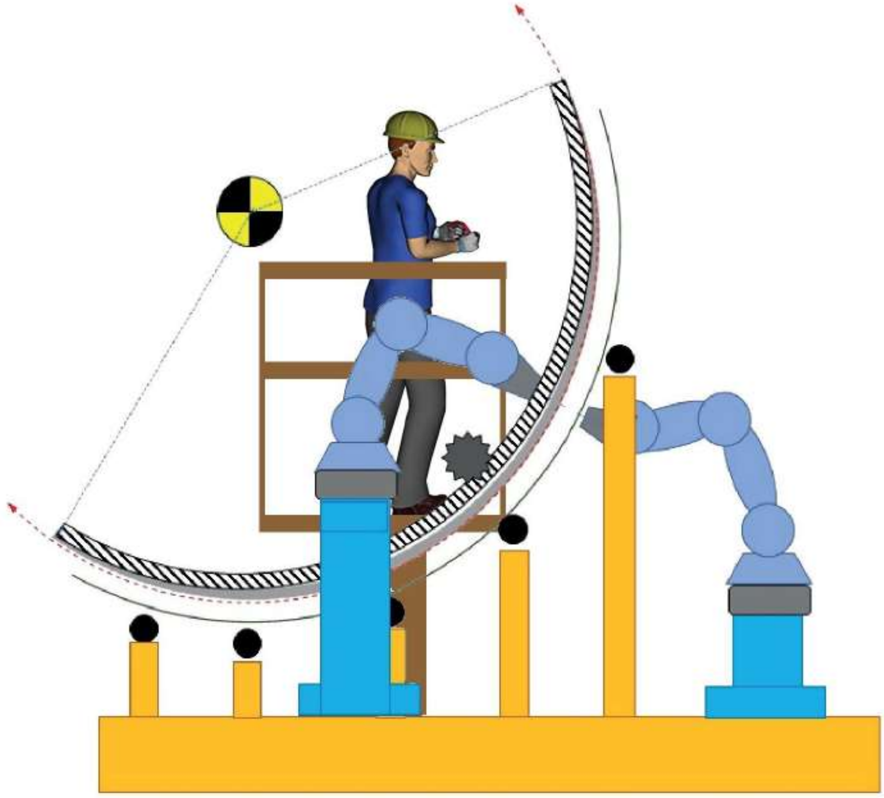

Figure 5. Workstation schematic layout.

4. Results and Discussion

According to Step 1 of the procedure in Figure 1, the working times of human, in HRI configuration, were estimated relying on the current manual configuration of the workstation. For privacy reasons, it is not possible to report the operations' times, but it can be useful to know that the assembling operations of the whole fuselage composite panel require about 3 working shifts. The analysis proposed in this study aims to evaluate if the completion time would decrease in HRI configuration. Moreover, a scale factor (SF) will be used in order to show the difference between the two configurations, as described in Table 2.

In detail, without loss of generality, the working time values (T) reported in this section, is equivalent to the scaled real working time values (RT), according to the following Equation (2):

$$T = RT \times SF \quad (2)$$

By applying Equation (2), the working time to assemble the whole panel (T_a) is 15 hours.

For estimating the working times in HRI configuration (Step 2 of procedure in Figure 1), about humans, several studies assess that in presence of robots, which may have predictable or unpredictable motions [41], humans are negatively influenced by the presence a robot [42,43], so the human working times for each operation have increased in a range between 10–20% of the estimated time, according to the type of operation. About the robots, KUKA estimated a mean reduction of working times, when a task is performed by a robot, of about 30% with respect to humans' times [44].

Consequently, for the tasks performed by robot (namely drilling, countersinking, inspection and riveting), the working times (T_R) values are assumed to be reduced of 30% with respect to the previously estimated working time, according to Equation (3).

$$T_R = RT \times SF \times 0.70 \quad (3)$$

Other robots' operations, such as the referencing of the working zone, the moving times, the end-effector tool changing times, etc., depend on the robots' characteristics. On each digital robot the real robot controller was implemented to define the minimum and maximum linear speeds, the joints' rotation speed and other important parameters.

Two types of cycle were implemented to simulate two different assembling scenarios. The first one cannot be considered as HRI, since the human and robots never work at the same time: when human is performing a task, the robot is passive and vice versa. In the second case, human and robots share the same working zone by respecting the constraints imposed by ISO-TS 15066 and their operations can be performed simultaneously, as shown in Table 3, representing part of the working cycle where same colors identify operations performed simultaneously.

Table 3. Part of the working cycle in HRI configuration.

<table>
<tr><th colspan="3">HUMAN</th><th colspan="3">ROBOT</th></tr>
<tr><th>Operation Description</th><th>Estimated Time—T (s)</th><th>Working Area</th><th>Operation Description</th><th>Estimated Time—T (s)</th><th>Working Area</th></tr>
<tr><td>Lifter Positioning</td><td>38</td><td>Slot 1, Area 11</td><td>Referencing working area</td><td>38</td><td>Slot 5, Area 3</td></tr>
<tr><td>Pop Rivets Removal</td><td>31</td><td>Slot 1, Area 11</td><td rowspan="3">Execute the entire cycle of drilling, countersinking, hole inspection, change tool, fastener installation and control</td><td rowspan="3"></td><td rowspan="3">Slot 5, Area 3</td></tr>
<tr><td>Stringer Disassembling</td><td>51</td><td>Slot 1, Area 11</td></tr>
<tr><td>Deburring of Holes</td><td>247</td><td>Slot 1, Area 11</td></tr>
<tr><td>Sealant Application</td><td>201</td><td>Slot 1, Area 11</td><td>Referencing working area</td><td>38</td><td>Slot 5, Area 2</td></tr>
<tr><td>Stringer Reassembling</td><td>51</td><td>Slot 1, Area 11</td><td rowspan="5">Execute the entire cycle of drilling, countersinking, hole inspection, change tool, fastener installation and control</td><td rowspan="5"></td><td rowspan="5">Slot 5, Area 2</td></tr>
<tr><td>Clecos Application</td><td>76</td><td>Slot 1, Area 11</td></tr>
<tr><td>Lifter Positioning</td><td>16</td><td>Slot 2, Area 12</td></tr>
<tr><td>Pop rivets Removal</td><td>15</td><td>Slot 2, Area 12</td></tr>
<tr><td>Stringer Disassembling</td><td>25</td><td>Slot 2, Area 12</td></tr>
</table>

Simulations were performed considering both simultaneous and separated working tasks.

The working times of Table 3 consider also the time required for human's micro-movement, such as walking, raise an arm, grasp an object, etc., which are implemented in Tecnomatix Process Simulate, based on MTM (method and time measurement) tables.

Results provided by the simulations are shown in Table 4 where there is a comparison between the different configurations: only manual, human and robot in sequential performing and HRI.

Table 4. Simulation results.

	Only Manual	Human–Robot	HRI
Time to Assemble (h)	15	8.78	7.86
Reduced Time (h)	0	6.22	7.14
% of Reduced Time	0	41.5%	47.6%

The implementation of robots in the workstation drastically reduces the working time for assembling the whole panel. This time is furtherly reduced in HRI configuration, where the difference with the manual configuration is almost the 50%.

Moreover, other details about HRI configuration are described in Table 5; both human-worker and robots have downtimes (namely passive time) due to constraints imposed by ISO-TS 15066 and mechanical constraints.

Table 5. Working time detail for human and robot in HRI configuration.

	Active Time (h)	Passive Time (h)	Interaction Time (h)	Passive Time (%)
Human	2.23	5.61	1.04	71.4
Robots	6.67	1.19	1.04	15.1

Some considerations may be done from results reported in Tables 4 and 5:

- Implementation of robots reduces the total working time for assembling the panel;
- Interaction time, i.e., the time during which human and robots work simultaneously, sharing the same working area, is about 13% of the total time. This can be furtherly increased by working-cycle optimization;
- Passive time for human is very high, suggesting that one worker may follow the assembling of more than one panel during the whole working shift;
- Passive times for robots is due to the separation distance imposed by ISO-TS 15066. They depend on the presence of human in proximity of the robot, according to ISO-TS 15066: These times could be reduced by working-cycle optimization.

Ergonomics Evaluation

The second analysis was carried out to assess ergonomic performance in HRI configuration.

Generally, ergonomic analysis in manufacturing production processes needs to be performed for four main factors, cause of injury due to biomechanical overload: (*i*) working postures, (*ii*) manual material handling (MMH), (*iii*) exerted forces and (*iv*) repetitive actions. In this case, only the assumed working postures contribute to biomechanical load, since there are no repetitive actions during the work shift, as well as no objects weighting more than three kilograms to handle or lift. About exerted forces, robots perform all drilling and countersinking tasks, which are the only ones for which forces are required. Thus, also exerted forces may be neglected in ergonomic analysis.

Hence, in order to analyze working postures, Ovako Working posture Analyzing Systems (OWAS) method [45] was used. OWAS method provides risk assessment for whole body by analyzing postures assumed by human workers. It assumes four risk classes, identified by four different weights, namely 1, 2, 3, 4.

In particular, weights for each risk class can be defined as follows:

- Risk class 1: no risk;
- Risk class 2: low risk;
- Risk class 3: medium risk;
- Risk class 4: high risk.

The final output of the method is the OWAS index, represented in the following Equation (4):

$$\mathrm{I} = [(\mathrm{a} \times 1) + (\mathrm{b} \times 2) + (\mathrm{c} \times 3) + (\mathrm{d} \times 4)] \times 100 \tag{4}$$

where a, b, c, d are the observation frequencies for each risk class. Observation frequencies may be calculated as the number of observations for each class (N_k) divided the total number of observations (N):

$$k = \frac{N_k}{N} \times 100 \; with \; k = a \ldots d \tag{5}$$

The final score is between 100 and 400. Table 6 represents the worker risk exposure based on the OWAS index and suggests possible corrective actions for high risk cases.

Table 6. OWAS index—risk areas.

OWAS Risk Index		
Value	**Risk Exposure**	**Consequences**
100	No risk	No consequences
101–200	Low risk	If possible, improve structural factors or take other organizational measures
201–300	Medium risk	Improve structural factors or take other organizational measures, rapidly
301–400	High risk	Immediate action need to change the operating methods, the equipment used or the work positions of the workers

Typically, the OWAS procedure also considers the handled weight higher that 10 kg. Since all the tools handled by human have weight less than 10 kg, the mass does not contribute to the OWAS index.

Another important factor affecting the accuracy of OWAS analysis is the sampling time of DHM movement. In fact, a great advantage of the analysis performed by using a digital reproduction of the real workstation is the possibility to vary the sampling time in order to achieve a good tradeoff between quality of the analysis and computational time. In particular, by decreasing the sampling time, more positions are acquired and analyzed, but the processing time increases and vice versa. In this study, a good compromise was achieved by fixing sampling time at 0.05 seconds (20 Hz frequency). The processing time, considering only human active times, was of about eight hours (already scaled by SF).

Taking into account SF, Table 7 shows the number of acquisitions falling in each action category and the observations frequency.

Table 7. Simulation results—OWAS coefficients.

Action Category	# of Observations		Observations Frequencies	% Value
1	114,983		a	93.885%
2	4840		b	3.951%
3	2649		c	2.163%
4	0		d	0.000%
	122,472	**Total**		100%

OWAS index can be calculated applying Equation (4):

$$I = [(0.93885 \times 1) + (0.03951 \times 2) + (0.02163 \times 3) + (0 \times 4)] \times 100 = 108.278 \quad (6)$$

The value of OWAS index falls within the low risk area; hence, there is no need for immediate corrective actions, but if possible, some organizational measures may be taken to improve the workstation. Concerning simulation, an important data are that only 7489 observations belong to action category 2, 3 or 4, corresponding to about six minutes of the human working cycle, highlighting the fact that occurring of musculo–skeletal disorders is very unlikely for this station.

5. Conclusions

In this study, the potential benefits of HRI was investigated for a real aerospace application. In particular, a methodology for redesigning a workstation was introduced and a real case study, in which a composite fuselage panel is assembled by human and robots, was proposed. The safety requirements and constraints imposed by standard ISO 10218 and ISO/TS 15066 were considered. In order to verify the feasibility of the approach, a simulation was carried out to evaluate the performance of the workstation in terms of both working times and ergonomics.

The results show a significant improvement of assembling performances in HRI configuration: in fact, the total assembling time is reduced of 47.6% with respect to the same activity manually performed. Concerning ergonomics, the OWAS index was evaluated and the result demonstrate that HRI allows the human working in extreme safety conditions, in terms of risk of work-related injuries. Unfortunately, it has not been possible to compare the obtained results with those of the OWAS index in the case of manual processing. However, it is presumable that, in this last case, the values are higher, considering the difficulty in reaching the working areas and the application of forces, together with the handling of additional loads, especially in performing drilling operations.

Numeric results validation, by means of comparison with experimental results, is not possible since the physical workstation is still not available. However—as already previously described—the literature demonstrated that numeric models for simulating manual operations provide results in agreement with those ones provided by experimental tests [11–15].

Future developments may be focused on the optimization of the sequence of tasks of the working cycle in order to assess the maximum benefits which can be obtained by employing the HRI solution. Computational time of the simulation can also be optimized by finding a tradeoff between the number of acquisition needed and the quality of the ergonomic assessment.

Author Contributions: Conceptualization, A.G., M.C., E.L., M.F.; methodology, A.G., M.C., M.F.; software, A.G., M.C.; formal analysis, A.G., M.C., E.L., M.F.; data curation, A.G, M.C.; writing—original draft preparation, A.G., M.C., E.L.; writing—review and editing A.G., M.C., E.L., M.F.; visualization, A.G., M.C., E.L.; supervision, M.F.; project administration, M.F.; All authors have read and agreed to the published version of the manuscript.

Funding: This work was supported by the European Commission under the H2020 Framework Clean Sky JTI–project LABOR, ID no. 785419, topic manager: Leonardo SpA.

Conflicts of Interest: No conflict of interest to declare.

References

1. Burgess-Limerick, R.; Steiner, L.J.; Torma-Krajewsky, J. *Ergonomics Processes: Implementation Guide and Tools for the Mining Industry*; US Department of Health and Human Services: Washington, DC, USA; Centers for Disease Control and Prevention: Atlanta, GA, USA; National Institute for Occupational Safety and Health: Washington, DC, USA; DHHS (NIOSH): Pittsburg, PA, USA, 2009.
2. Seri Rahayu, K.; Norhidayah, H.; Shahrizan, O.M. A Study on Muscle Fatigue Associated with Awkward Posture among Workers in Aerospace Industry. *Adv. Eng. Forum* **2013**, *10*, 287–292. [CrossRef]
3. Eklund, J.A. Ergonomics and Quality Management-Humans in Interaction with Technology, Work Environment and Organization. *Int. J. Occup. Saf. Ergo.* **1999**, *5*, 143–160. [CrossRef]
4. Getty, R.L.; Getty, J.M. Ergonomics Oriented to Processes Becomes a Tool for Continuous Improvement. *Int. J. Occup. Saf. Ergo.* **1999**, *5*, 161–194. [CrossRef] [PubMed]
5. Kroemer, K.H.E.; Kroemer, H.J.; Kroemer-Elbert, K.E. *Engineering Physiology: Bases of Human Factors/Ergonomic*; John Wiley and Sons: New York, NY, USA, 1994.
6. Lehto, M.R.; Landry, S.J. *Introduction to Human Factors and Ergonomics for Engineer*; CRC Press Taylor & Francis Group: New York, NY, USA, 2013.
7. Veasey, D.A.; Craft McCormick, L.; Hilyer, B.M.; Oldfield, K.W.; Hansen, S.; Krayer, T.H. *Confined Space Entry and Emergency Response*; Wiley: Hoboken, NJ, USA, 2005.
8. Fletcher, S.R.; Johnson, T.L. Investigating the impact of product orientation on muscoloskeletal risk in aerospace manufacturing. In *Contemporary Ergonomics and Human Factors 2014, Proceedings of the International Conference on Ergonomics & Human Factors 2014, Southampton, UK, 7–10 April 2014*; CRC Press: Boca Raton, FL, USA, 2014; pp. 85–92.
9. Judt, D.M.; Lowson, C.; Lockett, H. Experimental investigation into aircraft system manual assembly performance under varying structural component orientations. *Proc. IMechE Part B J. Eng. Manuf.* **2020**, *234*, 840–855. [CrossRef]
10. Beub, F.; Sender, J.; Flugge, W. Ergonomics Simulation in Aircraft Manufacturing—Methods and Potentials. *Proc. CIRP* **2019**, *81*, 742–746.
11. Alkan, B.; Vera, D.; Ahmad, M.; Ahmad, B.; Harrison, R. A lightweight approach for human factor assessment in virtual assembly designs: An evaluation model for postural risk and metabolic workload. *Proc. CIRP* **2016**, *44*, 26–31. [CrossRef]

12. Glaeser, D.; Fritzsche, L.; Bauer, S.; Sylaja, V.J. Ergonomic assessment for DHM simulation facilitated by sensor data. *Proc. CIRP* **2016**, *41*, 140–147. [CrossRef]
13. Lawson, G.; Salanistri, D.; Waterfield, B. Future directions for the development of virtual reality within an automotive manufacturer. *Appl. Ergon.* **2016**, *53*, 323–330. [CrossRef]
14. Caputo, F.; Greco, A.; Fera, M.; Macchiaroli, R. Workplace design ergonomic validation based on multiple human factors assessment methods and simulation. *Prod. Manuf. Res.* **2019**, *7*, 195–222. [CrossRef]
15. Caputo, F.; Greco, A.; Fera, M.; Macchiaroli, R. Digital twins to enhance the integration of ergonomics in the workplace design. *Int. J. Ind. Ergon.* **2019**, *71*, 20–31. [CrossRef]
16. Cimino, C.; Negri, E.; Fumagalli, L. Review of digital twin applications in manufacturing. *Comput. Ind.* **2019**, *113*, 103130. [CrossRef]
17. Evjemo, L.D.; Gjerstad, T.; Grøtli, E.I.; Sziebig, G. Trends in Smart Manufacturing: Role of Humans and Industrial Robots in Smart Factories. *Curr. Robot. Rep.* **2020**, *1*, 35–41. [CrossRef]
18. Tingelstad, L.; Capellan, A.; Thomessen, T.; Lien, T.K. Multi-Robot Assembly of High-Performance Aerospace Components. *IFAC Proc. Vol.* **2012**, *45*, 670–675. [CrossRef]
19. Greco, A.; Caputo, F.; Caterino, M.; D'Ambra, S.; Fera, M.; Laudante, E. Composite parts assembly operational improvements. *Macromol. Symp.* **2020**, *389*, 1900098. [CrossRef]
20. Hägele, M.; Nilsson, K.; Pires, J. Industrial Robotics. In *Handbook of Robotics*; Springer: Berlin, Heidelberg, Germany, 2008; pp. 963–986.
21. Schmidtler, J.; Knott, V.; Holzel, C.; Bengler, K. Human Centered Assistance Applications for the working environment of the future. *Occup. Ergon.* **2015**, *12*, 83–95. [CrossRef]
22. Shi, J.; Jimmerson, G.; Pearson, T.; Menassa, R. Levels of human and robot collaboration for automotive manufacturing. In Proceedings of the Workshop on Performance Metrics for Intelligent Systems, 20 March 2012; Volume 12, pp. 95–100.
23. Bender, M.; Braun, M.; Rally, P.; Scholtz, O. Lightweight robots in manual assembly—Best to start simply. In *Examining Companies' Initial Experiences with Lightweight Robots. Report*; Fraunhofer Institute for Industrial Engineering IAO: Stuttgard, Germany, 2016.
24. Aaltonen, I.; Salmi, T.; Marstio, I. Refining levels of collaboration to support the design and evaluation of human-robot interaction in the manufacturing industry. *Proc. CIRP* **2018**, *72*, 93–98. [CrossRef]
25. Matúšová, M.; Bučányová, M.; Hrušková, E. The future of industry with collaborative robots. *Matec Web Conf.* **2019**, *299*, 02008.
26. Magone, M.; Mazali, T. *Industria 4.0—Uomini e Macchine Nella Fabbrica Digitale*; Guerini e Associati: Milan, Italy, 2016; pp. 57–58.
27. Zacharaki, A.; Kostavelis, I.; Gasteratos, A.; Dokas, I. Safety bounds in human robot interaction: A survey. *Saf. Sci* **2020**, *127*, 104667. [CrossRef]
28. Teixeira, J.V.S.; Reis, A.M.; Mendes, F.B.; Vergara, L.G.L. Collaborative robots and ergonomics. *Occup. Environ. Saf. Health* **2019**, *202*, 791–796.
29. De Santis, A.; Siciliano, B.; De Luca, A.; Bicchi, A. Atlas of physical human-robot interaction. *Mech. Mach. Theory* **2008**, *43*, 253–270. [CrossRef]
30. ISO/TS 15066. *Robots and Robotic Devices: Collaborative Robots*; International Organization for Standardization: Geneva, Switzerland, 2016.
31. ISO 10218-1. *Robots and Robotic Devices—Safety Requirements for Industrial Robots—Part 1: Robots*; International Organization for Standardization: Geneva, Switzerland, 2011.
32. ISO 10218-2. *Robots and Robotic Devices—Safety Requirements for Industrial Robots—Part 1: Robot Systems and Integration*; International Organization for Standardization: Geneva, Switzerland, 2011.
33. Matthias, B.; Kock, S.; Jerregard, H.; Kllman, M.; Lundberg, I. Safety of collaborative industrial robots: Certification possibilities for a collaborative assembly robot concept. In *Assembly and Manufacturing (ISAM), IEEE International Symposium*; IEEE: Piscataway, NJ, USA, 2011; pp. 1–6.
34. Rosenstrauch, M.J.; Krüger, J. Safe human-robot-collaboration-introduction and experiment using ISO/TS 15066. In Proceedings of the 3rd International Conference on Control, Automation and Robotics (ICCAR), Nagoya, Japan, 22–24 April 2017; pp. 740–744.
35. Gualtieri, L.; Palomba, I.; Wehrle, E.J.; Vidoni, R. The Opportunities and Challenges of SME Manufacturing Automation: Safety and Ergonomics in Human-Robot Collaboration (HRC). *Ind. 4.0 SMEs* **2020**, 105–144.

36. Zhu, W.; Mei, B.; Yan, G.; Ke, Y. Measurement error analysis and accuracy enhancement of 2D vision system for robotic drilling. *Robot. Comput. Integr. Manuf.* **2014**, *30*, 160–171. [CrossRef]
37. Campomaggiore, A.; Costanzo, M.; Lettera, G.; Natale, C. *A Fuzzy Inference Approach to Control Robot Speed in Human-robot Shared Workspaces, Proceedings of the 16th International Conference on Informatics in Control, Automation and Robotics—ICINCO, INSTICC, Prague, Czech Republic, 29–31 July 2019*; SciTePress: Prague, Czech Republic, 2019; Volume 2, pp. 78–87.
38. Costanzo, M.; De Maria, G.; Lettera, G.; Natale, C.M.; Perrone, D. A Multimodal Perception System for Detection of Human Operators in Robotic Work Cells. In Proceedings of the 2019 IEEE International Conference on Systems, Man and Cybernetics (SMC), Bari, Italy, 6–9 October 2019; pp. 692–699.
39. Daniel, S.; Andreas, K.; Robert, K.; Peter, W.; Stefan, L.; Stefan, S.; Friedrich, V.D.; Juergen, T.; Christoph, B.; Ben, N. *Development of a Door Surround Structure with Integrated Structural Health Monitoring System In Smart Intelligent Aircraft Structures (SARISTU)*; Springer International Publishing: Cham, Switzerland, 2016; pp. 935–945.
40. Masali, M. *L'Italia si Misura. Vademecum Antropometrico Per il Design e L'ergonomia. Vent'anni di Ricerche (1990–2010)*; Aracne Editore: Rome, Italy, 2015.
41. Oyekan, J.O.; Hutabarat, W.; Tiwari, A.; Grech, R.; Aung, M.H.; Mariani, M.P.; Lopez-Davalos, L.; Ricaud, T.; Singh, S.; Dupuis, C. The effectiveness of virtual environments in developing collaborative strategies between industrial robots and humans. *Robot. Comput. Integr. Manuf.* **2019**, *55*, 41–54. [CrossRef]
42. Bortot, D.; Ding, H.; Antonopolous, A.; Bengler, K. Human motion behavior while interacting with an industrial robot. *J. Prev. Assess. Rehabil.* **2012**, *41* (Suppl. 1), 1699–1707. [CrossRef]
43. Bortot, D.F. Ergonomic Human-Robot Coexistence in the Branch of Production. Ph.D. Thesis, Technische Universität München, Munich, Germany, 2014.
44. Till, R.; Peter, M. Making the Right Decisions at the Right Time. 2017. Available online: https://www.kuka.com/-/media/kuka-corporate/documents/ir/reports-and-presentations/en/annual-report/kuka-annual-report-2016.pdf?rev=c976cc2263ef434682a6dbe81fd3e25f&hash=CF6BBC70885A83F5D4CF9EADCEBEEB81 (accessed on 10 July 2020).
45. Kharu, O.; Kansi, P.; Kuorinka, I. Correcting working postures in industry: A practical method for analysis. *Appl. Ergon.* **1977**, *8*, 199–201.

IOP Conference Series: Materials Science and Engineering

PAPER • OPEN ACCESS

Robotized assembly and inspection of composite fuselage panels: the LABOR project approach

To cite this article: Mario Caterino *et al* 2021 *IOP Conf. Ser.: Mater. Sci. Eng.* **1024** 012019

IOP Conf. Series: Materials Science and Engineering 1024 (2021) 012019 doi:10.1088/1757-899X/1024/1/012019

Robotized assembly and inspection of composite fuselage panels: the LABOR project approach

Mario Caterino[1], Pasquale Chiacchio[2], Cristina Cristalli[3], Marcello Fera[1], Gaetano Lettera[1], Ciro Natale[1] and Matteo Nisi[3]

[1] Dipartimento di Ingegneria, Università degli Studi della Campania Luigi Vanvitelli, Aversa (CE), Italy
[2] Dipartimento di Ingegneria dell'Informazione ed Elettrica e Matematica applicata, Università degli Studi di Salerno, Fisciano (SA), Italy
[3] Loccioni, Angeli di Rosora (AN), Italy

E-mail: [1]{mario.caterino,marcello.fera, gaetano.lettera, ciro.natale}@unicampania.it
[2] pchiacchio@unisa.it
[3] {c.cristalli, m.nisi}@loccioni.com

Abstract. The aerospace manufacturing is looking at ways to change their production processes in order to improve costs, flexibility and efficiency. The LABOR project, acronym for *Lean robotized AssemBly and cOntrol of composite aeRostructures*, aims at introducing robotic solutions for the assembly line of fuselage panels adopting medium size robots equipped with smart tools, Human Robot collaboration approach and a distributed software architecture. The system consists of a jig that holds the panel to be assembled, two 6-axis robots mounted on moving platforms in order to reach the whole panel and real time measurements to perform the quality control of the assembled components. The cell automatically performs the referencing of the robot working area on the basis of the recognition of geometric features of the parts to be coupled (edges, holes, etc.) through the use of 3D smart inspection tools. After the "one shot" drilling and countersinking operations, the hole is processed to guarantee a high standard of the process. Installation and sealing of the fastener complete the working cycle. Furthermore, an advanced multimodal perception system monitors the collaborative workspace in real time for safe human-robot collaboration (HRC) tasks. The project started in March 2018 as part of the European Clean Sky 2 research program. Three partners - LOCCIONI, UNICAMPANIA and UNISA – are developing the prototype cell in collaboration with LEONARDO S.P.A. that is the Topic Manager.

1. Introduction

One of the main challenges in aerospace manufacturing is to increase the level of automation to improve quality standards, production and efficiency rates and flexibility. These objectives have been reached by means of a lean and flexible automated solution in replacement of manual assembly or complex ad-hoc machine constructions and/or high-payload robots.

1.1. The LABOR project

Aeronautical robotic applications adopt quite heavy and big robots equipped with large, usually multi-functional end effectors (see Section 1.3). LABOR [1] proposes the uses of an assembly jig to hold the panel and two medium size 6-axis robots, namely the internal and the external robot with respect to the curvature of the panel, mounted on linear axes to reach the full length of the panel. A smart inspection tool allows real time measurements and robot self-adaptation to the environment in which they move and to the performed operations. Self-adaptive processing tools for composite structures perform an automatic drilling and fastener insertion, guaranteeing high accuracy. LABOR significantly lowers costs and makes maintenance and programming easy through a distributed intelligence architecture.

1.2. The LABOR requirements

The full demonstrator is compliant with a Technology Readiness Level (TRL) 7 and assemblies a section of fuselage composed of 6 panels containing both windows and doors and divided in a AFT and FWD sides. The assembly cycle starts by referencing the robot working area on the basis of the recognition of geometric features of some parts to be coupled (edges, holes, etc.). Then, a "one shot" drilling and countersinking operation is performed before applying sealant on the proper fastener and complete the automatic cycle by installing it on the panel. These operations are executed on skin shear ties, stringers, intercostal and stringer splices. These components are assembly in three steps: firstly, they are drilled and countersunk by the robots and, then, they are manually removed by human workers for further manual operations. Finally, the workers reinstall the parts on the skin panel and the LABOR cell completes the sealing and riveting operations. The target cycle time is 30 s per hole (excluding fastener inspection) on a CFRP and thermoplastic compound panel with 9 mm grip fasteners. The assembly panel material is a stack CFRP + CFRP or CFRP + Aluminum, with 10 mm maximum thickness. The positioning tolerance is ± 0.2 mm and the normal precision is less than $0.5°$. The system allows co-working activities when human operatiors enter the workcell to insert and remove temporary connecting part, to apply sealant by interposition and to remove metal burrs on the edge of the holes. HRC module is compliant with the current standards as ISO 10218-1/2 [2] [3] and ISO/TS 15066 [4].

1.3. Related works

According to the Global Market Forecast 2018-2037 [5], there is a strong need to increase productivity in the aviation industry to reduce the production costs and increase their efficiency rate. Use of automatic or robotic solutions is very limited especially for regional aircraft manufacturing lines: the high required positioning accuracy can be guaranteed only by using external expensive metrology systems. Existing solutions for fuselage assembly are Airbus A320 [6], Bombardier CSeries Aircraft [7] and FAUB [8] which adopt large robots, heavy end effectors and expensive measurement systems to compensate the unavoidable calibration errors and the limited absolute accuracy, making it impossible to realize HRC activities. On the contrary, in 2017, the VALERI project [9] proposes a mobile manipulator with tactile sensors for supporting human operators. The use of collaborative robots and physical-contact detection systems are unsuitable for industrial purposes because they introduce unsafe solutions and unnecessary production-time loss and low efficiency. Concerning the smart tools, one of the most multi-functional end effectors for composite aerostructure assemby is the MFEE by Kuka Systems Aerospace [10] which possesses functionalities compliant with LABOR but, due to its weight and dimensions, it requires a robot payload higher than 210 kg, as well as, it reaches a positioning accuracy limited to ± 0.5 mm.

2. Workcell Design

The LABOR workcell is shown in Figure 1 and mainly consists of an assembly jig and two 6-axis robots. The former holds the fuselage panel and is equipped with two motors which rotate

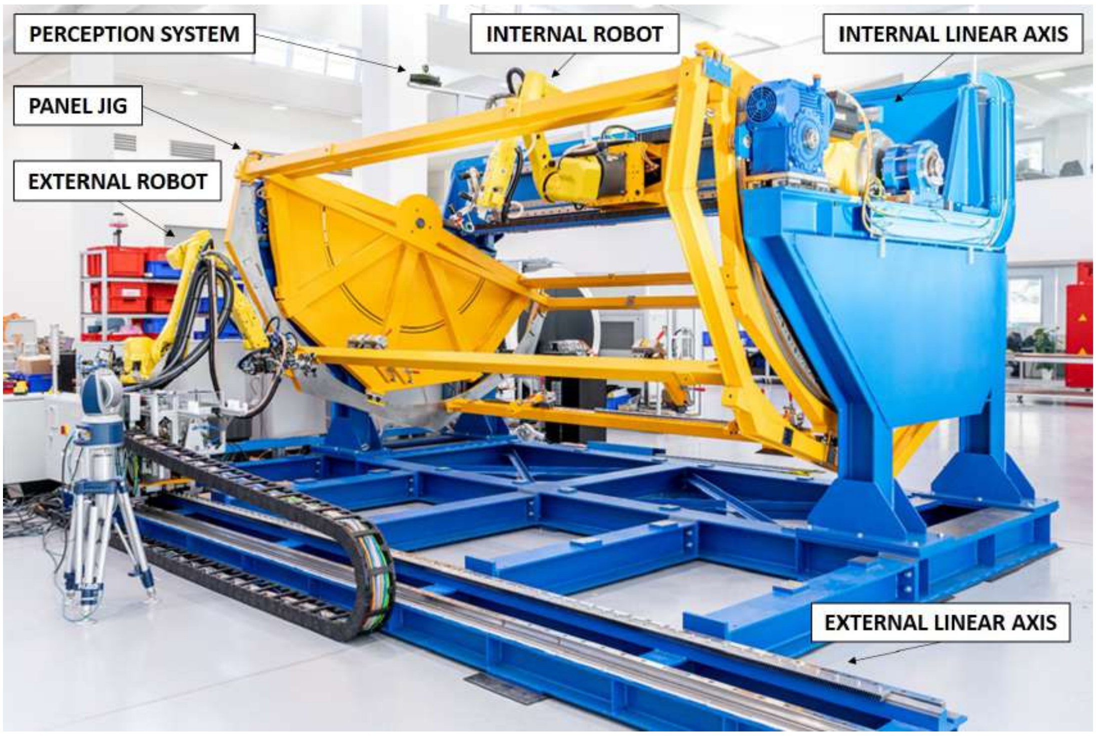

Figure 1: Final workcell design.

the panel during the assembly process, while the robots are mounted on the two sides of the panel and are mounted on linear axes. The cell is supplied with an advanced perception system to monitor the collaborative workspace (see Section 3). There is a *Fastener warehouse* which handles up to 8 different fasteners (with variable diameters and lengths), a *Drilling tip warehouse* which is a carousel of 15 positions, and a dedicated *HRC workstation*. Safety fences are installed to guarantee the operator accessibility. Four dedicated smart tools have been developed.

The external robot handles two different tools (see Figure 2a) that can be exchanged through a quick tool change system placed on the robot basement:

- *Drilling and 2D Inspection Tool*: the robot approaches the drill point and performs an orthogonal alignment with the panel skin through the 3 laser sensors installed around the drilling nose. An automatic electrospindle is mounted on a linear axis to control the advancing motion during the drilling task. A vacuum pipe removes powder and chips, while a force sensor controls the robot during the panel stack clamping. A lubrication system and two telecentric lens on two 2D cameras have been integrated to perform the hole and countersink inspection, i.e. fastener flushness, locking ring, stem height, hole and countersink diameter measurements and absence of burrs check;
- *Fastening and sealing tool*: the pneumatic gripper has been conceived to hold the fastener end. The fastener is automatically selected from the *Fastener Warehouse* and is brought to the gripper tip through a pneumatic transmission system. The fastener is rotated to execute the sealing application through a pneumatic rotary actuator. The sealant gun has been housed into the tool mechanical structure, and connected to the electrical motor that controls the sealant dispensing. Finally, a structured LED light pattern projector and the 2D camera have been integrated to execute the fastener flushness measurement.

The internal robot handles only one tool that is fixed on the robot flange (see Figure 2b). The tool is composed of two parts: the counterthrust tool and the 3D internal inspection tool:

- *Counterthrust tool*: the main component is the counterthrust rod that has been connected through to the suction pipe with the cell aspirator;
- *3D inspection tool*: the structured LED light pattern projector and the three cameras composing the tool have been installed on a screw-nut mechanism actuated by the electric motor. The tool executes the referencing of internal robot with respect to internal panel features and the installed fastener measurements, i.e. delamination and fastener sleeve height and diameter measurements.

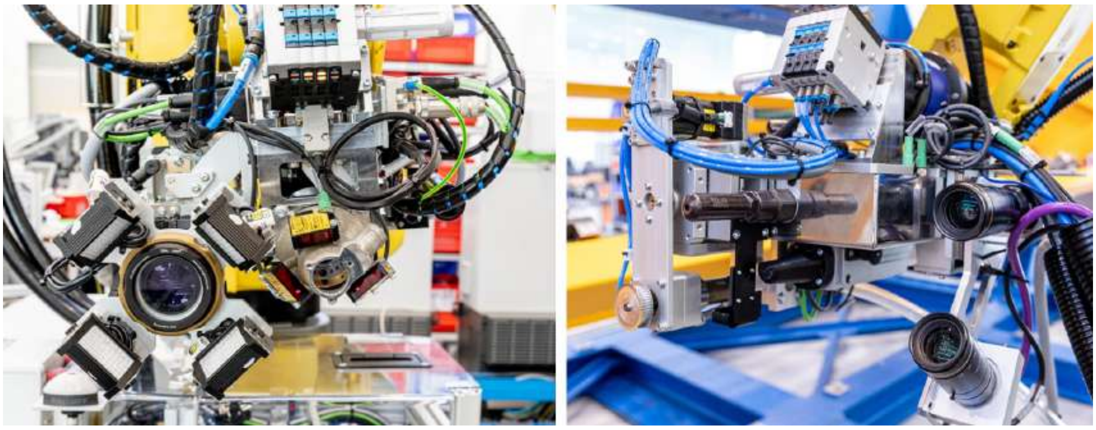

(a) External robot tools: *Drilling and 2d Inspection Tool* (left) and *Fastening and Sealing Tool* (right).

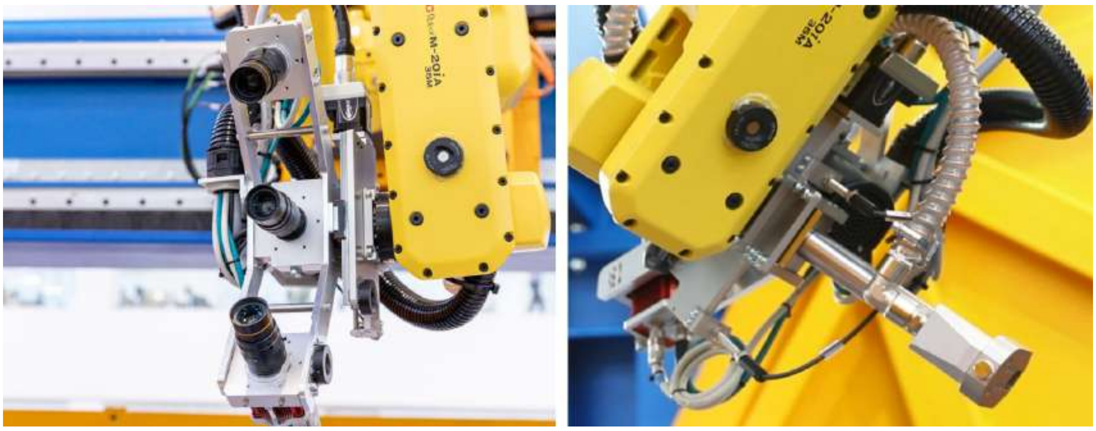

(b) Internal robot tools: *3D Inspection Tool* (left) and *Counterthrust Tool* (right).

Figure 2: External and internal robot self-adaptive tools.

From a software point of view, the main concept of the LABOR architecture is the development and the integration of different intelligent modules. Each module is an independent node which manages all the hardware components and it is related to and communicates only with the HMI module, the cell supervisor. Commands and feedbacks are sent from/to the HMI modules through an OPC-UA bus, the communication protocol chosen according to its intrinsic flexibility, adaptability, transparency which have to be fulfilled to satisfy the distributed intelligence approach. The interaction and communication of each module through the network allow to build a more complex system and to achieve the final complete task.

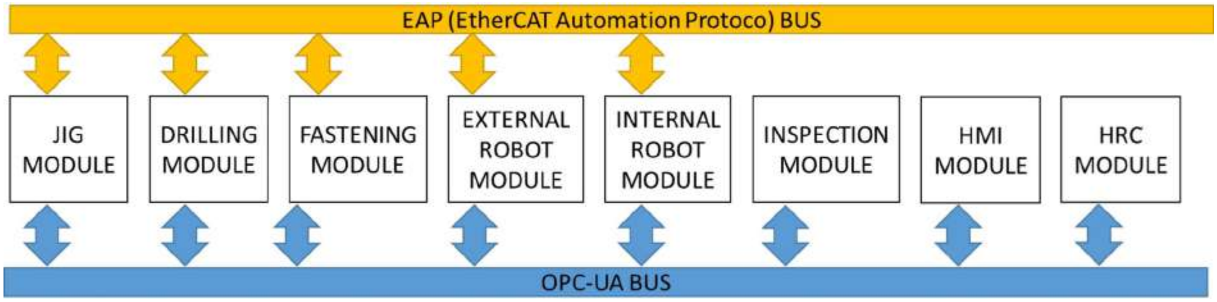

Figure 3: Distributed intelligence architecture.

3. HRC Module

Collaborative robots are typically not used in aerospace manufacturing because of their maximum payload of 35 kg and their limited force-torque safety function. Using conventional industrial robots of medium size for a collaborative cell is possible when integrated them with a safety-rated monitoring system [11]. The LABOR HRC module complies with the robot safety standards ISO 10218-1/2 and TS 15066 by implementing a *Speed and Separation Monitoring* (SSM) scenario. SSM *suggests* to compute the minimum protective distance, S, by considering the maximum robot speed, v_R, as well as the typical human speed, v_H (2000 mm/s):

$$S = \alpha[(v_H T_R + v_H T_S) + (v_R T_R)] + (B) + (C + Z_S + Z_R), \quad (1)$$

where T_R is the time required by the system to identify the operator, T_S is the time required for a complete robot stop, C is the intrusion distance, Z_R and Z_S are the robot and the human position uncertainties and B is the Euclidean distance travelled by the robot while braking.

While the standard equation 1 not foresees α (i.e., $\alpha = 1$), the LABOR approach introduces α representing a scaling factor which evaluates the current risk assessment analysis (see Section 3.2). Moreover, the adopted solution heavily considers the current v_R and v_H.

3.1. Related works

Standard optical protection devices use laser scanner technology to separate humans from the robots [12]. The off-the-shelf devices ([13] and [14]) divide the layout of the shared workspace into three zones associated with pre-defined, constant robot speeds which are selected according to the worker distance from the robot. In literature, motion capture systems are combined with range sensors [15] or artificial vision systems [16] for distance monitoring. This is the most suitable approach for pure coexistence in a collaborative workspace but the current solutions are no robust for industrial applications and produce a high percentage of false positives during the human tracking step, thus producing unnecessary robot stops which get worse production time. On the other hand, a common approach for the robot speed monitoring consists in using a reactive motion planning that modifies the pre-programmed path to generate a new collision free path [17], [18]. Unfortunately, in manufacturing environments it is often required not to modify the robot pre-programmed path because it can involve violation of some constraints. Reliable monitoring of the dangerous zone can make the robot slowing down when necessary, as shown in Section 3.2.

3.2. Reliable human detection and control system solution

The adopted multimodal vision system combines the 3D data, acquired from a depth sensor, with their thermal information, read from a thermal camera. Details about the whole developed pipeline have been originally reported in [19]. By merging depth and thermal data through a

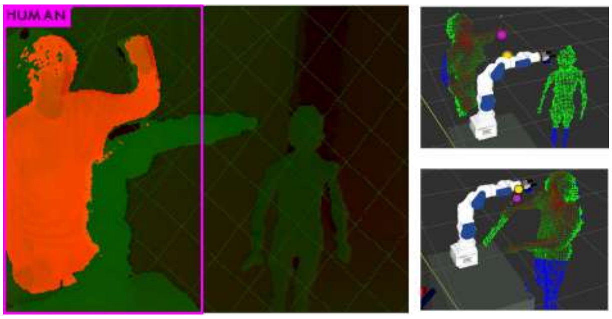

Figure 4: Reliable human detection: the depth-thermal image (left) read by the CNN to distinguish human operator from a plastic mannequin and thermal point cloud (right) showing the purple sphere belonging to the human cluster at minimum distance with respect to the yellow robot sphere.

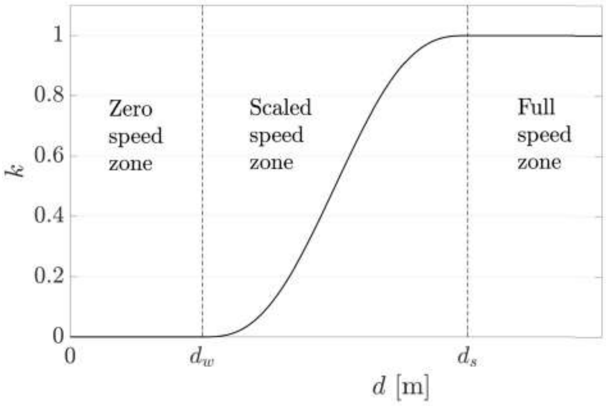

Figure 5: Relation between d and k; S is the minimum separation distance computed in real time as in equation (1)

novel image mapping approach (Figure 4 left), a retrained YOLOv3 [20] convolutional neural network (CNN) executes a reliable detection of human workers. In real time, a thermal point cloud computes the separation distance, d, between the human worker and the robot, thus selects both $\boldsymbol{p_R}$ and $\boldsymbol{p_H}$ (with its own temperature), the point belonging to the robot surface and the one belonging to the worker, respectively (Figure 4 right). From this step, the algorithm estimates v_H and v_R, i.e. the magnitudes of the instantaneous velocities of these points, projected along the direction identified by them. By collecting this data, S is computed as in equation 1, considering the current values of d, v_R, v_H, the temperature of $\boldsymbol{p_H}$, as well as the current risk assessment estimated through a fuzzy logic which computes in real time the α value ([0,1]). By comparing S and d as shown in Figure 5, the control algorithm estimates the scaling factor k ([0%, 100%]) to be directly used as the speed override of all the robot motion instructions. More details are reported in [21].

Table 1: General aircraft panel assembling operations without and with HRC

	WITHOUT HRC		WITH HRC	
OP CODE	HUMAN	ROBOT	HUMAN	ROBOT
OP10	Shear ties, frames and aluminium stringers assembly on SFRP skin	NA	Shear ties, frames and aluminium stringers assembly on SFRP skin	NA
OP20	Panel drilling	NA	NA	Panel drilling
OP30	Panel countersinking	NA	NA	Panel countersinking
OP40	Hole inspection	NA	NA	Hole inspection
OP50	Stringers de-assembling	NA	Stringers de-assembling	NA
OP60	Stringers cleaning	NA	Stringers cleaning	NA
OP70	Stringers deburring	NA	Stringers deburring	NA
OP80	Sealant application	NA	Sealant application	NA
OP90	Stringers re-assembling	NA	Stringers re-assembling	NA
OP100	Panel riveting	NA	NA	Panel riveting

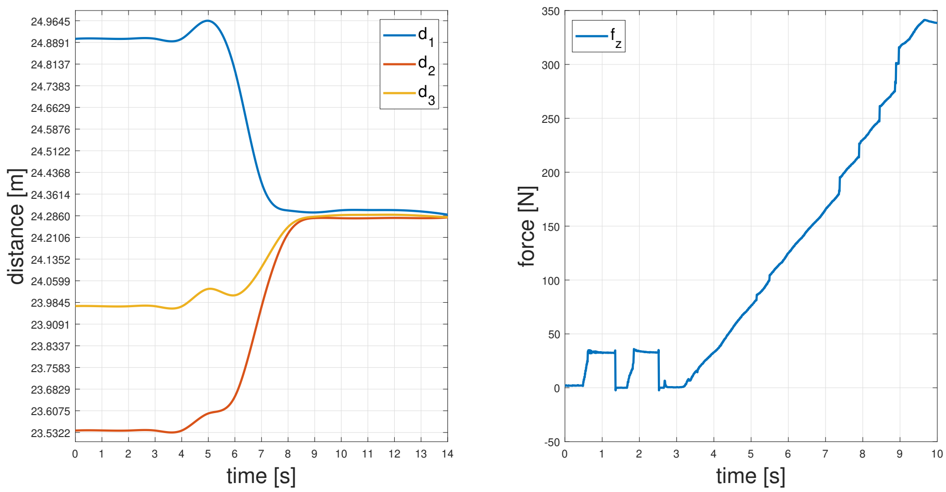

Figure 6: Distances read by the laser sensors during the alignment operation to ensure the drilling axis is orthogonal to the panel skin (left); clamping forces measured during the panel stack clamping operation (right).

3.3. Optimization of the collaborative work cycle

To fully exploit the HRC module functionality, the work cycle of the SIDE FWD panel, which needs the combination of both robot and manual activities, has been redefined with respect to a fully-automated work cycle (Table 1). The main idea is that the human worker and the internal robot can work simultaneously on different panel areas. This approach ensures the human safety by executing the collaborative algorithm described in Section 3.2. Simulated analyses estimate that the time to manually assemble the panel is around 15 h. LABOR reduces the working time of about 40% with a standard fully-automated working cycle, while the percentage rises by using the HRC module (48%).

4. Cooperative control of robots

The application of a clamping force is needed to produce a local stiffening of the panel, in order not to bend or damage it and to avoid burrs in the interface between the different parts of the stack during the *one-shot* drilling operation. This objective has been achieved through the use of cooperative thrusts from both robots, based on force measurements. The external and internal robots coordinate themselves to build up the desired clamping force thus realizing the clamping of stacks of material. Note that the adoption of force sensors allows the monitoring of forces during the entire drilling process.

The open-loop solution is based on the idea that both the drilling tool of the external robot and the counter-thrusting tool of the internal one push the panel until a force threshold is reached. The operation is divided into three thrusts, as shown in Figure 6 (right): the external robot approaches the panel and applies 30N along the drilling axis in 1.5s, then the internal robot approaches the panel in the opposite direction by applying 30N in 1.5s and, finally, the external robot completes the pre-load application till 340N. Note that sensor readings are zeroed after each thrust to specify only force variations. To guarantee the required hole axis angular tolerance of ± 2 deg, before the clamping force operation, the drilling axis of the external robot is aligned to ensure normality to the panel surface. The alignment operation rotates the robot tip around the drilling point by reading the values of the three laser sensors mounted on the drilling tool till the three distances are inside the required tolerances, as shown in Figure 6 (left).

5. Conclusions

The paper describes the main requirements of the LABOR project, the main components of the cell and the operations to be performed, i.e. drilling, sealing, fastening, inspection, HRC by summarizing the main proposed approaches. Based on these requirements, the developed drilling, fastening, sealing, clamping, referencing and inspection tools are presented paying attention to the dimensions of the tools and the number of tool changes required in order to meet the objectives of the project, i.e. to adopt the concept of lean automation involving the use of small/medium size robots. Moreover, ergonomics, flexibility and reduced costs of the overall structure has been described, as well as an overview of the developed human-machine collaboration system architecture. A video showing the main functionalities of the LABOR cell is available at https://images.loccioni.com/Share/142d68f4-49f9-4b46-bb96-621e3440042b.

Acknowledgement

This work has received funding from the Clean Sky Horizon 2020 Programme under the LABOR project, GA n. 785419, with Leonardo S.p.A. as Topic Manager.

References

[1] The LABOR project 2019 https://www.labor-project.eu/
[2] 2011 ISO 10218-1 - Robots and robotic devices - Safety requirements for industrial robots. Part 1: Robots. Standard International Organization for Standardization
[3] 2011 ISO 10218-2 - Robots and robotic devices - Safety requirements for industrial robots. Part 2: Robot system and integration. Standard International Organization for Standardization
[4] 2016 ISO/TS 15066 - Robots and robotic devices - collaborative robots. Standard International Organization for Standardization
[5] Global Market Forecast 2019-2038 https://www.airbus.com/aircraft/market/global-market-forecast.html
[6] Airbus inaugurates new A320 structure assembly line in Hamburg 2019 https://www.airbus.com/newsroom/press-releases/en/2019/10/airbus-inaugurates-new-a320-structure-assembly-line-in-hamburg.html
[7] Bombardier to Combine Efficiency and Quality in Manufacturing of CSeries Aircraft 2011 https://www.bombardier.com/en/media/newslist/details.636-bombardier-to-combine-efficiency-and-quality-in-manufacturing-of-cseries-aircraft.bombardiercom.html
[8] A Futuristic View Of The 777 Fuselage Build 2014 http://www.boeing.com/features/2014/07/bca-777-fuselage-07-14-14.page
[9] The VALERY project http://www.valeri-project.eu/
[10] Kuka MFEE multi-functional end effector https://www.yumpu.com/en/document/view/34034049/kuka-mfee-multi-functional-end-effector-kuka-systems
[11] Walton M, Webb P and Poad M 2011 *SAE Technical Paper Series* 2011-01-2655
[12] Krüger J, Lien T and Verl A 2009 *CIRP Annals* **58**(2) 628–646
[13] SICK website www.sick.com
[14] Safe camera system SafetyEYE https://www.pilz.com/it-it/eshop/00106002207042/safetyeye-safe-camera-system
[15] Cifuentes C A, Frizera A, Carelli R and Bastos T 2014 *Robotics and Autonomous Systems* **62** 1425 – 1439 ISSN 0921-8890
[16] Flacco F, Kröger T, Luca A D and Khatib O 2012 *2012 IEEE International Conference on Robotics and Automation* (Saint Paul, Minnesota, USA: IEEE)
[17] Zhang P, Jin P, Du G and Liu X 2016 *Industrial Robot: An International Journal* **43** 264–273
[18] Lippi M and Marino A 2018 *IFAC-PapersOnLine* **51** 190–196
[19] Costanzo M, Maria G D, Lettera G, Natale C and Perrone D 2019 *2019 IEEE International Conference on Systems, Man and Cybernetics* (Bari, I: IEEE) pp 692–699
[20] Redmon J and Farhadi A 2018 *CoRR* (*Preprint* arXiv:1804.02767)
[21] Campomaggiore A, Costanzo M, Maria G D, Lettera G and Natale C 2019 *16th International Conference on Informatics in Control, Automation and Robotics* (Prague, CZ: Scitepress) pp 78–87

A multimodal approach to human safety in collaborative robotic workcells

Marco Costanzo, *Student Member, IEEE,* Giuseppe De Maria, Gaetano Lettera, *Student Member, IEEE,* and Ciro Natale.

***Abstract*—The paper investigates the problem of controlling the speed of robots in collaborative workcells for automated manufacturing. The solution is tailored to robotic cells for cooperative assembly of aircraft fuselage panels, where only structural elements are present and robots and humans can share the same workspace, but no physical contact is allowed, unless it happens at zero robot speed. The proposed approach addresses the problem of satisfying the minimal set of requirements of an industrial Human-Robot Collaboration (HRC) task: precision and reliability of human detection and tracking in the shared workspace; correct robot task execution with minimum cycle time while assuring safety for human operators. These requirements are often conflicting with each other. The former does not concern with safety only but also with the need of avoiding unnecessary robot stops or slowdowns in case of false positive human detection. The latter, according to the current regulations, concerns with the need of computing the minimum protective separation distance between the human operator and the robots by adjusting their speed when dangerous situations happen. This paper proposes a novel fuzzy inference approach to control robot speed enforcing safety while maximizing the level of productivity of the robot minimizing cycle time as well. The approach is supported by a sensor fusion algorithm which merges the images acquired from different depth sensors with those obtained from a thermal camera, by using a machine learning approach. The methodology is experimentally validated in two experiments, the first one at lab-scale and the second one performed on a full-scale robotic workcell for cooperative assembly of aeronautical structural parts.**

***Note to Practitioners*—The paper discusses a way to handle human safety specifications vs. production requirements in collaborative robotized assembly systems. State-of-Art (SoA) approaches cover only a few aspects of both human detection and robot speed scaling. The present research work proposes a complete pipeline which starts from a robust human tracking algorithm and scales the robot speed in real time. An innovative multimodal perception system composed of two depth cameras and a thermal camera monitors the collaborative workspace. The speed scaling algorithm is optimized to take on different human behaviors during less risky situations or more dangerous ones to guarantee both operator safety and minimum production time with the aim of better profitability and efficiency for collaborative workstations. The algorithm estimates the operator intention for real-time computation of the minimum protective distance according to the current safety regulations. The robot speed is smoothly changed for psychological advantages of operators, both in case of single and multiple workers. The result is a complete system, easily implementable on a standard industrial workcell.**

***Index Terms*—Human-robot collaboration, Fuzzy control logic, Safety standards, Multimodal perception system, Workspace monitoring, Motion planning, Industrial robot, Convolutional neural network.**

M. Costanzo, G. De Maria, G. Lettera and C. Natale are with the Department of Computer Engineering, Universit degli Studi della Campania Luigi Vanvitelli, 81031 Aversa, Italy. e-mail: {marco.costanzo, giuseppe.demaria, gaetano.lettera, ciro.natale}@unicampania.it.

Manuscript received xxx, 2019; revised xxxx, 2019.

I. Introduction

ROBOTS of the future should be employed safely, intelligently and adaptively in many automated manufacturing environments. Humans and robots have to interact and communicate effectively and efficiently during their movements in order to maximize the system productivity and preserve operator safety at the same time. To achieve such challenging objectives, a perception system is needed for monitoring human presence reliably, and suitable control algorithms should be devised to select the proper robot behaviour for keeping a high level of productivity in a collaborative scenario. This paper leverages machine learning techniques based on a multimodal perception and a novel sensor fusion algorithm for human tracking, as well as a fuzzy control logic to detect the proximity and the speed interaction between human operators and robots in real-time.

A. Context and motivations

The research work is carried out in the framework of the LABOR European project [1], which has the objective to propose novel robotized assembly paradigms of aircraft fuselage panels by integrating human capabilities in a robotized assembly system. Until recently, the aerospace industry was still conservative and companies tended to use successful assembly methods that had already been proven to work in the past. Nowadays, many assembly sub-operations try to exploit robotics, e.g., drilling, fastening and sealing tasks. These operations are no longer manually performed by human operators but by industrial robots equipped with dedicated tools or by large automated machines devoted to assembly of specific parts. However, there are some operations which require human capabilities and that must be executed by operators in coexistence with robots. An example in this context is [2], where humans and robots collaborate to perform installation applications inside the fuselage. This is also the case of hybrid metal and composite structures, where, after the drilling operation, some parts have to be manually removed for further manual operations, like deburring, and then re-installed on the skin panel before the sealing and riveting operations, as shown in Fig. 1. Automated assembly applications demonstrate that the greatest advantage brought by collaborative robots lies in the opportunity to combine the advantages of automation with the flexibility and soft skills of human workers. These systems also prevent workers from tedious, complex and

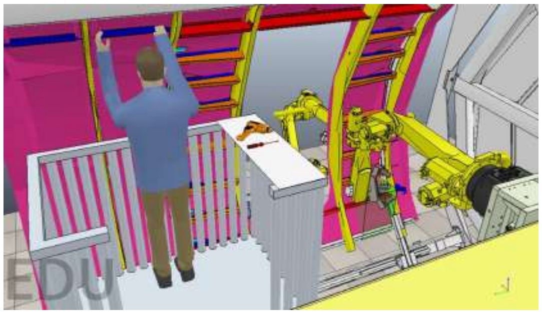

Fig. 1. Example of a manual assembly operation: the operator removes the blue element from the panel for the execution of deburring operations.

ergonomically not feasible jobs and increase productivity of the industrial process. Specifically, traditional industrial robots continuously perform the same tasks and reach levels of accuracy, speed and repeatability which are impossible to be achieved by humans. However, they lack in versatility and cannot efficiently adapt to dynamic working environment or changes in production.

Preliminary versions of the approach proposed in this paper have been originally reported in [3] and [4]. The present paper extends those works by proposing a new fuzzy control strategy and an improved perception pipeline to further reduce cycle time, it presents new challenging case studies and counterexamples to support the solution, finally, it adds implementation details to make the proposed strategy fully reproducible.

B. Classification of safety standards

Safety is the fundamental prerequisite in the design of human-robot collaborative workplaces. The International Organization for Standardization (ISO) 10218-1 [5], 10218-2 [6] outline some methods for safe collaborative work and ISO/TS [7] supplements them and provides additional guidance for safety in HRC. The safety standards address four collaborative scenarios, i.e.: *Safety-rated Monitored Stop*, *Hand Guiding*, *Speed and Separation Monitoring* (SSM) and *Power and Force Limiting*. In the SSM scenario (the one selected in this application), the safety is ensured by maintaining at least the protective separation distance between the operator and the robot all the time (the slower the robot speed is, the smaller separation distance is allowed and, if the separation distance decreases below the minimum protective separation distance, the robot has to stop).

The safety collaborative scenarios can be divided into two categories: *post-collision* and *pre-collision* [8]. A *post-collision* system reacts after the physical impact occurs between the robot and the operator. In this case, the collision could be dangerous if the robot limits are poorly defined or when the robot is equipped with sharp tools, e.g., drilling tools; moreover, any collision stops the task execution, thus affecting production time. Human safety can be assured by minimizing the energy transmitted during the contact [9], [10] by using robots endowed with sensors for assessing force exchange when the impact occurs, e.g., force or tactile sensors [11], or by using only proprioceptive measurements in case of industrial manipulators With closed control architecture [12]. On the other hand, a *pre-collision* scheme makes use of exteroceptive sensors to detect humans and prevent collisions. Motion capture systems combined with range sensors [13] or artificial vision systems [14] are crucial in the case of distance monitoring, used in workspaces with human-robot coexistence only. The dangerous zone around the robot is monitored and any operator that accesses it makes the robot slowing down, until a full stop when the human is too close.

Industrial safety requirements do not permit to use *post-collision* systems, therefore, this paper presents a novel *pre-collision* strategy based on the SSM scenario, that means no physical contact is allowed between the robot and the operator, unless it happens at zero robot speed. Two main methods have been developed and integrated: Safety Through Prediction (STP) and Safety Through Control (STC). STP is based on the use of a multimodal perception system (depth and thermal camera) for a reliable detection of human operators. This has been pursued by tracking separation distance and by predicting human actions and motions. STC includes a strategy to prevent collisions by defining safety regions, according to the current regulations, and designing control actions to decrease robot speed only when indispensable, depending on the actual risk of collision.

1) Safety through prediction: Localizing human operators robustly requires to fuse several sensors with different physical properties [15], [16], [17]. The present paper makes use of a thermal camera to find humans into the observed scenario, which have a surface temperature around 37° C. The reason of choosing this type of sensor is related to its intrinsic principle of robustly identifying and distinguishing temperature data also when illumination and viewpoint change. Unfortunately, thermal camera does not support depth information for the separation distance measurement required by the current regulations. This paper demonstrates that a robust real-time human detection strategy can be obtained through a multimodal perception system which combines 2D thermographic data and 3D depth information. The approach can be classified as a device-free technology and compared to other methods of the same class, e.g., those based on radio frequency transceivers [18], [19], is able to detect body parts with a higher level of detail and better accuracy.

Section III-A gives emphasis to the novel extrinsic camera calibration procedure. Section V provides experimental results to prove the effectiveness of the proposed method and compares the proposed solution with some SoA strategies. Finally, the pipeline which computes the points at minimum distance has been strengthened by adding a new step which produces a thermal point cloud to distinguish points belonging to the human body surface from the tools held by the worker. This information will be taken into account by the control system to better handle the robot speed modulation according to a risk analysis.

2) Safety through control: The main objective of the proposed method is to scale down the robot pre-programmed speed when a real and imminent danger of collision between the robotic system and a human worker occurs. The operator safety is assured by analyzing his/her behaviour when entering the collaborative workspace and by quantifying the level of risk to which he/she is exposed during the task execution. This analysis is complex due to the extreme variability and unpredictability of human behaviours.

A first known approach usesa reactive motion planning that modifies the pre-programmed path to generate a new collision free path [20], [21]. Unfortunately, in manufacturing environments it is often required not to modify the robot pre-programmed path because it can involve violation of some of the production constraints. This paper presents a methodology to generate an optimal motion taking into account both safety and production constraints. A novel distance-controlled velocity strategy is introduced, which adapts the robot speed on an assigned path, not only to the perceived distance with respect to the closest human worker, as suggested by the current regulations, but also with respect to the relative position and velocity of the operator and the robot used in the risk assessment analysis. The recent paper [22] proposes a general framework for computer-aided risk assessment based on a temporal logic language. It deals also with the SSM method as a risk reduction measure, however the robot is slowed down based on fixed thresholds for the protective distance. Whereas, the method based on the FIS proposed here generates a smoother modulation of the protective distance S; moreover, the risk assessment rules can be specified in natural language rather than in a formal one.

In [3] and [4] the risk is assessed only on the basis of the relative position and velocity, here the risk assessment algorithm takes into account also the thermal information of the selected point at minimum distance belonging to the worker. This new input has been introduced to better distinguish dangerous situations for the workers from cases of possible collisions with nearby obstacles, typically tools used by the worker.

C. Paper contributions

The paper discusses solutions to handle safety specifications vs. production requirements in HRC environments. Although several works about the same topic exist, to the best of the authors' knowledge, none or just few of the aforementioned approaches cover all the relevant challenges in an exhaustive manner or have been explicitly designed to be consistent with the production requirements, aiming at maximizing the overall throughput. The main contributions of the present research work are

- development of a reliable human detection through a multimodal perception system with depth and thermal cameras able to handle multiple workers (see Section III);
- definition of a new thermal point cloud to distinguish human body parts from handheld tools, used to separate less risky situations from more dangerous ones;
- development of a fuzzy-based risk analysis to correctly evaluate dangerous situations and avoid unnecessary robot stops (see Section IV-A);
- development of a strategy which properly identifies the points at minimum distance considering all parts of the human bodies and all links of the robot (see Section III-C);
- real-time adaptation of the minimum protective separation distance defined in the current regulations on the basis of the risk analysis (see Section II and Section IV-A);
- development of an intention estimation predictive technique through real-time estimation of human velocity based on a Kalman filter (see Section III-C).

II. Assessment and measure of the risk in collaborative environments

The ISO 10218-1/2:2011 underlines the importance of hazard identification and set the mandatory requirements of risk assessment, especially for collaborative robots and for those operations that dynamically involve the operator and the robot, as in SSM scenarios. The ISO TS 15066 provides additional information and further guidelines to evaluate the risk related to the four types of collaboration modes (see Section I-B). Assuming as fundamental requirement a maximum safe reduced speed of 250 mm/s over the collaborative operations [6], it presents the acceptable physical quantities for the collaborative modes of SSM, such as the allowable *minimum protective separation distance*, S, between the human operator and the robot.

The ISO TS 15066 suggests to compute S by using the relation

$$S = v_H T_R + v_H T_S + v_R T_R + B + C + Z_S + Z_R, \qquad (1)$$

where

- v_H represents the maximum speed of the closest operator and it is assumed as 2000 mm/s with the option to use 1600 mm/s when $S > 500$ mm;
- v_R is the maximum robot speed;
- T_R is the time required by the machine to respond to the operator presence;
- T_S represents the response time of the machine which brings the robot to a safe, controlled stop;
- C is the intrusion distance safety margin, which represents an additional distance, based on the expected intrusion toward the critical zone prior to the actuation of the protective equipment;
- Z_R is the robot position uncertainty;
- Z_S is the operator position uncertainty (i.e., the sensor uncertainty);
- B is the Euclidean distance travelled by the robot while braking.

The rational behind this choice is that, during the robot motion, the robot never gets closer to the operator than S. When the Euclidean separation distance, d, is equal to or less than S, the robot system stops, before it can impact the operator. When the operator moves away from the robot, this can resume the motion automatically while maintaining at least the minimum protective separation distance.

This metric is only suggested but it is not mandatory, since the regulation allows the user to adopt different metrics based on a documented risk analysis. The present work starts from the suggested metric (1) and tries to improve some aspects to optimize the production time. To this aim, S has been redefined as follows

$$S(t) = \alpha(t)[v_H(t)T_R + v_H(t)T_S + v_R(t)T_R] + B + C + Z_S + Z_R, \quad (2)$$

where $\alpha(t)$ is a scaling factor, which can be evaluated according to a suitable risk assessment analysis, and $v_H(t)$ and $v_R(t)$ are the magnitudes of the instantaneous velocities of the points at minimum distance belonging to the human operator and the robot, respectively, projected along the direction identified by these two points (see eqs. (13) and (14)). The actual value of α will also take into account if the robot and the human are approaching or they are moving away (see end of Section III). The scaling factor can assume values in the interval $[0, 1]$: α should be close to 1 when the current situation is actually dangerous for the worker and it is necessary to follow the TS suggestions, whereas α can take smaller values when the current situation is less risky for the operator, so it is possible to relax the constraints given by TS. In addition, the velocity values are not constant as suggested by TS, but they are estimated in real time to properly adapt the estimation of S to the current scenario.

III. Safety Through Prediction

The perception of the presence of human operators inside the collaborative workspace must be extremely reliable and ensure human safety in every situation. For the computation of the minimum distance, it is possible to geometrically represent the robot simply as its tool center point (TCP) or as a kinematic chain of primitive shapes like spheres or ellipsoids [23]. Usually, the human body is represented as a parallelepiped object [24] or as a stick figure using colour markers on the clothes and skeletal trackers [25], [26]. Considering only the TCP might prevent reaching the desired safety level since collisions with other links of the robot are not taken into account. In this paper, the whole robot is modeled through a virtual 3D model, by drawing dynamic bounding spheres around each link that follow robot movements in real time. The human operators are observed by capturing real images from a multimodal perception system that provides a point cloud representation enhanced with temperature information. In this way, the measurement of the separation distance between the 3D robot model and the closest human operator considers the whole body surface, thus ensuring a higher degree of safety.

A. Experimental setup configuration

The experimental setup demonstrates that the use of multiple sensors can involve advantages for the workspace monitoring. Two depth cameras have been adopted to solve the risk of occlusions: the *Microsoft Kinect v1* and the *Intel RealSense D435*. At the same time, a sensor fusion technique with a thermal camera has been developed to decrease the false positive detection. The *Optris PI 450* thermal camera has been rigidly attached to the Kinect depth camera and they have been arranged in a way that their optical axes are aligned. Fig. 2 shows an image of the setup.

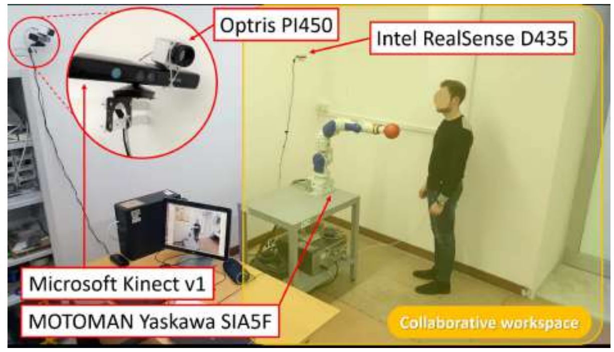

Fig. 2. Multimodal perception system: two depth cameras and a thermal camera for monitoring the collaborative workspace.

1) Depth-Depth camera calibration: The intrinsic calibration of the depth cameras has been necessary to adjust the default intrinsic parameters. It is carried out using a standard procedure and a chessboard pattern [27]. The extrinsic calibration has been necessary to obtain the homogeneous transformation matrices, $\boldsymbol{T}_{d_1}^b$ and $\boldsymbol{T}_{d_2}^b$, which express the poses of the depth camera frames with respect to the robot base frame. In literature, this problem is solved by different calibration procedures, especially for object recognition applications. Their typical target is to recognize objects located at about $0.5\,\mathrm{m}$ from the camera frame. On the contrary, for a typical industrial environment, the robot and the operators work in a large workspace and more than $2.5\,\mathrm{m}$ far from the camera. Therefore, a new sphere-tracking extrinsic calibration procedure for depth cameras has been proposed.

A red polystyrene sphere has been mounted at the robot TCP, so as to match the center of the sphere with the origin of the known end-effector frame, as shown in Fig. 2. The calibration procedure is based on the *M-estimator SAmple Consensus* (MSAC) algorithm [28] which is an extension of the well-know *RANdom SAmple Consensus* (RANSAC) algorithm [29]. The original depth images are converted into point clouds [30] and MSAC estimates the geometric model of the sphere, satisfying a constraint on the sphere radius dimension. The robot configuration must guarantee that the sphere can be properly visible in both camera images, without using RGB data (see Fig. 3). For each robot configuration, the forward kinematics computes the center sphere pose. A cost function combines the estimated poses from both cameras and evaluates $\boldsymbol{T}_{d_1}^b$ and $\boldsymbol{T}_{d_2}^b$. The mean positioning error achieved by applying this calibration procedure is about $0.015\,\mathrm{m}$ for the Kinect camera and $0.042\,\mathrm{m}$ for the Intel one, against $0.10\,\mathrm{m}$ achieved by using SoA techniques, due to the large monitored workspace at hand ($20\,m^3$).

2) Depth-Thermal camera calibration: The software adopted for the thermal camera intrinsic calibration [27] needs a perforated grid with a circular pattern. A novel extrinsic calibration procedure has been proposed in this paper to define the thermal camera pose with respect to the depth camera.

In [31] and [32] a thermal camera and a depth camera are extrinsically calibrated by using a perforated grid placed in front of the sensors. These procedures assume that the target

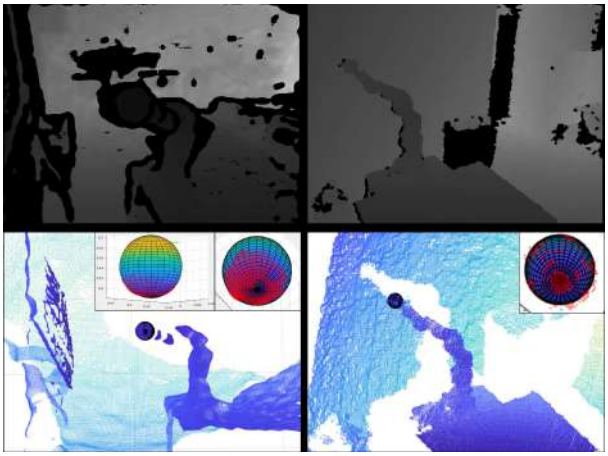

Fig. 3. Depth camera extrinsic calibration procedure: the original depth images (top) are converted in point clouds (bottom) to allow MSAC to estimate the sphere model pose by finding the correspondences, i.e., the inliers (red points).

is located close enough to the sensor lenses, at about $0.5\,\mathrm{m}$. These assumptions could not be met in the application scenario at hand, due to the large distance at which the camera should work.

The solution consists in using three heated spheres attached to a flat cardboard support placed far from the camera, where the human operators are expected to work. This assumption guarantees that the calibration output provides an accurate correspondence when the two images are overlapped. Note that if the two cameras have different fields of view (FOV), the flat cardboard support must be placed carefully inside the common view.

To estimate the transformation matrix $\boldsymbol{T}_t^{d_1}$, between the depth camera frame Σ_{d_1} and the thermal camera frame Σ_t, the spheres have been moved inside the collaborative workspace. The coordinates $\boldsymbol{p}_k^{d_1} = \begin{bmatrix} x_k^{d_1} & y_k^{d_1} & z_k^{d_1} \end{bmatrix}^T$ of the kth center of the target sphere have been directly calculated from the depth image, while the corresponding thermal point coordinates have been calculated from the thermal image, assuming the distance from the lens equal to the depth value, i.e., $z_k^t = z_k^{d_1}$, and

$$x_k^t = \frac{(a_k - c_{x_t}) z_k^t}{f_{x_t}}, \; y_k^t = \frac{(b_k - c_{y_t}) z_k^t}{f_{y_t}}, \tag{3}$$

where a_k and b_k are the pixel coordinates of the sphere center in the thermal image, c_{x_t}, c_{y_t} are the pixel coordinates of the thermal image center and f_{x_t}, f_{y_t} are the focal lengths expressed in pixel-related units. Finally, the transformation matrix $\boldsymbol{T}_t^{d_1}$ has been estimated by minimizing a cost function that combines the corresponding data.

B. Human Detection and Tracking

An innovative Convolutional Neural Network (CNN), which merges spatial and thermal data, is presented to detect human workers. Introducing a novel representation consisting in a RGB-D point cloud, two pipelines have been implemented: the *Segmentation Pipeline* and the *Sensor Fusion Pipeline*.

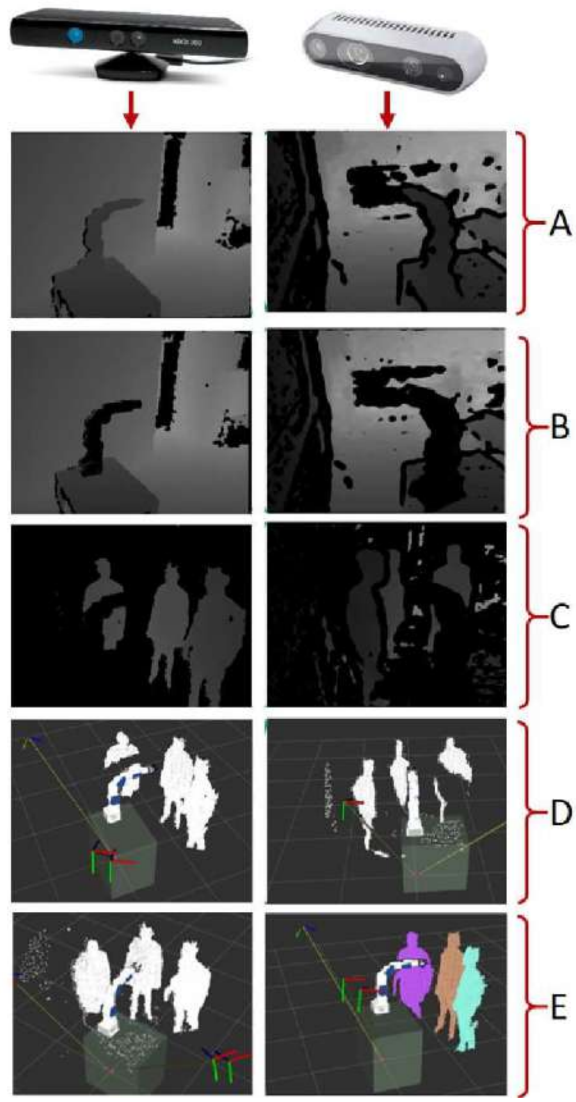

Fig. 4. Segmentation pipeline: the original depth images (step A) are processed by removing the robot model (step B) and then subtracted to the static background to recognize dynamic entities (step C). The corresponding point clouds (step D) are merged and processed to divide the entities into independent clusters (step E).

1) Segmentation Pipeline: The first step of the proposed segmentation pipeline is subtracting the static environment from the original depth image in order to process exclusively dynamic entities. This idea simplifies the point cloud to be analyzed, because unnecessary points are discarded. Fig. 4 shows five main steps which are detailed below.

Step A shows that the original depth images contain not only the robot surroundings but also the robot itself. This means that the moving robot could be classified as a dynamic entity. The *Real-time URDF Filter* [33] package identifies the pixels belonging to the robot model and assigns them a Not-a-Number (NaN) value (step B). At this point, the background filtering can be made: every dynamic entity which enters the collaborative workspace is now recognized into the processed depth image.

The second part of the segmentation pipeline makes use

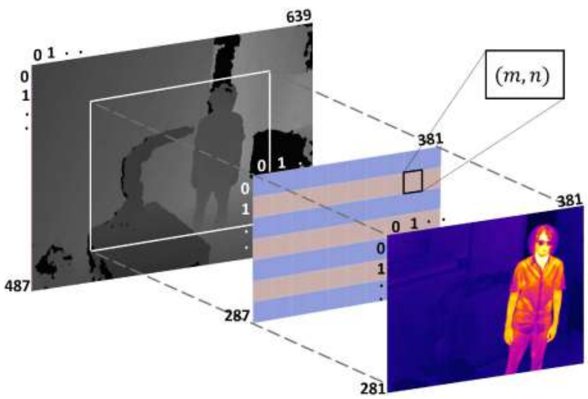

Fig. 5. The proposed pixel-by-pixel mapping technique to find correspondences between the depth image and the thermal image: the result is a 382×288 matrix.

of point cloud data (PCD) which the two depth images are converted to (see step D). Chosen a depth camera as the reference one, the PCDs are expressed relative to the same camera frame. Step E (left) shows the next point cloud merging phase which demonstrates the accuracy reached during the extrinsic calibration procedure (Section III-A1). Finally, a clustering process (step E, right) provides as many clusters as single dynamic areas are detected in the foreground. The step uses an Euclidean cluster extraction method. The image shows three detected dynamic clusters colored by random colors and visualized in RViz together with the robot model.

2) Sensor Fusion Pipeline: The sensor fusion pipeline strength is the CNN trained on images obtained by combining both depth and thermal data. The approach guarantees robust human detection in real time with very low sensitivity to lighting conditions owing to the combination of the two image sources and it consists in four key phases described in the following.

Phase 1: depth-thermal mapping. The extrinsic calibration explained in Section III-A2 is the first step towards a correct mapping, that means finding correspondences between the depth image and the thermal image. Since the adopted cameras have different FOVs and resolutions, the resulting map size must correspond to the smallest one. According to the experimental setup shown in Fig. 2, the mapping procedure builds a 382×288 matrix. The mapping phase has been solved through a pixel-by-pixel procedure as shown in Fig. 5: the pixel of the depth image, of indices (m, n), contains the depth value, $z^d_{m,n}$, which is read to compute the corresponding Cartesian point $\boldsymbol{p}^d_{m,n} = \begin{bmatrix} x^d_{m,n} & y^d_{m,n} & z^d_{m,n} \end{bmatrix}^T$, similarly to (3),

$$x^d_{m,n} = \frac{(m - c_{x_d}) z^d_{m,n}}{f_{x_d}}, \; y^d_{m,n} = \frac{(n - c_{y_d}) z^d_{m,n}}{f_{y_d}}. \quad (4)$$

The Cartesian point is then expressed with reference to the thermal camera frame through the relation

$$\begin{bmatrix} \boldsymbol{p}^t_{m,n} \\ 1 \end{bmatrix} = \boldsymbol{T}^t_d \begin{bmatrix} \boldsymbol{p}^d_{m,n} \\ 1 \end{bmatrix}. \quad (5)$$

Using the intrinsic parameters of the thermal camera, the corresponding pixel indices of the point $\boldsymbol{p}^t_{m,n}$ into the thermal image (a, b) are finally computed by inverting (3). If they are contained in the FOV of the thermal image, the corresponding depth pixel indices (m, n) are written into the mapping matrix at the indices (a, b); otherwise, they are discarded because they are outside the common view.

Phase 2: sensor fusion. The most widely used image fusion algorithms [34] combine the sources of information into a single gray scale image with suitable weights defined by the user. Here, the depth and thermal information are combined with the aim to preserve the integrity of the information contained in the two sources. The user maps the entire depth image into a specific RGB channel and the entire thermal image into a different one. Thus, the CNN in the next step defines the correct weights to the two channels of the resulting RGB image, during the training phase.

The proposed novel approach is called *RGB Mapping Approach* (RGB-MA) and consists in defining the intensities of RGB channels starting from the spatial and thermal values for every common pixel. The RGB-MA strength is that the user does not need to assign a priority to the input sources, this is indirectly done by the CNN training phase.

Fig. 6 shows five main steps to demonstrate the use of the RGB-MA. The original images acquired from the depth camera and from the thermal camera (step F) are normalized (step G) before being mapped on the green channel and the red one, respectively, as shown in step H. More in detail, the original depth sensor value, s^d, and the corresponding temperature sensor value, s^t, are normalized according to a predefined interval. Specifically, for the thermal camera, $\min_t = 30°$ C and $\max_t = 40°$ C which represent the temperature interval for human surface detection; for the depth camera, $\min_d = 0.5$ m and $\max_d = 6.0$ m which are the sensor depth ranges. At this point, the color information inserted into the specific channel of the (i, j)th pixel of the output image must be mapped to 8 bits. The $R_{i,j}$ (red) value is computed by acquiring $s^t_{i,j}$ from the thermal image, as

$$R_{i,j} = \text{round}\left(255 \frac{s^t_{i,j} - \min_t}{\max_t - \min_t}\right); \quad (6)$$

the $G_{i,j}$ (green) value is computed by acquiring $s^d_{m,n}$ from the depth image, where m and n are contained into the (i, j)th value of the mapping matrix,

$$G_{i,j} = \text{round}\left(255 \frac{s^d_{m,n} - \min_d}{\max_d - \min_d}\right); \quad (7)$$

the B (blue) value of the resulting image is always zero. A sample resulting image is shown in step I (left).

Phase 3: DT-CNN for human detection. The framework adopted for real-time human detection is YOLOv3 [35], as detailed in the previous version of this work. YOLOv3 is an off-the-shelf SoA 2D object detector pre-trained on ImageNet [36] and fine-tuned on the MS-Coco [37] data-set. It is an extremely fast and accurate object detection system, which is born to detect semantic objects of a certain class, e.g., humans, buildings and cars, in standard RGB images.

Nowadays, there are no neural networks which have been trained on combined images such as those proposed by this

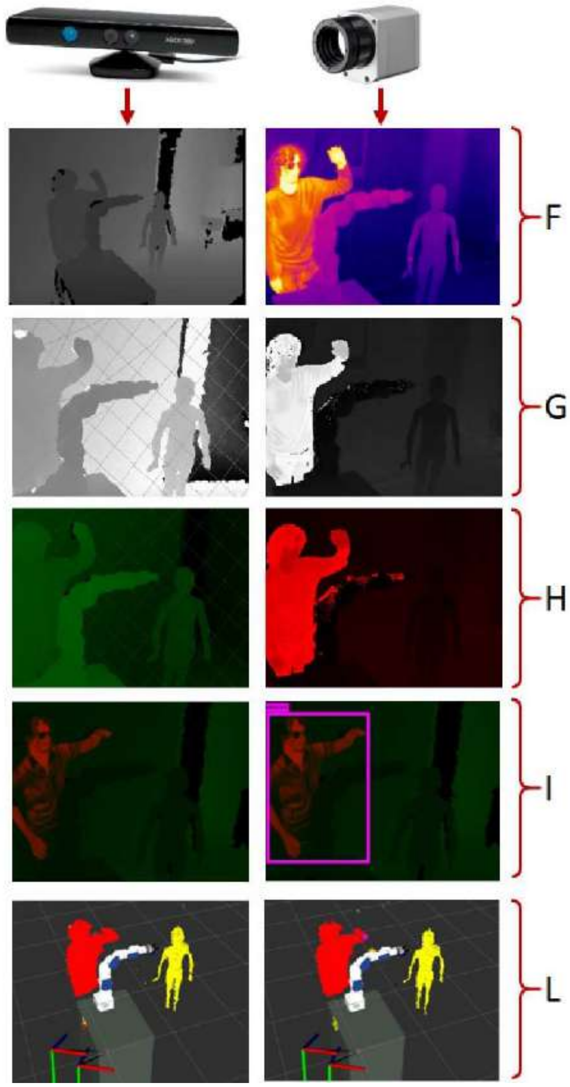

Fig. 6. Sensor fusion pipeline: the depth image and thermal image (step F) are normalized (step G) before being mapped on the green and red channels (step H). RGB-MA allows to robustly detect human workers (step I) and the pose estimation is useful to distinguish human and not-human clusters (step L).

paper, so the YOLOv3 CNN model has been re-trained. Therefore, after the definition of a *Person* class, the training data-set is built by acquiring frames from the fused D-T video stream. About 1000 frames have been manually labelled using the Yolo labeling tool and used to retrain the YOLOv3 CNN to obtain the estimated weights. After the training step, all pre-trained classes other than the *Person* class are excluded from the prediction and the CNN is executed on the real-time Depth-Thermal (DT) video stream for the human detection. A bounding box is drawn around each detected human (see step I of Fig. 6, right). Note that both the training and the prediction process need high computational cost and they are executed on a proper GPU (NVIDIA Titan V). Some details are reported in Section V.

Phase 4: human validation check. The human validation check is the last phase of the *Sensor fusion pipeline*. It collects the clusters provided by the *Segmentation pipeline* and the bounding box coordinates provided by the DT-CNN to distinguish human clusters from not-human ones.

The phase needs to transform each cluster point to the corresponding depth pixel coordinates, by inverting (4). The bounding box, originally expressed in thermal camera frame, is converted into depth camera frame through the use of the mapping matrix. If at least 70% of the cluster points are within the bounding box coordinates, the cluster is labeled as *Human* and passes the check. Step L (left) of Fig. 6 shows a clear example in which the validated human cluster is colored in red and the not-human plastic mannequin is yellow.

C. Human-Robot closest points

The human clusters provided by the sensor fusion pipeline must be processed to obtain the fuzzy inference system inputs. The clusters are converted into *RGB-D point clouds* which contain both spatial and temperature data. Then, a novel algorithm identifies the points at minimum distance through the computation of the *Human-Robot separation distance*. Finally, a *Human-Robot speed estimation* procedure is developed to compute the speed of the robot and the closest human in real-time.

1) RGB-D point clouds: The main idea in this step is that not all the points of a cluster could actually belong to the body surface. When the worker holds a tool for his manual operation, the tool is also included into the identified human cluster. Thermal information can distinguish the points representing the tool from points belonging to the human body surface inside the single cluster. This consideration led the authors to use a *thermal point cloud*: every point of the cluster is represented not only by its position but also by a RGB color depending on its own temperature. The color scale is between green (temperature value below or equal to 25° C) and red (temperature value above or equal to 40° C), as shown in step M of Fig. 7. When the point at minimum distance from the robot is identified as described in Section III-C2, the purple sphere in step N of Fig. 7 contains also its temperature value. This information is sent to the fuzzy inference system (Section IV-A), which distinguishes if the point actually belongs to the body surface or to an handheld tool. In the latter case, assuming the operator is not handling a dangerous tool, the minimum protective distance can be slightly reduced to improve the production time, because an impact of the robot with the tool is considered potentially less hazardous to the worker than a direct impact with the body surface. The effect is that the robot speed is decreased less if the point at minimum distance does not belong to the human body surface. It is important to remark that a collision is still not allowed, as required by the SSM scenario.

2) Human-Robot separation distance: The last step to compute the separation distance between the robot machine and the human worker is to identify the nearest pair of points, one belonging to the robot (P_R) and the other one belonging to the operator (P_H), that minimize the distance, i.e.,

$$P_H \in \mathcal{H}, P_R \in \mathcal{R} \mid d(P_H, P_R) \leq d(P'_H, P'_R) \quad \forall P'_H \in \mathcal{H}, P'_R \in \mathcal{R}, \tag{8}$$

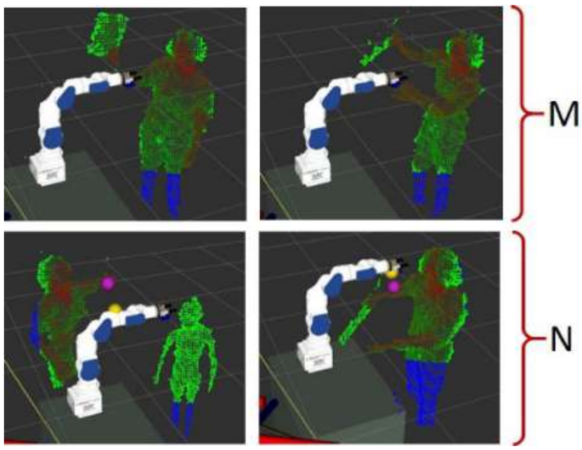

Fig. 7. RGB-D point cloud: step M shows the thermal point cloud which is obtained by associating each point to its own temperature information read by the thermal camera. The RGB color is chosen by using a color scale from green (temperature value below or equal to $25°$ C) to red (temperature value above or equal to $40°$ C). The purple sphere of step N, which represents the point at minimum distance from the robot, keeps its temperature value which is sent to the fuzzy inference system to properly ass the risk.

where $d(\cdot,\cdot)$ is the Euclidean distance between two points, $\mathcal{H}$ and $\mathcal{R}$ represent the set of all points that belong to the operator and the robot, respectively.

The whole robot is modeled through a virtual 3D model, by drawing real-time bounding spheres around each link as in [38] and [39]. Therefore, the pair of closest points can be immediately identified: the algorithm calculates the distance between all points of the human cluster point clouds and the origin of every robot frame. The robot point P_R will be on the closest virtual sphere along the line connecting the origin with P_H. Step N of Fig. 7 shows the result.

3) Human-Robot speed estimation: Intention estimation means the prediction of human motion. It consists in estimating the next position and velocity of the trajectory performed by the operator on the basis of a series of positions previously acquired.

The adopted strategy is based on a standard Linear Kalman Filter (LKF), which tries to solve the problem of estimating the state of a discrete-time process governed by the equations

$$\boldsymbol{x}_{k+1} = \begin{bmatrix} \boldsymbol{I}_3 & \Delta t \boldsymbol{I}_3 \\ \boldsymbol{O}_3 & \boldsymbol{I}_3 \end{bmatrix} \boldsymbol{x}_k + \boldsymbol{w}_k, \tag{9}$$

$$\boldsymbol{y}_k = \begin{bmatrix} \boldsymbol{I}_3 & \boldsymbol{O}_3 \end{bmatrix} \boldsymbol{x}_k + \boldsymbol{n}_k \tag{10}$$

where Δt is the sampling time, $\boldsymbol{I}_3$ and $\boldsymbol{O}_3$ are the identity and zero matrices of size 3×3, respectively; $\boldsymbol{w}_k$ and $\boldsymbol{n}_k$ are the process and measurement noises with covariance matrices $\boldsymbol{W}$ and $\boldsymbol{N}$, respectively. Finally, $\boldsymbol{x}$ is the state vector of the system, i.e., the position and the velocity of the operator $\boldsymbol{x} = \begin{bmatrix} \boldsymbol{p}_H^T & \dot{\boldsymbol{p}}_H^T \end{bmatrix}^T$, and the measured output $\boldsymbol{y}_k$ is a vector containing the coordinates of the point P_H described in Section III-C1. The covariance matrix $\boldsymbol{N}$ is experimentally estimated, while the covariance matrix $\boldsymbol{Q}$ has been chosen as

$$\boldsymbol{Q} = \begin{bmatrix} \boldsymbol{I}_3 \Delta t^2 & \boldsymbol{O}_3 \\ \boldsymbol{O}_3 & \boldsymbol{Q}_2 \end{bmatrix} \tag{11}$$

where $\boldsymbol{Q}_2$ quantifies the uncertainty on the velocity dynamics (assumed constant) of the state equations.

Based on the vector nature of the velocity, it is possible to make some considerations about the direction (trend) of the operator, that is to say, to predict in which direction he/she is travelling to.

On the other hand, the linear velocity $\dot{\boldsymbol{p}}_R$ of the point on the robot closest to the operator can be computed according to the differential kinematics equation

$$\dot{\boldsymbol{p}}_R = \boldsymbol{J}_p(\boldsymbol{q})\dot{\boldsymbol{q}}, \tag{12}$$

where $\boldsymbol{q}$ and $\dot{\boldsymbol{q}}$ are the robot joint position and velocity vectors, respectively; while, $\boldsymbol{J}_p$ is the position part of the Jacobian matrix calculated till the closest point.

As described in Section II, ISO TS 15066 suggests to compute a constant value for the minimum protective separation distance S. Unfortunately, the equation (1) does not distinguish situations during which the robot and the operator are going away from each other or they are approaching. However, the novel proposed equation (2) represents v_H as the operator speed in the direction of the moving part of the robot and v_R as the robot speed in the direction of the selected operator. Therefore, the velocity terms of (2) can be computed as

$$v_H = \left| \dot{\hat{\boldsymbol{p}}}_H^T \left(\frac{\boldsymbol{p}_R - \hat{\boldsymbol{p}}_H}{\|\boldsymbol{p}_R - \hat{\boldsymbol{p}}_H\|} \right) \right| \tag{13}$$

$$v_R = \left| \dot{\boldsymbol{p}}_R^T \left(\frac{\hat{\boldsymbol{p}}_H - \boldsymbol{p}_R}{\|\hat{\boldsymbol{p}}_H - \boldsymbol{p}_R\|} \right) \right|, \tag{14}$$

where $\hat{\boldsymbol{p}}_H$ and $\dot{\hat{\boldsymbol{p}}}_H$ are the operator position and velocity estimated by the LKF, respectively, and $\boldsymbol{p}_R$ is a vector containing the coordinates of the point P_R defined above.

IV. Safety Through Control

In literature there are a lot of proposed methodologies to reduce the robot speed in SSM scenarios, according to certain metrics. Defining these metrics is a crucial step as the main purpose is to achieve the best trade-off between the operator safety and the robotic cell productivity. An innovative fuzzy logic approach controls the robot speed by monitoring the relative distance between the robot and the human operator and by taking into account risk assessment considerations. Note that the adopted metric does not generate a discretized decision, but a continuously modulated speed scaling factor.

A. Fuzzy Inference System

To improve the production time, the minimum protective separation distance has been redefined as in (2), where α is a scaling factor which can be selected by means of considerations about hazards for the workers.

To choose the value of α, thus to define the risk, a Fuzzy Inference System (FIS) has been designed. FIS is a well-known method that provides a basis for a qualitative approach to the analysis of complex systems in which linguistic, rather than numerical, variables are employed to describe system behaviour or to encode the a priori knowledge into a computational system. Another characteristic of the fuzzy logic is

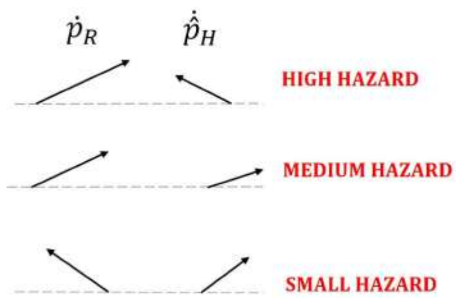

Fig. 8. Critical scenarios can be distinguished by considering both $\dot{d}$ and $\dot{\boldsymbol{p}}_R^T\dot{\hat{\boldsymbol{p}}}_H$. When the two entities are getting closer to each other and travel along opposite directions, a high hazard risk is occurring. On the contrary, when they are moving away from each other but they travel along the same direction, the risk level is intermediate. Only when they are moving away from each other, travelling along opposite directions, the risk level is low.

that each proposition of a FIS possesses a degree of truth into the interval $[0,1]$ [40], which makes it well suited to introduce smoothness in any decision process. The variable α must be classified taking into account some qualitative attributes and it may have varying levels of validity between the maximum 1 and the minimum 0. In particular, α should be close to 1 when the current situation is actually dangerous for the worker, while it should be 0 when both the robot and the human worker do not move. In addition, the velocity values are not constant as suggested by the ISO TS, but they are estimated in real time to properly adapt the value of S to the current scenario.

Hence, it is necessary to generate linguistic rules of fuzzy inference to realize a mapping of the inputs to the desired output.

The fuzzy inference process has been developed as a three-input, one-output, five-rule problem. The selected inputs are:

1) the time derivative of the distance between human and robot, i.e., $\dot{d} = \frac{d\|\hat{\boldsymbol{p}}_H - \boldsymbol{p}_R\|}{dt}$;
2) the scalar product between the robot and the human velocity vectors, i.e., $\dot{\boldsymbol{p}}_R^T\dot{\hat{\boldsymbol{p}}}_H$;
3) the temperature value of the human point at minimum distance from the robot.

The first input is useful to distinguish when the operator and the robot are getting closer ($\dot{d} < 0$) and when they are moving away from each other ($\dot{d} > 0$). The second input specifies if the travel directions of the operator and the robot are aligned ($\dot{\boldsymbol{p}}_R^T\dot{\hat{\boldsymbol{p}}}_H > 0$) or opposite ($\dot{\boldsymbol{p}}_R^T\dot{\hat{\boldsymbol{p}}}_H < 0$). The third input relaxes the speed monitoring if the point closest to the robot belongs to not-human surface, providing reduction of the production time. Note that the scalar product (second input) represents a complementary information to the time derivative (first input) to distinguish situations shown in Fig. 8.

The fuzzy system consists of five rules (see Table I).

TABLE I
FUZZY RULES: [S] SMALL, [M] MEDIUM, [H] HIGH, [N] NEGATIVE, [P] POSITIVE, [YES] HUMAN TEMPERATURE, [NO] NOT-HUMAN TEMPERATURE, [$\sim$] ANY.

antecedent			consequent
$\dot{d}$	$\dot{\boldsymbol{p}}_R^T\dot{\hat{\boldsymbol{p}}}_H$	human	α
N	$\sim$	$\sim$	H
P	N	$\sim$	S
P	P	$\sim$	M
$\sim$	$\sim$	Yes	H
$\sim$	$\sim$	No	S

Two membership functions have been selected to represent positive (P) and negative (N) values, a Z-shape and a S-shape, respectively, as well as, to represent human (Yes) and not-human (No) temperature ranges equal to those used for the construction of the thermal point cloud. The defuzzification is performed according to the centroid method.

Note that the output value, α, is generated by analyzing different possible risk situations, corresponding to the three fuzzy sets high (H), medium (M) and small (S), with the twofold aim of avoiding any collisions between human body surface and robot, and being in line with the current ISO/TS 15066.

B. Trajectory scaling

A standard SSM method usually sacrifices the production time because the minimum protective distance S is constant. On the contrary, the proposed strategy implements an algorithm to adapt the minimum protective distance S to the actual operating conditions and, in turn, changing the robot speed.

A typical pre-programmed task, $\mathcal{T}$, is composed by N positions $\tilde{q}_i$, associated to velocities $\dot{\tilde{q}}_i$, accelerations $\ddot{\tilde{q}}_i$ and time instants $\tilde{t}_i$ with $i = 1,\ldots,N$. In the control interface of the robot used in the experiments presented in Section V, the pre-programmed joint positions have to be interpolated according to the sampling time T_c. Nevertheless, the strategy described below simply translates into the computation of a scaling factor for industrial robots that allows the user to change the speed override in real time. In this work a quintic interpolation is assumed, i.e., the planned interpolated trajectory is

$$\tilde{q}_h = p_5(t_h;\, \mathcal{T}) \tag{15}$$

$$\dot{\tilde{q}}_h = p_4(t_h;\, \mathcal{T}) \tag{16}$$

$$t_{h+1} = t_h + T_c, \tag{17}$$

where t_h is the h-th discrete time instant, p_4 is the derivative of the polynomial p_5, $\tilde{q}_h$ and $\dot{\tilde{q}}_h$ are the *planned* joint position and velocity at time t_h, respectively.

The robot speed is modulated by scaling the trajectory time with a *safety scale factor* k, which can assume values in the interval $[0,1]$. The mathematical expression of the curve relating d with k is a piecewise-defined function whose graph is shown in Fig. 9. More in detail, when $d < S$, k is 0 and the robot stops as required by the SSM constraint. Otherwise, when $d > \nu S$, where $\nu > 1$ is a design parameter needed to guarantee continuity of k, the robot can move at full speed to improve the production time, i.e., νS represents the warning

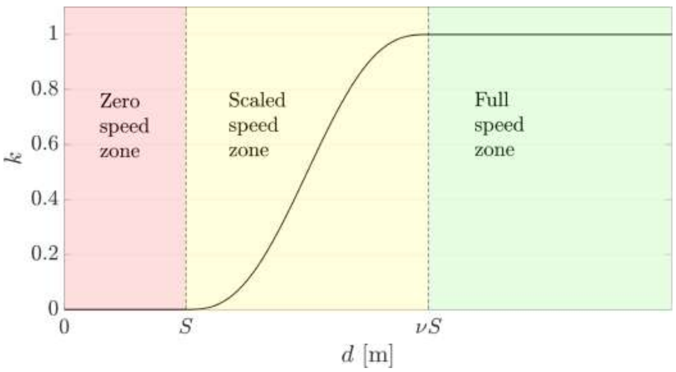

Fig. 9. Relation between d and k; S is the minimum separation distance computed in real time as in (2).

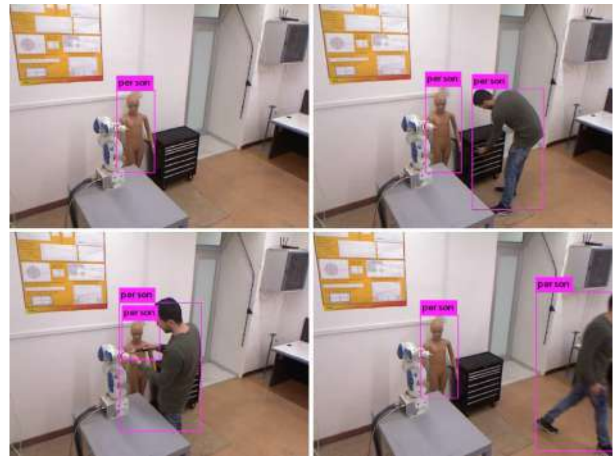

Fig. 10. Standard Yolo CNN for human detection on RGB images: a plastic mannequin which has a shape similar to the human one, is wrongly classified as *Human*.

distance. Finally, when d assumes a value between S and νS a polynomial of order at least 3 should be used to avoid acceleration discontinuities (see (20)).

Practically, the trajectory is scaled computing (15) using a scaled time τ_h, i.e.,

$$q_h = p_5(\tau_h; \mathcal{T}) \quad \tau_{h+1} = \tau_h + kT_c, \tag{18}$$

where q_h is the actual joint command at time t_h. Obviously, the joint command q_h, as well as the scaled time τ_h, are generated with sampling time T_c.

This approach effectively scales the joints velocities. In fact, using (18), it is

$$\dot{\tau} \approx \frac{\tau_{h+1} - \tau_h}{T_s} = k. \tag{19}$$

By time differentiating (18), (20) demonstrates that the velocity is scaled by the *safety factor* k,

$$\dot{q}_h = p_4(\tau_h; \mathcal{T})k. \tag{20}$$

This approach guarantees that the task $\mathcal{T}$ remains the same in position, but, simultaneously, the resulting velocity is scaled according to k. Note that, in case the industrial control interface of the robot allows the user to change online the speed override of any motion instruction, it is sufficient to set a speed override equal to the factor k. Section V-C reports an experiment where an industrial robot is controlled in this way.

V. Experimental results

To assess the practical relevance of the proposed method, this section shows some results. The experiments are executed on two different setups. The first lab-scale setup includes a Yaskawa MOTOMAN SIA5F industrial robot performing an assembly-like task, i.e., a cyclic pre-programmed trajectory. The application is based on a ROS industrial architecture and the external PC communicates, through an Ethernet cable at 50Hz, the reference joint positions to the robot controller, equipped with the MotoPlus SDK [41]. The second full-scale setup includes a robotic cell designed to perform the cooperative assembly of aeronautical panels composed of hybrid (composite-metal) structural parts [42]. The robot is a Fanuc M-20iA-35M whose controller allows the user to set on line a register with the desired value of the speed override. This value is set by the external PC running the speed scaling algorithm that computes the speed override k. The external PC communicates with the cell Human Machine Interface (HMI) module via TCP-IP with a frequency at which the scaling algorithm runs, i.e., 30 Hz. Finally, the HMI updates the register of the robot controller in real time via EtherCAT Automation Protocol (EAP).

A. Human detection

The performance of the novel CNN will be compared with standard pre-trained RGB-CNNs as well as with single-source CNNs, i.e., trained on depth or thermal images only.

1) Standard RGB-CNN: The first experiments are conducted by using standard RGB-CNNs. Unfortunately, these pre-trained networks always confuse a plastic mannequin or other objects with shape similar to humans (see Fig. 10) and classify them into the *Human Class*. This type of result is clearly unusable in industrial environments as it would produce too many false positives. Consequently, any speed scaling algorithm that has such a wrong classification input would involve unnecessary robot stops, therefore a useless dead time.

2) Single-source CNNs Vs DT-CNN: To evaluate the performance of the novel DT-CNN, two single-source CNNs are trained at the same time. The first one processes only depth images (D-CNN) and the second one processes only thermal images (T-CNN). The test is useful to better understand the need of the sensor fusion approach to achieve robust and reliable detection results. Note that the three networks have been trained and tested with the same input data-set to correctly compare the results.

The training data-set is composed of manually labeled images. Yolo requires that each image is supported by a text file which contains the information about the category of the labeled objects and the coordinate values of the drown bounding boxes. The images are saved starting from a recorded video stream and an available Python program automatically saves the frames at a chosen rate. *YOLO-Annotation-Tool* software is used to manually label the images and generate

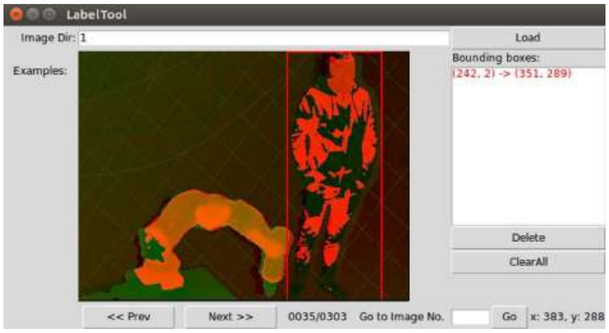

Fig. 11. *YOLO-Annotation-Tool* software supports manual labelling step: the programmer draws the bounding box around the human operators present into the image and labels them as belonging to the *Human Class*.

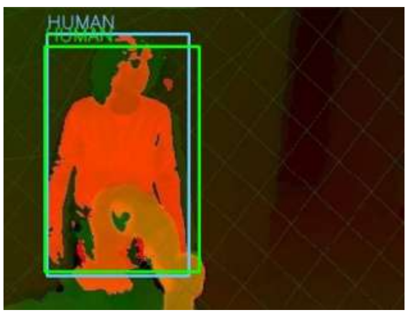

Fig. 12. mAP evaluation: comparison between the area returned from the prediction (green box) and the ground truth (blue box).

the corresponding text files, as shown in Fig. 11. Note that the training phase needed about 1000 training samples to achieve the presented performance. This requirement represents another great advantage of using the proposed approach, if compared with RGB pre-trained CNNs which need tens of thousands of images to be trained.

The metrics adopted to measure the accuracy of the novel CNNs are reported in Table II. The first metric is the *Mean Average Precision (mAP)* [43] which determines the accuracy of finding the coordinates of the bounding box in which the object is predicted to be. Computing the mAP consists in comparing the area returned from the prediction (green box) and the ground truth (blue box), as shown in Fig. 12. Since the mAP value does not consider false positives and false negatives, the percentage of erroneous detection has been manually estimated. Table II reports all the results. The DT-CNN mAP is almost similar to the single-source CNNs and represents a good value of prediction accuracy based only on true positives. The most clear advantage of using DT-CNN is about the percentage of false positives, which is considerably lower than the other networks. The proposed approach is able to correctly distinguish only human operators thanks to the additional temperature information. This is a remarkable result which guarantees that any robot speed scaling algorithm can robustly impose the nominal speed by assuring worker safety and maximizing the production time in industrial environments. The high percentage of false positives of single-source approaches is to be found in cases where hot objects (T-CNN) or objects with shapes comparable to human ones (D-CNN) can be confused with humans, as shown in Fig. 13. For completeness, the percentage of false negatives remains low for all three neural networks. Part 1 of the accompanying video of the experiment regarding the proposed DT-CNN clearly shows the differences with the single-source CNNs.

TABLE II
CNNs Testing Results

CNN	mAP %	False Positives %	False Negatives %
D-CNN	65.09	36.87	17.53
T-CNN	62.76	64.35	4.37
DT-CNN	57.54	2.47	11.85

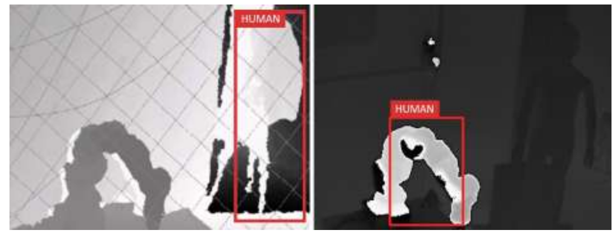

Fig. 13. Two cases of human false positives: a coat rack labeled as human in the D-CNN approach (left); a hot moving robot labeled as human in the T-CNN approach (right).

B. Lab-scale experiment

This section shows a complete example of a collaborative task to highlight all the features of the proposed methods. All the algorithms, except the DT-CNN, run on a standard desktop PC running Ubuntu 16.04 LTS with an Intel Core i7-8700K CPU at 3.70GHz, 12GB of RAM and an nVidia GeForce GT 730 GPU with 12GB of memory. The Yolo prediction process runs on a PC running Ubuntu 18.04.2 LTS with an Intel Core i9-7980XE CPU at 2.60GHz, 18 GB of RAM and an nVidia Titan V GPU with 12GB of memory.

1) Task description: The scene simulates a robot executing a pre-planned path at a given nominal speed, and a human operator who enters the collaborative workspace to perform some inspection checks. The operator handles different objects, e.g., a bubble level, a notepad, close to the robot, at different distances and approaching it randomly. Fig. 14 shows the main snapshots of the task execution which demonstrate that, by reading the temperature of the point belonging to the human cluster which is the closest to the robot, the fuzzy inference system (Fig. 15) marks it as belonging to an object manipulated by the operator or actually belonging to the human body surface. More in detail, at $t = 12\,\mathrm{s}$ the operator puts a bubble level on the desk, then he closes the toolbox at $t = 18\,\mathrm{s}$ and he takes a notepad to write some inspection measurements at $t = 26\,\mathrm{s}$. During these phases, the point closest to the robot belongs to the handled tools, thus the robot may proceed at a slightly higher speed. At the end of the experiment, the worker puts the tools in place ($t = 41\,\mathrm{s}$) and leaves the collaborative zone ($t = 45\,\mathrm{s}$), thus his body surface is directly the most exposed to the robot motions, i.e., the fuzzy system reduces the robot speed to ensure the worker safety. Note that the variations of the separation distance $S(t)$ are limited due to the low value of the nominal (when $k = 1$)

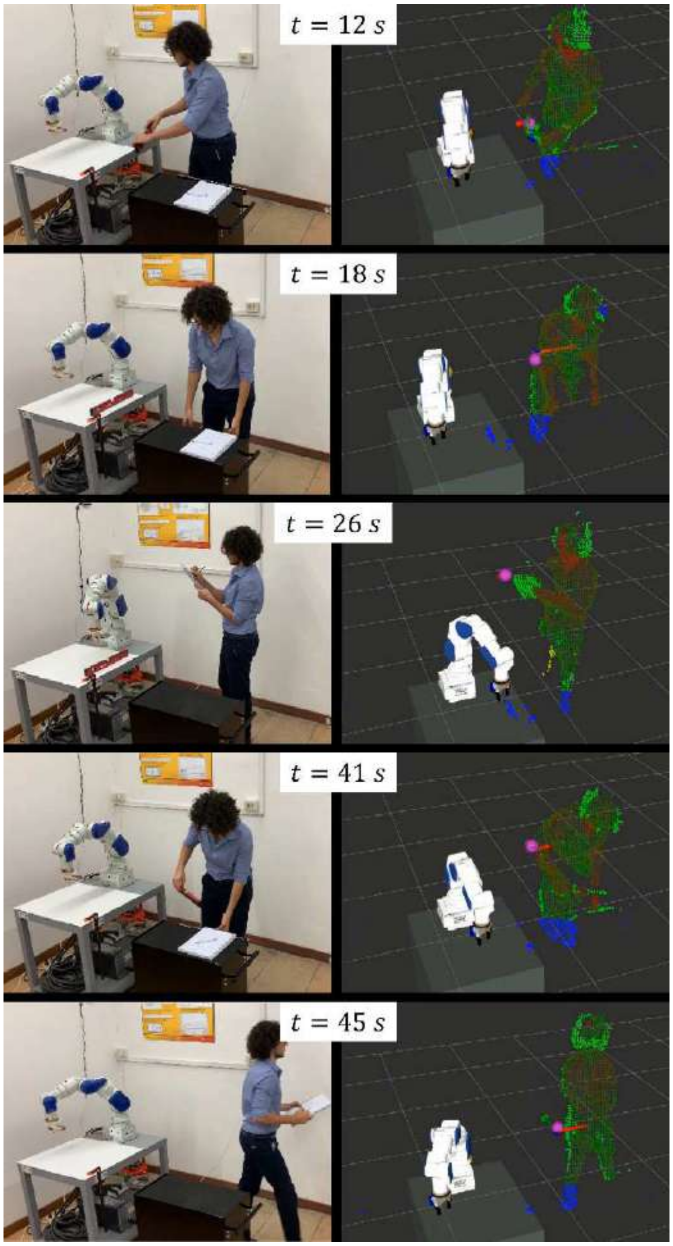

Fig. 14. Snapshots of the task execution of the lab-scale experiment: while the robot is following its pre-programmed path, at $t = 12$ s the operator enters its workspace and puts a bubble level on the desk, then he closes the toolbox at $t = 18$ s and he takes a notepad to write some inspection measurements at $t = 26$ s. At the end of the experiment, the worker puts the tools in place ($t = 41$ s) and leaves the collaborative zone ($t = 45$ s).

robot speed and the constant terms in eq. (2), which prevent its further reduction.

2) Task results: Results are shown in Fig. 15 and in Part 2 of the accompanying video of the experiment.

The bottom graph represents the robot speed scaling performance. More in detail, at about 10 s the operator enters the collaborative workspace and the system starts to measure the separation distance d (green line). When d goes below the warning distance νS, with $\nu = 2$, (red line) at about 11 s, the trajectory scaling factor k (magenta line) becomes lower than 1 and the robot reduces its velocity without changing its path. During some intervals of the collaborative phase, d goes below the minimum protective distance S, thus k becomes 0 and the robot stops.

The top graph compares the α_{old} values (green line) obtained through the preliminary fuzzy inference system proposed in [3], and the α values computed with the new algorithm (indicated with α_{new} in the figure (blue line)). The difference is due to the use of the new input, i.e., the temperature value, T (red line), of the point at minimum distance from the robot, which belongs to the human cluster.

Until 12 s the operator is inside the collaborative workspace and manipulates the bubble level to perform his task. After that, at about 18 s, he closes the toolbox, thus his body part becomes close to the robot: the elbow, the right arm, the hand, the shoulder are most exposed to risk in the direction of the robot. Therefore, the mean value of the temperature of these points is about $35°$ C, that the fuzzy inference system associates to the human surface. In this first phase, the α_{new} signal follows the α_{old} one without major changes.

The most interesting phase is the second one. At about 26 s, the operator takes notes on a notepad to perform some inspection checks. From this moment on, the notepad is the object closest to the robot. Note that it clearly belongs to the human cluster, even if it is not part of the operator body surface. The temperature value can be read to realize this difference. Indeed, during this phase the point at minimum distance has got a mean value of about $28°$ C, which does not represent a human surface temperature value. The proposed fuzzy inference approach adopts this input also for the α_{new} computation, which is lower than the α_{old} estimation because the risk is considered lower. In other words, during similar situations, the minimum protective distance S can be reduced to allow the robot to move faster. The last phase, at about 38 s is similar to the first one, when the closest point of the human cluster belongs to the human surface.

C. Full-scale experiment

A similar experiment has been performed on the full-scale robotic cell reported in Fig. 16, where a robot is performing a quality inspection task and the worker is dismantling a metal part after its drilling for deburring purposes. The results reported in Fig. 17, where the minimum protective distance is computed according to the proposed method in eq. (2), show that the robot moves at scaled speed when $S < d < \nu S$ and only for a few moments it moves at zero speed. In fact, the red zone at about 80 s highlights the time interval when the robot is completely stopped since the separation distance d is below S. Fig. 18 shows what would have happened if the minimum protective distance S had been a constant value calculated according to (1): the duration of robot stops is significantly larger, with a clear drawback in terms of robot work cycle time. Note that the robot moves at its nominal speed only when the human worker is not inside the collaborative area, i.e., the blue line representing the separation distance d is absent.

VI. Conclusion

The paper contributed with two methods to the problems that arise when using collaborative robots in industrial ap-

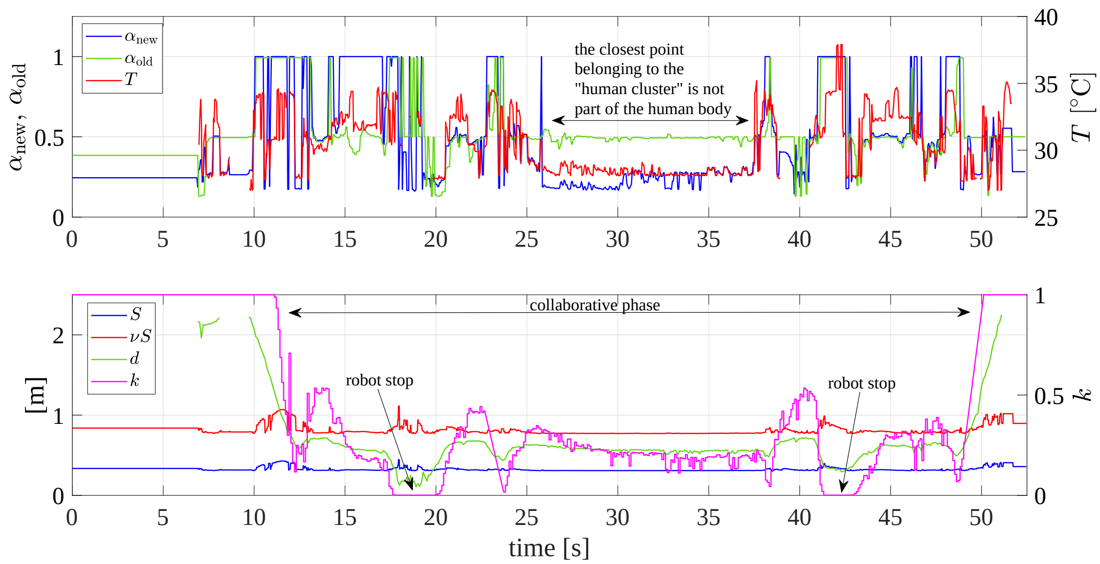

Fig. 15. Experiment: an operator enters the shared workspace to make some inspection checks while the robot is moving. The top plot shows the comparison between α_{old} values (green line) obtained through the preliminary fuzzy inference system of [3] and α values obtained with the new fuzzy system (indicated with α_{new} (blue line)) which considers the temperature value T (red line – right axis) of the human point closest to the robot. The bottom plot shows the estimated separation distance robot-operator d, the protective distances proposed by the paper (S and νS) and the scaling factor k (magenta line – right axis).

Fig. 16. The LABOR robotic cell during a cooperative assembly operation: the robot is performing a quality inspection task, while the human worker is dismantling a metal part for deburring after hole drilling.

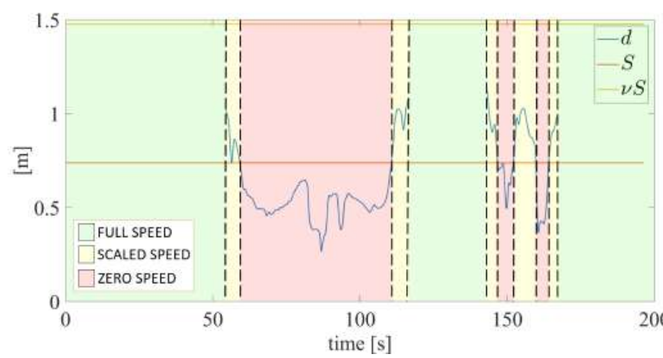

Fig. 18. Standard method: S is a constant value computed as in (1). The plot shows the comparison between the separation distance d (blue line) and the fixed range [S, νS]. The zero speed zones are very large, causing considerable increase of the production time. The robot moves at full speed only when the human operator is outside the collaborative area (green zone).

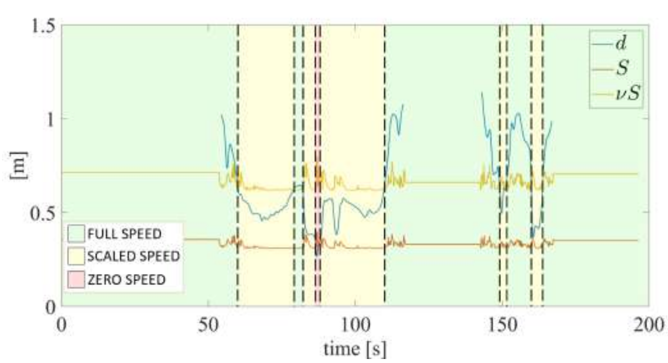

Fig. 17. Proposed method: $S(t)$ is computed online as in (2). The plot shows the comparison between the separation distance d (blue line) and the time-variant range [S, νS]. The robot mostly moves at full or scaled speed, while the complete stop area is minimal.

plications. Specifically, the STP proposes a new multimodal perception system that fuses depth and thermal images for reliable human detection and tracking in a robotic workcell. The new RGB mapping approach can be generally applied to any other perception system that intends to use thermal and RGB cameras for obtaining a single image. The algorithm, besides the separation distance between the robot and the human, computes a thermal point cloud of the detected humans, which helps to distinguish body parts from handheld tools. The STC method proposes a fuzzy inference system able to compute dynamically the minimum protective distance according to a risk analysis based on the perception data. A simple speed scaling algorithm is used to modulate the robot velocity in each situation preserving safety of the human operators in the workcell. The combination of the two methods allowed achieving a high productivity of the workcell by minimizing robot stops while ensuring safety owing to the additional thermal information. An experiment on a full-scale robotic workcell for cooperative assembly of aircraft panels has also been presented. The algorithms can easily be extended to the multirobot case and already work in case of multiple humans. Even though the paper proposes an approach limited to the case of workspace sharing without any physical contact of the robot with the human, some of the results can be extended to this case also. For example, the FIS used for the risk assessment could be designed to assess the risk of the physical human-robot contact based on the robot velocity and configuration, as well as on the location of the contact detected by the human monitoring system able to capture the different body parts.

Acknowledgement

This work has received funding from the Clean Sky Horizon 2020 Programme under the LABOR project, GA n. 785419, with Leonardo S.p.A. as Topic Manager.

References

[1] The LABOR project, "https://www.labor-project.eu/," 2019.

[2] L. Roveda, S. Ghidoni, S. Cotecchia, E. Pagello, and N. Pedrocchi, "Eureca h2020 cleansky 2: a multi-robot framework to enhance the fourth industrial revolution in the aerospace industry," in *2017 IEEE Int. Conf. on Robotics and Automation - workshop IC3 Industry of the future: Collaborative, Connected, Cognitive. Novel approaches stemming from factory of the future & industry 4.0 initiatives*, 2017.

[3] A. Campomaggiore., M. Costanzo., G. Lettera., and C. Natale., "A fuzzy inference approach to control robot speed in human-robot shared workspaces," in *Proceedings of the 16th International Conference on Informatics in Control, Automation and Robotics - Volume 2: ICINCO,*, INSTICC. Prague, CZ: SciTePress, July 2019, pp. 78–87.

[4] M. Costanzo, G. De Maria, G. Lettera, C. Natale, and D. Perrone, "A multimodal perception system for detection of human operators in robotic work cells," in *2019 IEEE International Conference on Systems, Man and Cybernetics (SMC)*, Bari, I, Oct 2019, pp. 692–699.

[5] "Robots and robotic devices - Safety requirements for industrial robots. Part 1: Robots." International Organization for Standardization, Technical report, 2011.

[6] "Robots and robotic devices - Safety requirements for industrial robots. Part 2: Robot system and integration." International Organization for Standardization, Technical report, 2011.

[7] "Robots and robotic devices - collaborative robots." International Organization for Standardization, Technical report, 2016.

[8] J. Heinzmann and A. Zelinsky, "Quantitative safety guarantees for physical human-robot interaction," *The International Journal of Robotics Research*, vol. 22, no. 7-8, pp. 479–504, July 2003.

[9] S. Haddadin, A. Albu-Schaffer, A. D. Luca, and G. Hirzinger, "Collision detection and reaction: A contribution to safe physical human-robot interaction," in *2008 IEEE/RSJ International Conference on Intelligent Robots and Systems*. IEEE, Sep 2008.

[10] S. Haddadin, A. Albu-Schaffer, M. Frommberger, J. Rossmann, and G. Hirzinger, "The dlr crash report: towards a standard crash-testing protocol for robot safety - part II: Discussions," in *2009 IEEE International Conference on Robotics and Automation*. IEEE, 2009, pp. 280–287.

[11] A. Cirillo, F. Ficuciello, C. Natale, S. Pirozzi, and L. Villani, "A conformable force/tactile skin for physical human–robot interaction," *IEEE Robotics and Automation Letters*, vol. 1, no. 1, pp. 41–48, January 2016.

[12] M. Geravand, F. Flacco, and A. D. Luca, "Human-robot physical interaction and collaboration using an industrial robot with a closed control architecture," in *2013 IEEE International Conference on Robotics and Automation*. IEEE, may 2013.

[13] C. A. Cifuentes, A. Frizera, R. Carelli, and T. Bastos, "Humanrobot interaction based on wearable imu sensor and laser range finder," *Robotics and Autonomous Systems*, vol. 62, no. 10, pp. 1425 – 1439, 2014.

[14] F. Flacco, T. Kroger, A. D. Luca, and O. Khatib, "A depth space approach to human-robot collision avoidance," in *2012 IEEE International Conference on Robotics and Automation*. IEEE, May 2012.

[15] N. Arora, D. Martins, D. Ruggerio, E. Tousimis, A. J. Swistel, M. P. Osborne, and R. M. Simmons, "Effectiveness of a noninvasive digital infrared thermal imaging system in the detection of breast cancer," *The American Journal of Surgery*, vol. 196, no. 4, pp. 523–526, oct 2008.

[16] M. Vollmer and K.-P. Mllmann, *Infrared Thermal Imaging*. Wiley-VCH Verlag GmbH & Co. KGaA, dec 2017.

[17] H. Kaplan, *Practical Applications of Infrared Thermal Sensing and Imaging Equipment.* SPIE Publications, 2007.

[18] S. Savazzi, V. Rampa, and F. Vicentini, "Device-free human sensing and localization in collaborative humanrobot workspaces: A case study," *IEEE Sensors Journal*, vol. 16, no. 5, pp. 1253–1264, 2015.

[19] S. Kianoush, S. Savazzi, F. Vicentini, V. Rampa, and M. Giussani, "Device-free rf human body fall detection and localization in industrial workplaces," *IEEE Internet of Things Journal*, vol. 14, no. 2, pp. 351–362, 2016.

[20] P. Zhang, P. Jin, G. Du, and X. Liu, "Ensuring safety in human-robot coexisting environment based on two-level protection," *Industrial Robot: An International Journal*, vol. 43, no. 3, pp. 264–273, May 2016.

[21] M. Lippi and A. Marino, "Safety in human-multi robot collaborative scenarios: a trajectory scaling approach," *IFAC-PapersOnLine*, vol. 51, no. 22, pp. 190–196, 2018.

[22] F. Vicentini, N. Pedrocchi, M. Beschi, M. Giussani, N. Iannacci, P. Magnoni, S. Pellegrinelli, L. Roveda, E. Villagrossi, M. Askarpour, I. Maurtua, A. Tellaeche, F. Becchi, G. Stellin, and G. Fogliazza, *PIROS: Cooperative, Safe and Reconfigurable Robotic Companion for CNC Pallets Load/Unload Stations*. Cham: Springer International Publishing, 2020, pp. 57–96.

[23] M. Safeea, N. Mendes, and P. Neto, "Minimum distance calculation for safe human robot interaction," *Procedia Manufacturing*, vol. 11, pp. 99–106, 2017.

[24] L. Bascetta, G. Ferretti, P. Rocco, H. Ardo, H. Bruyninckx, E. Demeester, and E. D. Lello, "Towards safe human-robot interaction in robotic cells: An approach based on visual tracking and intention estimation," in *2011 IEEE/RSJ International Conference on Intelligent Robots and Systems*. IEEE, September 2011.

[25] A. M. Z. Matteo Parigi Polverini and P. Rocco, "A computationally efficient safety assessment for collaborative robotics applications," *Robotics and Computer-Integrated Manufacturing*, vol. 46, pp. 25 – 37, 2017.

[26] J. T. C. Tan and T. Arai, "Triple stereo vision system for safety monitoring of human-robot collaboration in cellular manufacturing," in *2011 IEEE International Symposium on Assembly and Manufacturing (ISAM)*, May 2011, pp. 1–6.

[27] James Bowman and Patrick Mihelich, "Camera calibration tool, http://wiki.ros.org/camera_calibration."

[28] P. Torr and D. Murray, "The development and comparison of robust methods for estimating the fundamental matrix," *International Journal of Computer Vision*, vol. 24, no. 3, pp. 271–300, September 1997. [Online]. Available: https://doi.org/10.1023/A:1007927408552

[29] M. A. Fischler and R. C. Bolles, "Random sample consensus: a paradigm for model fitting with applications to image analysis and automated cartography," *Communications of the ACM*, vol. 24, no. 6, pp. 381–395, June 1981.

[30] R. B. Rusu and S. Cousins, "3d is here: Point cloud library (PCL)," in *IEEE International Conference on Robotics and Automation*. IEEE, May 2011.

[31] T. Luhmann, J. Piechel, and T. Roelfs, "Geometric calibration of thermographic cameras," in *Thermal Infrared Remote Sensing*. Springer Netherlands, 2013, pp. 27–42.

[32] J. Rangel and S. Soldan, "3d thermal imaging: Fusion of thermography and depth cameras," in *Proceedings of the 2014 International Conference on Quantitative InfraRed Thermography*. QIRT Council, 2014.

[33] N. Blodow, "Realtime urdf filter," 2012.

[34] B. Yang, Z. liang Jing, and H. tao Zhao, "Review of pixel-level image fusion," *Journal of Shanghai Jiaotong University (Science)*, vol. 15, no. 1, pp. 6–12, February 2010.

[35] J. Redmon and A. Farhadi, "Yolov3: An incremental improvement," *CoRR*, vol. abs/1804.02767, 2018. [Online]. Available: http://arxiv.org/abs/1804.02767

[36] J. Deng, W. Dong, R. Socher, L.-J. Li, K. Li, and L. Fei-Fei, "ImageNet: A Large-Scale Hierarchical Image Database," in *CVPR09*, 2009.

[37] T.-Y. Lin, M. Maire, S. Belongie, J. Hays, P. Perona, D. Ramanan, P. Dollár, and C. L. Zitnick, "Microsoft COCO: Common objects in context," in *Computer Vision – ECCV 2014*. Springer International Publishing, 2014, pp. 740–755.

[38] S. I. Choi and B. K. Kim, "Obstacle avoidance control for redundant manipulators using collidability measure," in *Proceedings 1999 IEEE/RSJ International Conference on Intelligent Robots and Systems. Human and Environment Friendly Robots with High Intelligence and Emotional Quotients (Cat. No.99CH36289)*. IEEE, 1999.

[39] P. Bosscher and D. Hedman, "Real-time collision avoidance algorithm for robotic manipulators," in *2009 IEEE International Conference on Technologies for Practical Robot Applications*. IEEE, November 2009.

[40] T. J. Ross, *Fuzzy Logic with Engineering Applications*. John Wiley & Sons, Ltd, January 2010.

[41] Yaskawa, "MotoPlus SDK." [Online]. Available: https://www.motoman.com/en-us/products/software/development/motoplus-sdk

[42] M. Caterino, P. Chiacchio, C. Cristalli, M. Fera, G. Lettera, C. Natale, and M. Nisi, "Robotized assembly and inspection of composite fuselage panels: the labor project approach," in *Proceedings of the 10th EASN Virtual Conference*. IOP Publishing Ltd., Sep. 2020.

[43] W. Su, Y. Yuan, and M. Zhu, "A relationship between the average precision and the area under the roc curve," in *Proceedings of the 2015 International Conference on The Theory of Information Retrieval*, ser. ICTIR '15. New York, NY, USA: ACM, 2015, pp. 349–352.

Marco Costanzo graduated in Information Engineering on 2017 at the Università degli Studi della Campania Luigi Vanvitelli where he is currently a PhD student. His research interests range from robotic manipulation based on force/tactile sensing to multi-modal sensing for safe human-robot interaction.

Giuseppe De Maria since 1994 is full professor of System Theory and Automatic Control at the Department of Engineering of the Università degli Studi della Campania Luigi Vanvitelli. His research interests include control of aerospace and aeronautical systems, active noise and vibration control of flexible structures, robust control, control of mechanical systems, industrial and advanced robotics. Now his research interests are focused on the development of force and tactile sensors for grasping and in hand manipulation in professional service robotics.

Gaetano Lettera was born in Aversa, Italy, in 1993. He received the B.Sc. and the M. Sc. degree in Computer Engineering from the Università degli Studi della Campania Luigi Vanvitelli, Aversa, in 2015 and 2017, respectively. His research interests range from object recognition and localization, trajectory planning, robotic manipulation to multi-modal sensing for human-robot collaboration.

Ciro Natale is currently a Full Professor of Robotics and Mechatronics with the Università degli Studi della Campania Luigi Vanvitelli, Italy. He has authored or co-authored more than 120 journal and conference papers, including two monographs. His research interests include modeling and control of industrial manipulators, force and visual control, manipulation control based on force-tactile sensing, as well safe human-robot interaction. He served as Associate Editor for IEEE journals and he is Associate Editor of Automatica.

Manufacturing Rev. **8**, 8 (2021)

https://doi.org/10.1051/mfreview/2021007

Manufacturing Review
Available online at:
https://mfr.edp-open.org

RESEARCH ARTICLE

OPEN ACCESS

Planning of efficient trajectories in robotized assembly of aerostructures exploiting kinematic redundancy

Federica Storiale*, Enrico Ferrentino**, and Pasquale Chiacchio***

Department of Computer Engineering, Electrical Engineering and Applied Mathematics (DIEM), University of Salerno, Fisciano, SA 84084, Italy

Received: 30 September 2020 / Accepted: 20 February 2021

Abstract. Aerospace production volumes have increased over time and robotic solutions have been progressively introduced in the aeronautic assembly lines to achieve high-quality standards, high production rates, flexibility and cost reduction. Robotic workcells are sometimes characterized by robots mounted on slides to increase the robot workspace. The slide introduces an additional degree of freedom, making the system kinematically redundant, but this feature is rarely used to enhance performances. The paper proposes a new concept in trajectory planning, that exploits the redundancy to satisfy additional requirements. A dynamic programming technique is adopted, which computes optimized trajectories, minimizing or maximizing the performance indices of interest. The use case is defined on the LABOR (Lean robotized AssemBly and cOntrol of composite aeRostructures) project which adopts two cooperating six-axis robots mounted on linear axes to perform assembly operations on fuselage panels. Considering the needs of this workcell, unnecessary robot movements are minimized to increase safety, the mechanical stiffness is maximized to increase stability during the drilling operations, collisions are avoided, while joint limits and the available planning time are respected. Experiments are performed in a simulation environment, where the optimal trajectories are executed, highlighting the resulting performances and improvements with respect to non-optimized solutions.

1 Introduction

Nowadays, the huge volumes in manufacturing industries have brought to an increment in the employment of autonomous systems performing the hardest and repeatable operations, in order to increase the overall efficiency of the production lines. As a consequence, robotized solutions are frequently adopted to obtain a higher level of automation, while guaranteeing high quality results. On the one hand, the aerospace sector, as highlighted in [1], is the least automated because of the large and complex systems to handle and the wide variety of activities to be carried out during the production phases, including drilling, sealing, fastening, inspection, coating, painting and material handling [2]. On the other hand, even in this context, in agreement with the global trend, production volumes have increased in the last years, requiring automatic solutions where robots perform such operations.

Typically, robotized solutions in large industrial plants have the common characteristic of employing robots mounted on slides, i.e. linear axes, to increase their workspace and allow them to cover wide areas. These linear axes introduce additional degrees of freedom that yield kinematic redundancy, i.e. there is an infinite number of joint configurations corresponding to the same pose of the end-effector.

Kinematic redundancy is also the key in applications involving mobile manipulators [3], that are versatile systems, capable of performing different kinds of tasks. Their flexibility comes with an increased complexity due, among other things, to the capability of handling the kinematic redundancy efficiently. This characteristic has been the main impediment to the spreading of mobile robots in the aerospace manufacturing lines. In fact, in order to simplify the setup of the workcell, the existing solutions foresee to neglect the extra degrees of freedom during trajectory planning, using them exclusively to increase the workspace of the robots.

Existing robotized solutions in aerostructures manufacturing are typically complex, heavy, rigid and expensive, since high-payload robots are adopted and the demanding requirements of the assembly operations yield an increase of cost. Especially in the case of regional aircraft

* e-mail: fstoriale@unisa.it
** e-mail: eferrentino@unisa.it
*** e-mail: pchiacchio@unisa.it

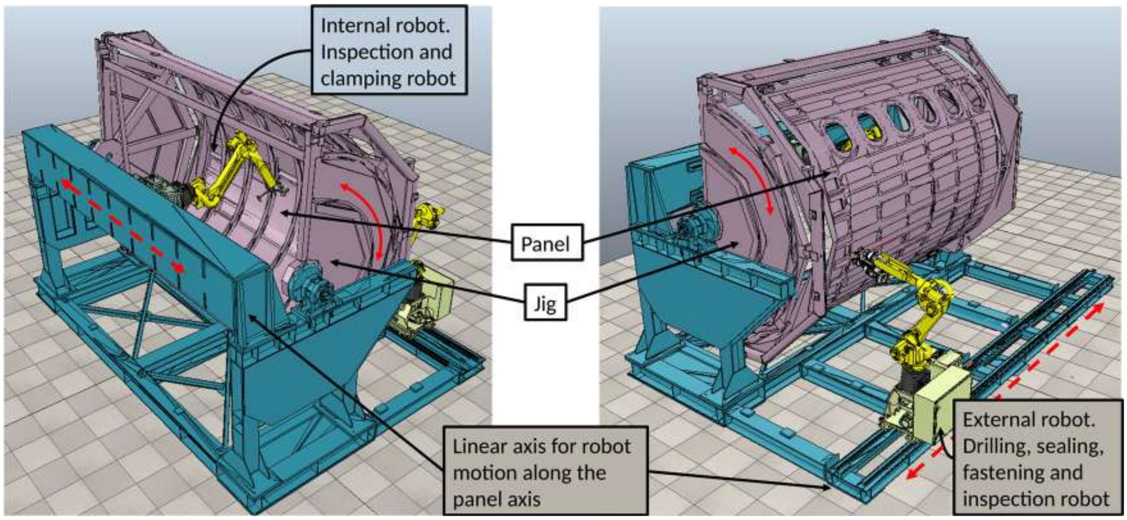

Fig. 1. LABOR cell represented in the CoppeliaSim simulator.

industry, assembly of fuselage aerostructures is largely a manual process because of the need for high accuracy, which is not achievable by the common industrial robots. In fact, this is typically guaranteed through external metrology systems that, however, increase the overall cost of the system and reduce its flexibility.

Furthermore, a complete assembly cycle requires to perform the mentioned tasks on thousands of holes per aircraft, thus tight time constraints are usually imposed on each single operation to keep the production rates high. Also, since in most cases the human intervention is still required, the automated workcell must be adapted for human cooperation [1,4,5]. In particular, a higher degree of safety is necessary, avoiding dangerous robot movements and configurations.

This paper concerns the employment of small and medium sized high-precision robots, whose workspace is augmented through the introduction of extra degrees of freedom. They guarantee higher flexibility and speed, naturally contain costs and can be programmed to increase production quality and safety. Kinematic redundancy is exploited to optimize one or more performance indices of interest for aerostructures assembly, as well as to respect all the typical constraints that characterize such applications.

Finally, as highlighted in [6], industrial robots are often programmed by using the robot-specific teach pendant, which is a very slow and not efficient solution and is not suitable especially for mobile robots moving in a dynamic environment. Handling redundancy allows to define tasks directly in the workspace, pushing the programming interface to a higher level of abstraction, leading to greater flexibility and efficiency in the workcell management.

1.1 Motivation of the paper

The case study of this paper comes from the European project LABOR (Lean robotized AssemBly and cOntrol of composite aeRostructures) [7]. Its objective is to build an automated solution for the assembly process of fuselage parts, such as skins, stringers, frames and door surround components, where drilling, sealing, fastening and inspection are performed by small/medium size robots, in replacement of the large and heavy robots that characterize the state of art in aeronautical machining cells.

A 3D reconstruction of the LABOR cell is provided in Figure 1. The panel is mounted on a rotating jig, that holds and orients the panel during the assembly operations performed by two cooperating six-axis robots mounted on the two sides of the panel, namely: the external and internal (with respect to the curvature of the panel) robot. The former performs drilling, sealing, fastening and inspection from the hole entry side while the latter performs the inspection from the hole exit side and applies a clamping force during the drilling phase. Each robot is mounted on a platform moving on a linear axis (the 7-th axis), allowing for the movement along the length of the panel. The combined movement of the robots, the slide and the jig allows to cope with the size of the panel which is much larger than the workspace of the two six-axis robots.

The nominal working sequence starts with the internal robot inspecting the area, performing the referencing and computing the drilling coordinates which are sent to the external robot. Then, the external robot starts drilling while the internal robot applies the counterthrust force. At the end of the drilling operations, the external robot inspects the drilled hole. Such operations are repeated for each hole of the sequence. Once all the holes have been drilled, the external robot mounts the sealing and fastening tool and goes back to the first hole of the sequence to start sealing and fastening. At the end, if it is required, the internal robot performs the inspection of the fastened holes. The work to be performed on every hole must not exceed 30 s (excluding after-fastening inspection) in order to respect the overall cycle time for the whole panel.

The current setup foresees that the trajectories tracked by the robot during the assembly operations (e.g. from one hole to the other) are directly assigned in the joint space, by keeping the jig and slide fixed. In particular, jig-slide positions are found corresponding to best working areas for the robots to improve the quality of the assembly operations. These are found through some heuristics such as placing the slide right in front of the hole with the robot tool close to the base and the arm less elongated. This way, the redundancy introduced by the presence of the slide is not exploited, resulting in several shortcomings.

In the current setup, holes are in vertical sequences, such that the slide is not moved during the operations on a single sequence. This limits the performances, preventing to efficiently operate on different hole patterns which are needed for some specific panel areas, e.g. doors, windows. Since large and geometrically complex tools are mounted at the robot end-effector, collisions with the panel and with the robot itself can easily occur. Hence the system must be equipped with collision avoidance algorithms, which are even more important when human operators access the cell during the working phase. In addition, the interaction with the panel might not be stable, since slippage and mechanical deviations may occur. Also, the time constraints imposed by the process have to be respected, as well as joint limits imposed by the robot manufacturer.

Our goal is to deal with all these aspects by planning trajectories that allow for more complex hole pattern geometries, avoid unnecessary robot movements through minimum joint displacements, prevent dangerous robot configurations through collisions checking, increase stability, by stiffness maximization, during drilling, while respecting joint limits and being compliant with the available planning time. The joint space configurations are computed by simply defining the task in the workspace (e.g. the position and orientation coordinates of the hole to be drilled) and then optimizing, in the allotted time and in a global manner, the postures that the robot has to assume to make the end-effector reach the assigned positions.

Trajectories are optimized using the approach proposed in [8] which is based on a dynamic programming (DP) algorithm for planning robot trajectories in the joint space, exploiting kinematic redundancy, in order to satisfy additional requirements and effectively increase the efficiency and the flexibility of the whole system. The slide will not be kept fixed, but its motion will be planned as part of the optimization process, treating it as an additional joint to achieve more efficient configurations.

In Section 2, we recall the notion of kinematic redundancy and present the dynamic programming approach, analyzing the technique of the force ellipsoids for the stiffness maximization. Then, in Section 3, experimental results are provided, comparing them with the traditional approach. At the end, in Section 4, conclusions and possible future developments are discussed.

2 Problem formulation

2.1 Redundancy resolution

A manipulator is defined as *kinematically redundant* when the number m of task constraints is lower than the number n of degrees of freedom provided by the manipulator's kinematic chain. $r = n - m$ is termed *degree of redundancy*.

Let $\mathbf{q} = [q_1\ q_2 \dots q_n]^T$ be the $n \times 1$ vector of joint positions representing the configuration of the manipulator and $\mathbf{x} = [\mathbf{p}\ \boldsymbol{\phi}]^T$ the $m \times 1$ vector of task position $\mathbf{p}$ and orientation $\boldsymbol{\phi}$ expressing the end-effector frame $\mathcal{T}_e$ coordinates with respect to the base frame $\mathcal{T}_b$. Considering a task described by six variables, the position is $\mathbf{p} \in \mathbb{R}^3$ and the orientation $\boldsymbol{\phi}(\mathbf{R}) \in \mathbb{R}^3$ is expressed through the set of Euler angles [9] extracted from the 3×3 rotation matrix $\mathbf{R} \in SO(3)$ from $\mathcal{T}_b$ to $\mathcal{T}_e$. The mapping from the joint space to the task space is performed through the non-linear vectorial function $\mathbf{k}: \mathbb{R}^n \to SE(3)$, where $SE(3) = \{(\mathbf{p}, \mathbf{R}): \mathbf{p} \in \mathbb{R}^3, \mathbf{R} \in SO(3)\} = \mathbb{R}^3 \times SO(3) = \mathbb{R}^m$. The direct kinematic equation, representing the path constraint, is expressed as

$$\mathbf{x}(t) = \mathbf{k}(\mathbf{q}(t)), \tag{1}$$

where $t \in [0, T]$ denotes the time and T is the trajectory duration.

When the task is assigned in the task space, the kinematic equation (1) has to be inverted in order to find the joint positions allowing to fulfill such a task, that is

$$\mathbf{q}(t) = \mathbf{k}^{-1}(\mathbf{x}(t)). \tag{2}$$

For a redundant robot, the inverse kinematics problem in (2) admits, in general, an infinite set of solutions, i.e. infinite joint positions that keep the end-effector motionless. This means that it is possible to optimize across such solutions to achieve other objectives, besides respecting the task constraint. This optimization process is usually referred to as *redundancy resolution*.

According to [10], the infinite set of solutions can be parametrized with r functions of the joint positions. Let us call the vector of these functions $\mathbf{u}$ and add it to the direct kinematic equations $\mathbf{k}$, so as to obtain:

$$\begin{bmatrix} \mathbf{x}(t) \\ \mathbf{u}(t) \end{bmatrix} = \begin{bmatrix} \mathbf{k}(\mathbf{q}(t)) \\ \mathbf{k}_u(\mathbf{q}(t)) \end{bmatrix} = \mathbf{k}_a(\mathbf{q}(t)) \tag{3}$$

where $\mathbf{k}_u: \mathbb{R}^n \to \mathbb{R}^r$ is the forward kinematics of some joint combinations and $\mathbf{k}_a$ is the *augmented kinematics*. By differentiating (3), we obtain:

$$\begin{bmatrix} \dot{\mathbf{x}}(t) \\ \dot{\mathbf{u}}(t) \end{bmatrix} = \begin{bmatrix} \mathbf{J}(\mathbf{q}(t)) \\ \mathbf{J}_u(\mathbf{q}(t)) \end{bmatrix} \dot{\mathbf{q}}(t) = \mathbf{J}_a(\mathbf{q}(t))\dot{\mathbf{q}}(t) \tag{4}$$

where $\mathbf{J} = \frac{\partial \mathbf{k}}{\partial \mathbf{q}}$ is the task Jacobian, $\mathbf{J}_u = \frac{\partial \mathbf{k}_u}{\partial \mathbf{q}}$ is the redundancy parameter Jacobian and $\mathbf{J}_a = \frac{\partial \mathbf{k}_a}{\partial \mathbf{q}}$ is the Jacobian matrix of the augmented kinematics. The problem (3) is squared and can be inverted out of singularities, when $\mathbf{u}$ is given. In the most simple case, $\mathbf{u}$ can be made of r joint positions, whose selection, however, is not trivial. For certain tasks, the manipulator may still be redundant (and present infinite inverse kinematics solutions), even though r joints are fixed. In such cases, the selected joints are not representative of the redundancy space, i.e. the null space of the Jacobian $\mathcal{N}(\mathbf{J})$, and $\mathbf{J}_a$ is rank-deficient for some trajectory point. Therefore, we must ensure that

$$\mathrm{rank}(\mathbf{J}_a) = n \tag{5}$$

for each trajectory point. This requires to choose the redundant joints such that

$$\mathcal{R}(\mathbf{J}^T) \cap \mathcal{R}(\mathbf{J}_u^T) = \emptyset \tag{6}$$

where $\mathcal{R}(\mathbf{M})$ represents the range space of a generic matrix $\mathbf{M}$ [10].

A solution that satisfies (6) is not easy to find analytically, especially for complex robots. Typically, in practice, the choice is made empirically, depending on the experience of the programmer. In our case, it can be verified a posteriori, numerically or through the graphical representation of the null space that the dynamic programming approach itself provides. If the joints are correctly selected, a finite number of solutions to the inverse kinematic problem is retrieved by inverting (3). In particular, the number of solutions depends on the robot type (i.e. planar, regional, spherical, spatial) and on the imposed constraints.

As will be clear in Section 2.2, the Jacobian is only used to verify the representativeness of the redundant joints, since the first order kinematics is not needed. Operating at joint position level is an important characteristic of the dynamic programming approach, resulting to be immune to singularities.

2.2 Redundancy optimization with dynamic programming

In [8], redundancy resolution is addressed through discrete dynamic programming. In this paper, we briefly recall this framework and extend it to the specific objectives and constraints that characterize the assembly of aerostructures in the LABOR project.

In the case of the LABOR cell, where the end-effector tools must have a specific orientation due to their shape and volume, the task variables are always six ($m = 6$), even for drilling, which is usually described by only five variables [11]. Given a six-axis robot mounted on an additional linear axis ($n = 7$), we thus have $r = 1$. In this paper, we provide a formulation for this particular case, but the reader may realize that it can be easily extended to cases where $r > 1$.

Let us consider the trajectory $\mathbf{x}(t)$, and discretize t in its domain with $N_i + 1$ samples, with sampling interval $\tau = \frac{T}{N_i}$. Then, let us parametrize the redundancy by joint selection, so that $\mathbf{u} = u = q_i$, where i is the i-th joint (the selected one). We discretize u with $N_j + 1$ samples in its physical domain that depends on joint limits.

The augmented forward kinematics (3) can then be inverted in this discrete domain, for each single sample of $\mathbf{x}(t)$ and $u(t)$:

$$\mathbf{q}_{j,g}(i) = \mathbf{k}_a^{-1}\big(\mathbf{x}(i), u_j(i)\big) \tag{7}$$

where i and j are the indices that span the samples of the time and the redundancy parameter respectively, and g=1,...,N_g is the index accounting for the presence of multiple inverse kinematic solutions when the redundancy parameter is given.

As mentioned in Section 1, the joint configurations and their derivatives must satisfy joint limits (position and velocity) and avoid self-collisions and collisions with the surrounding environment. Joint limits are formalized as follows:

$$\mathbf{q}_{\min} \leq \mathbf{q}(i) \leq \mathbf{q}_{\max} \tag{8}$$

$$\dot{\mathbf{q}}_{\min} \leq \dot{\mathbf{q}}(i) \leq \dot{\mathbf{q}}_{\max} \tag{9}$$

Collision constraints are checked referring to the geometric shapes [12] of each robot joint $S(q_j(i))$ and of the environment S_e, in such a way that the following relationships are always verified:

$$S\big(q_j(i)\big) \cap S(q_k(i)) = \emptyset \ \forall j, k = 1, \ldots, n \ \text{ with } \ j \neq k \tag{10}$$

$$S\big(q_j(i)\big) \cap S_e = \emptyset \ \forall j = 1, \ldots, n \tag{11}$$

Thus, we can define the set $\mathcal{A}_i$ of admissible $\mathbf{q}$ at waypoint i which takes the role of accepting only those configurations satisfying (8), (10) and (11). Similarly, the joint velocity limits $\dot{\mathbf{q}}$ can be accounted for with the set $\mathcal{B}_i(\mathbf{q}(i))$ which, in general, is time-dependent, as well as state dependent, i.e.

$$\begin{aligned} \mathcal{A}_i &= \{\mathbf{q}(i) : (8), (10), (11) \text{ hold}\} \\ \mathcal{B}_i &= \left\{ \begin{aligned} &\dot{\mathbf{q}}(i) = \frac{\mathbf{q}(i) - \mathbf{q}(i-1)}{\tau} : \\ &\mathbf{q}(i) \in \mathcal{A}_i, \mathbf{q}(i-1) \in \mathcal{A}_{i-1}, (9) \text{ holds} \end{aligned} \right\} \end{aligned} \tag{12}$$

where the backward Euler approximation has been used for discrete-time derivatives.

Once $\mathbf{q}_{j,g}(i)$ is available for each single value of i, j and g, the objective is to find the optimal sequence of inputs that minimizes or maximizes a given cost function. Let us consider a generic cost function I that is computed incrementally by summing up the local costs l for each i:

$$I(N_i) = \psi(\mathbf{q}(0)) + \sum_{i=1}^{N_i} l(\mathbf{q}(i), \mathbf{q}(i-1)) \tag{13}$$

where l is assumed to be a function of the joint positions and their derivatives and ψ is the cost of the initial configuration. It is typically set to zero, unless the application requires to associate an explicit cost to it.

Assuming that the robot can reach the first drilling position in a safe configuration, far from collisions, the objective is to minimize the joint displacements, so as to avoid unnecessary risky movements [13]:

$$l(\mathbf{q}(i), \mathbf{q}(i-1)) = \sum_{k=0}^{n} |q_k(i) - q_k(i-1)| \tag{14}$$

where k is the index spanning the joint position variables.

Now we can rewrite the objective function (13) in a recursive form and minimize over the possible configurations $\mathbf{q}$, i.e.

$$\begin{aligned} &I(0) = \psi(\mathbf{q}(0)) \\ &I_{\text{opt}}(i) = \min_{\mathbf{q}_{j,g} \in \mathcal{C}_{i-1}} [l(\mathbf{q}(i), \mathbf{q}(i-1)) + I(i-1)] \end{aligned} \tag{15}$$

where $\mathcal{C}_{i-1}$ is the set of admissible $\mathbf{q}_{j,g}$ in $\mathcal{A}_{i-1}$ that also respect constraints on the derivative defined by the set $\mathcal{B}_i$. $I_{\text{opt}}(i)$ is termed *optimal return function*, which is the minimum value of the objective function if the process started at stage i, thus $I_{\text{opt}}(N_i)$ will be the optimized function.

2.3 Force ellipsoids

The dynamic programming setup described in Section 2.2 allows to compute an optimal solution for each sample of the redundancy parameter u_j and inverse kinematic solution g at the last stage N_i. The repetition of the recursion in (15) up until the last stage allows retrieving the globally-optimal solution for the given discretization of the domains. However, as discussed in Section 1, besides ensuring safe motions, we would like to guarantee stable drilling operations. Thus, among the safe trajectories that minimize the joint displacements, we choose the one that ends in the stiffest configuration. This selection is based on the analysis of the force ellipsoids.

The force ellipsoid represents the force transmission efficiency generated by the set of torque vectors with norm equal to one when the manipulator is in a given configuration [14]:

$$\boldsymbol{\tau}^T \boldsymbol{\tau} \leq 1 \Rightarrow \mathbf{f}^T \mathbf{J}\mathbf{J}^T \mathbf{f} \leq 1 \tag{16}$$

where $\boldsymbol{\tau}$ is the $n \times 1$ vector of actuation torques and $\mathbf{f}$ is the $m \times 1$ vector of forces and torques at the end-effector. The relationship $\boldsymbol{\tau} = \mathbf{J}^T \mathbf{f}$ has been used in the equation above, while the dependence of $\mathbf{J}$ on $\mathbf{q}$ has been omitted.

The shape of the ellipsoid is described by the eigenvectors $\mathbf{v}$ and the eigenvalues $\boldsymbol{\lambda}$ of the $m \times m$ matrix $\mathbf{A} = \mathbf{J}\mathbf{J}^T$. With reference to Figure 2, the eigenvectors indicate the orientation of the ellipsoid's axes with respect to the reference frame of the Jacobian and the reciprocals of the square roots of the eigenvalues represent the length of the semi-axes.

Assuming that the end-effector frame is aligned to the task frame in such a way that the z axes are opposite and the x axes are aligned, as in Figure 3, the objective is to maximize the force capacity along the z axis, i.e. the drilling direction. As highlighted in [15], the best performances would be achieved if the ellipsoid's major axis and the direction of interest (z in our case) had the same orientation. However, this is a difficult condition to obtain due to collisions and kinematic constraints. As a consequence, if $\mathbf{J}$ is computed with respect to the end-effector frame, we maximize the distance between the center of the frame, i.e. the center of the ellipsoid, and the intersection between the ellipsoid surface and the z axis (the distance represented in yellow in Figure 2). This distance is given by

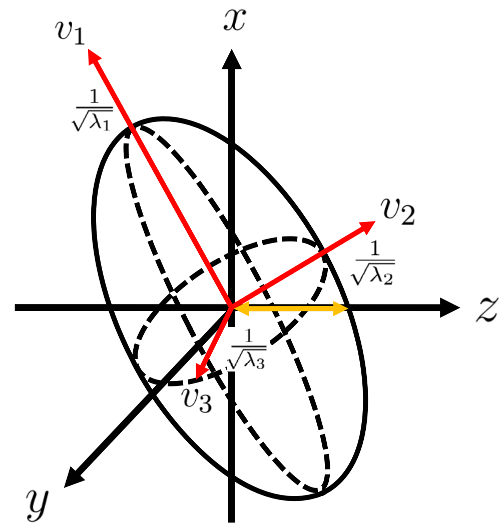

Fig. 2. Force ellipsoid representation.

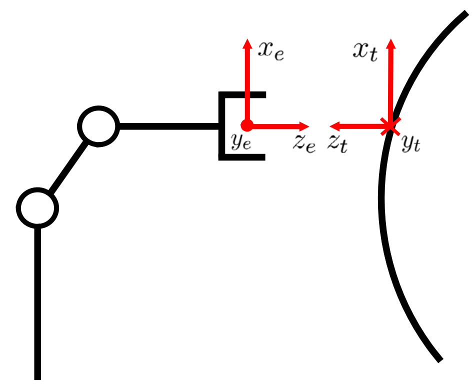

Fig. 3. End-effector and task frames.

the components of the $\mathbf{J}\mathbf{J}^T$ matrix selected through the vector $\boldsymbol{\eta}$, corresponding to the direction along which the stiffness has to be maximized.

All the valid joint configurations at the last waypoint are evaluated and the one with the maximum stiffness is retrieved by using the *Manipulator Mechanical Advantage* (MMA) index [16], i.e.

$$\mathbf{q}(N_i) = \underset{\mathbf{q}_{j,g} \in \mathcal{C}_{N_i}}{\arg\max} \left[\left(\boldsymbol{\eta}^T \mathbf{J}\mathbf{J}^T \boldsymbol{\eta} \right)^{-1/2} \right] \tag{17}$$

This way, the only admissible configuration at the last stage is the stiffest one $\mathbf{q}(N_i)$. Since the Jacobian is expressed in the end-effector frame and we only consider the translational components, the $\boldsymbol{\eta}$ vector will be equal to $\boldsymbol{\eta} = [0\ \ 0\ \ 1\ \ 0\ \ 0\ \ 0]^T$, which corresponds to the z axis. It is worth remarking that (17) is a special case of the optimization problem in [17], obtained by setting the same compliance for all joints.

Recalling the optimization function (15) at the final stage N_i, we have that

$$I_{\text{opt}}(N_i) = \min_{\mathbf{q}_{j,g} \in \mathcal{C}_{N_i - 1}} [l(\mathbf{q}(N_i), \mathbf{q}(N_i - 1)) + I(N_i - 1)] \tag{18}$$

where $\mathbf{q}(N_i)$ is the stiffest configuration obtained by applying (17).

2.4 Algorithmic implementation

The algorithm in [8,18] has been modified to include the stiffness optimization on the last waypoint, as well as to consider the specific objective function and constraints that characterize the LABOR use case. Its pseudo-code is provided in Algorithm 1.

The algorithm works on N_g grids of size $N_i \times N_j$, whose cells (i, j) represent possible configurations $\mathbf{q}$ at which the robot can be at the corresponding stage i. For each cell, a transition is evaluated towards all the cells at the next stage, i.e. $i+1$: constraints are checked and, if satisfied, the local cost l and the cumulative cost I are computed and saved. The optimal transition is the one returning the minimum cumulative cost.

Once all the costs have been computed for the last stage N_i, the stiffness of each enabled configuration at this stage is computed. The node with the maximal stiffness is selected and, starting from such configuration, the entire trajectory is built backwards, following the predecessors' list.

It is worth noticing that the grids represent the null space for the entire trajectory and their graphical representation through colored maps [8] is used for the a posteriori verification of the redundant parameter representativeness, as mentioned in Section 2.1.

3 Experimental results

Algorithm 1 has been implemented in ROS (Robot Operating System) in order to reuse the available modules to plan and visualize trajectories in the task space and to simulate the motion in the *RViz* virtual environment and assess the stiffness optimization. ROS has also been used to connect the DP planner to the *CoppeliaSim* simulator in order to command the Fanuc M20iA/35M model in the 3D scene with the LABOR panel.

The position and velocity limits that have been used in the algorithm are extracted from the official Fanuc datasheet and reported in Table 1 for the sake of clarity.

Algorithm 1 Discrete DP redundancy resolution algorithm with stiffness optimization.

Initialize $\mathcal{A}_i, \forall i = 0..N_i$
Initialize $\mathcal{B}_i, \forall i = 1..N_i$
Initialize $\mathcal{C}_i = \oslash, \forall i = 0..N_i$
Initialize costs $I_{i,j,g} = +\infty, \forall i = 1..N_i, \forall j = 0..N_j, \forall g = 1..N_g$
Initialize costs $I_{0,j,g} = 0, \forall j = 0..N_j, \forall g = 1..N_g$
$C_0 \leftarrow \mathcal{A}_0$
for $i \leftarrow 0$ to $N_i - 1$ **do**
  for each $\mathbf{q}_{j,g} \in \mathcal{C}_i$ **do**
    for each $\mathbf{q}_{k,h} \in \mathcal{A}_{i+1}$ **do**
      $\dot{\mathbf{q}} \leftarrow \frac{\mathbf{q}_{k,h} - \mathbf{q}_{j,g}}{\tau}$
      if $\dot{\mathbf{q}} \in \mathcal{B}_{i+1}$ **then**
        $\mathcal{C}_{i+1} \leftarrow \mathcal{C}_{i+1} + \{\mathbf{q}_{k,h}\}$
        Compute local cost function l
        if $I_{i,j,g} + l < I_{i+1,k,h}$ **then**
          $I_{i+1,k,h} \leftarrow I_{i,j,g} + l$
          Set $\mathbf{q}_{j,g}$ *at* i *as predecessor of* $\mathbf{q}_{k,h}$ *at* $i+1$
$s_{max} \leftarrow -\infty$
for each $\mathbf{q}_{j,g} \in \mathcal{C}_{N_i}$ **do**
  Compute the stiffness $s_{j,g} \leftarrow (\boldsymbol{\eta}^T \mathbf{J}(\mathbf{q}_{j,g}) \mathbf{J}^T(\mathbf{q}_{j,g}) \boldsymbol{\eta})^{-1/2}$
  if $s_{j,g} > s_{max}$ **then**
    $s_{max} \leftarrow s_{j,g}$
    $\overline{\mathbf{q}} \leftarrow \mathbf{q}_{j,g}$
$I_{opt}(N_i) \leftarrow I_{N_i,j,g}$, with $j, g : \mathbf{q}_{j,g}(N_i) = \overline{\mathbf{q}}$
Build the sequence of configurations $\mathbf{q}(i)$ *starting from* $\mathbf{q}_{j,g}(N_i)$ *and going backwards in the predecessors list*

Table 1. Fanuc M20iA/35M joint limits.

	Joint 1	Joint 2	Joint 3	Joint 4	Joint 5	Joint 6	Slide joint
$q_{\max}$	−3.225 rad	−1.7553 rad	−3.225 rad	−3.49 rad	−2.4435 rad	−7.854 rad	−2.1 m
$q_{\min}$	3.225 rad	2.7925 rad	4.8171 rad	3.49 rad	2.4435 rad	7.854 rad	2.1 m
$\dot{q}_{\max}$	3.14 rad/s	3.14 rad/s	3.49 rad/s	6.11 rad/s	6.11 rad/s	6.98 rad/s	9.6 m/s

Table 2. Time estimated for automatic operations on a CFRP and thermoplastic compound panel with 1500 holes using 9 mm grip Hi-lite fasteners.

Assembly operations	Percentage of time	Per hole
Drilling: 3.1 mm diameter hole	0.07	2.04 s
Diameter increasing from 3.1 to 4.0 mm	0.06	1.93 s
Diameter increasing from 4.0 to 4.8 mm	0.06	1.93 s
Countersinking	0.12	3.54 s
Sealing and riveting	0.55	16.38 s
Inspection	0.14	4.19 s
Total time	1.00	30 s

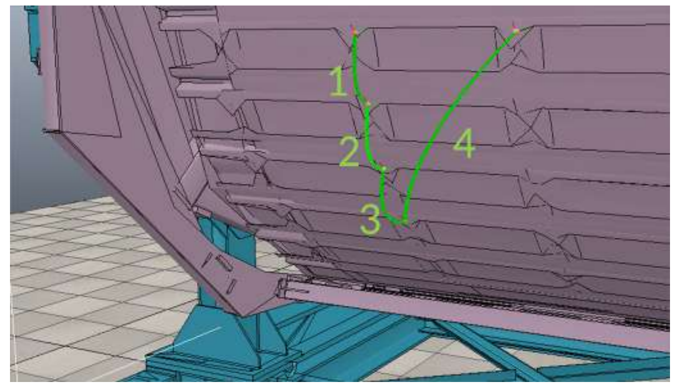

Fig. 4. Four task-space trajectories in the CoppeliaSim simulation environment.

3.1 Time requirement

The dynamic programming algorithm presented in Section 2.2 is usually employed for off-line applications [8,13,19,20] because of the computational effort required to find the optimal solution. While the algorithm is far from being applied in scenarios requiring real-time planning, in some circumstances, it is suitable to plan trajectories while the robot already moves or interacts with the workpiece. In the LABOR project, the trajectories cannot be completely pre-planned because they are subject to the referencing operations performed by the internal robot, that provides the initial drilling position of a known pattern. However, at each position in the pattern, the robot stops to perform the task of interest (drilling/sealing/fastening) and this time can be used to plan the next hole-to-hole trajectory in the pattern in an optimal way: the trajectory optimization process must not exceed the time for drilling and sealing/fastening operations. Here we analyze what, in the LABOR project, these time requirements are, thus providing an upper bound for the DP algorithm to complete before the external robot needs to move to the next hole.

The estimation is based on the requirement that the cycle time is 30 s per hole (considering drilling, countersinking, hole inspection, sealing, fastener insertion and not considering fastener inspection), but such a time is not allocated to specific tasks. Thus, we make the simplifying assumption that the distribution of time across the several tasks is the same as manual operations. We consider the time needed for the manual installation of 9 mm grip Hi-lite fasteners for 1500 holes in a CFRP and thermoplastic compound panel, and keep the same time percentages for the automatic assembly. The results are shown in Table 2.

In particular, the drilling time results to be equal to 13.62 s (considering all the operations except sealing and riveting) and the fastening time is equal to 16.38 s (considering only sealing and riveting). As a consequence, the planning for each hole-to-hole trajectory has to be completed within the minimum of such times.

3.2 Planned trajectories

Simulations have been performed by planning four hole-to-hole trajectories for five drilling points, by keeping the orientation fixed. Such trajectories are longer than the real ones to highlight some characteristics of the optimization process that we will discuss next. The trajectories are shown in Figure 4, and the parameters used for planning are reported in Table 3. The initial position for the first trajectory is not known so it is computed as a result of the optimization process, while, for the others, the initial position must correspond to the final position of the previous trajectory.

The slide position has been empirically selected as redundancy parameter and, as discussed in Section 2.1, an a posteriori verification is performed to be sure that the condition (5) holds for all waypoints. The *slide resolution* in Table 3 indicates the minimum displacement of the slide joint in its discrete domain and has been selected as a result of the trade-off between optimization quality and execution time: the higher the resolution is, the closer the solution will be to the global optimum. Like many other six-axis industrial robots, even for the Fanuc M20iA/35M, it is $N_g = 8$ although, due to constraints, the number of admissible inverse kinematics solutions may be lower.

The execution of the four trajectories of Figure 4 in CoppeliaSim is shown in [21]: unlike the current planning policy, the DP algorithm makes the slide move to minimize

Table 3. DP solver parameters for trajectories 1–4. Planning times are related to the execution of the algorithm on a virtual machine with a single-threaded implementation.

	Trajectory	Waypoints (N_i)	Length (mm)	Slide resolution (mm)	Duration (T) (s)	Planning time (s)
1	1st to 2nd hole	10	288.5	13.2	0.55	27
2	2nd to 3rd hole	10	321.4	13.2	0.55	21
3	3rd to 4th hole	10	339.0	13.2	0.55	29
4	4th to 1st lateral hole	15	1060.0	13.2	0.55	24

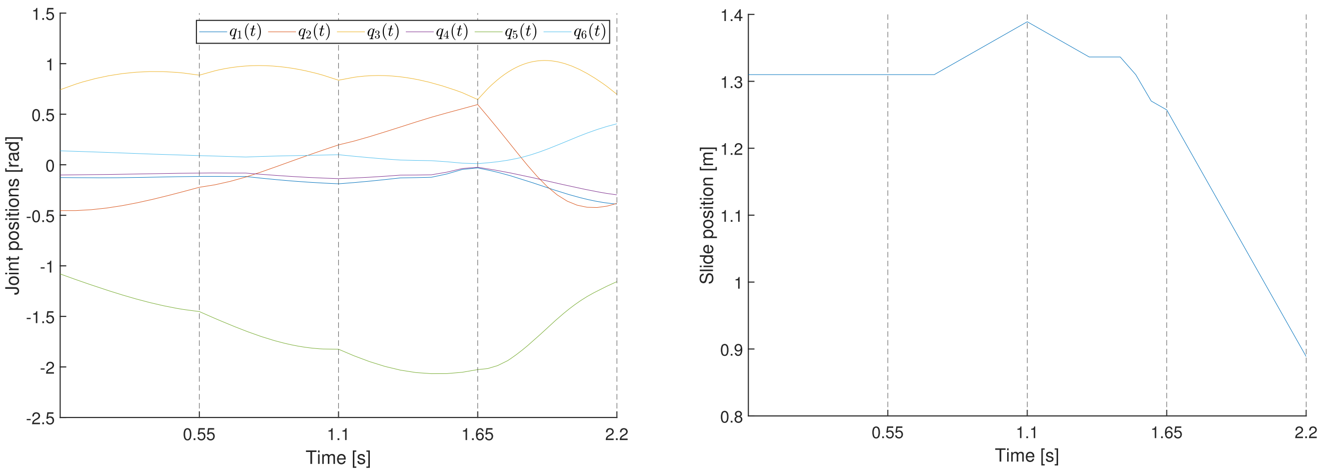

Fig. 5. Planned joint and slide positions for trajectories 1–4 plotted in sequence. The end of each trajectory is indicated with a dotted line.

the overall motion of the joints and to reach a stiff configuration at the end of each trajectory. It is important to remark that this is done by assigning the tasks directly in the task space. Joint limits and collisions are automatically checked and avoided. The planning time spans from 21 to 29 s for trajectories longer than 288 mm with 10/15 waypoints. The trajectories that are considered in the LABOR project are much shorter (25.4 mm), being the points in the pattern much closer. By keeping the same trajectory resolution, we would only need 3 waypoints to describe such trajectories. Since the computation time scales linearly with the number of waypoints, we should expect the planning time to be equal to about 8 s, respecting the upper bound of 13.62 s as estimated above. Plots of planned joint space trajectories against time are provided in Figure 5.

3.3 Stiffness analysis

Now let us make a deeper analysis on the stiffness considering the 4th trajectory. In Figure 6 (left), the force ellipsoid for the last position (the working pose) is plotted in RViz. Here the red, green and blue vectors are the ellipsoid's semi-axes, while the yellow vector represents the distance between the center of the tool frame and the ellipsoid surface, to be maximized. The stiffest configuration is the one having the yellow vector aligned with the major axis of the ellipsoid, but kinematic constraints and collisions may prevent to reach such a condition. For the 4th trajectory, the resulting MMA is equal to 1.099. Details on the direction and length of each axis with respect to the tool frame (as the one represented in Figure 3) are reported in Table 4. It is worth noticing that the robot is slightly placed on the left of the working point, while the ellipsoid is quite oblique. In fact the y component of the major semi-axis (the red one) is equal to -0.0825 while its z component is almost aligned with the z axis of the tool frame, i.e. -0.9008. Hence, it is intuitive to conclude that stiffer configurations may exist.

Let us repeat the experiment by considering a slower end-effector trajectory (from 0.55 to 1.4 s), so that the robot will have more time to move its kinematic structure without violating joint velocity and acceleration limits. The final configuration is shown in Figure 6 (right), together with the force ellipsoid. In this case the MMA is equal to 1.127, which is higher than the MMA obtained with a faster trajectory. The related ellipsoid's parameters are reported in Table 5. We can notice that the ellipsoid is more elongated and its major semi-axis is better aligned with the drilling direction, resulting in a stiffer posture. The y component is perfectly aligned with the corresponding axis of the tool frame and its length is also higher (1.8 instead of 1.7629).

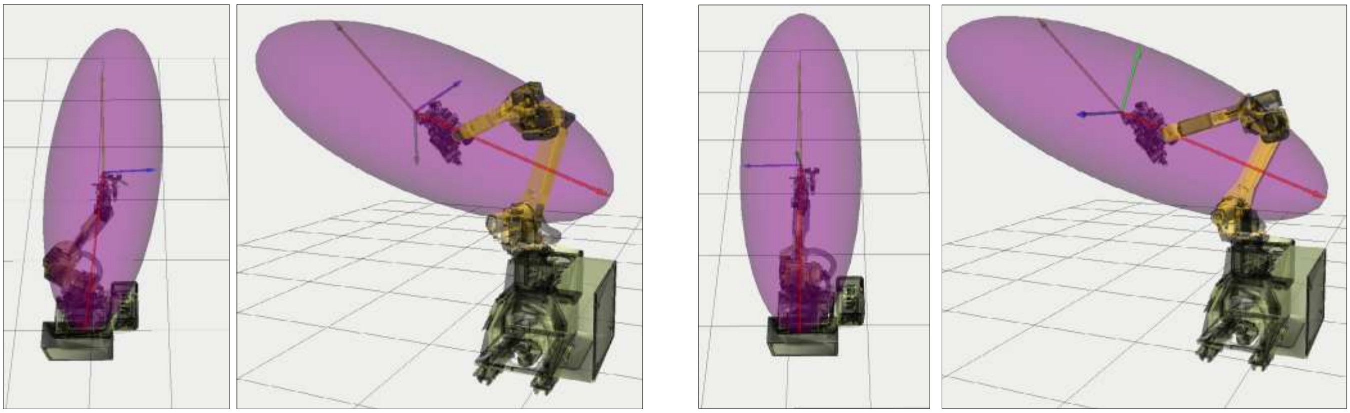

Fig. 6. Frontal and lateral view of the force ellipsoid of the last position of the 4th trajectory, planned with a trajectory duration of 0.55 s (left) and 1.4 s (right).

Table 4. Parameters of the ellipsoid resulting from the planning of the 4th trajectory with duration 0.55 s, expressed with respect to the tool frame.

Axis	Eigenvector			Length
	x	y	z	$(1/\sqrt{\lambda})$
Red axis	0.4262	−0.0825	−0.9008	1.7629
Green axis	−0.8127	0.4025	−0.4214	0.5726
Blue axis	0.3973	0.9117	0.1045	0.6608

Table 5. Parameters of the ellipsoid resulting from the planning of the 4th trajectory with duration 1.4 s, expressed with respect to the tool frame.

Axis	Eigenvector			Length
	x	y	z	$(1/\sqrt{\lambda})$
Red axis	0.4193	0.001	−0.9079	1.8
Green axis	0.9077	−0.0183	0.419	0.5743
Blue axis	−0.0161	−0.9998	−0.008	0.6613

A comparison between the two trajectories is provided in [22]: in the second trajectory the robot is obviously slower but this allows reaching a stiffer final posture.

Hence, depending on the assigned parameters and the trajectory characteristics, the joint-space trajectory will change, allowing the robot to adapt to different situations and scenarios.

3.4 Comparative results

As explained in Section 1.1, the traditional approach is based on the heuristics of fixing the slide in a position which should lead to the stiffest manipulator configuration. According to it, in the case of the first three trajectories of Table 3, the slide is placed in front of the vertical hole sequence and the joint space trajectory is found. We remark that no optimization occurs in this case, as the inverse kinematics problem is squared. In terms of both MMA and joint displacements, the two techniques provide similar results, as Figure 7 and Table 6 testify.

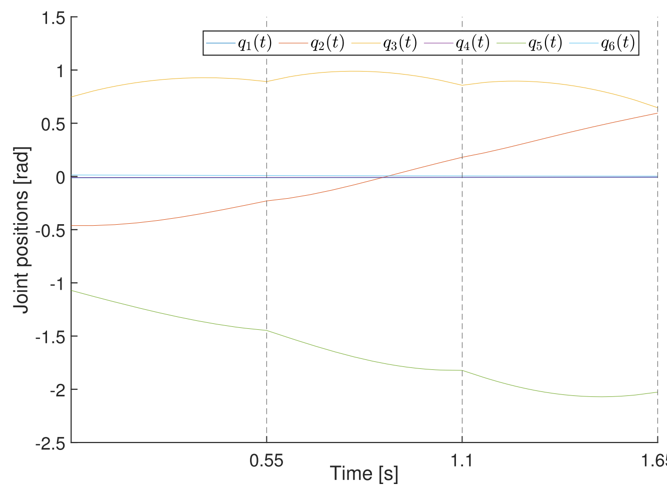

Fig. 7. Planned joint positions with fixed slide for the trajectories 1–3 plotted in sequence. The end of each trajectory is indicated with a dotted line.

Table 6. MMA values obtained from the dynamic programming algorithm moving the slide and from the heuristics by fixing the slide position.

Trajectory	Moving slide	Fixed slide
1	0.922	0.922
2	0.819	0.819
3	0.741	0.741

Now, let us consider the 4th trajectory again, which is a lateral motion. This task cannot be achieved by fixing the slide, as the path exits the manipulator's workspace. In the current LABOR setup, as shown in [23], the robot returns to its home position, the slide moves in front of the lateral hole, then the robot arm moves to the drilling position. Alternatively, inverse kinematics could be solved for the last hole, assuming the slide already be in front of it: two point-to-point motions are planned for both the slide and the arm, commanded separately, and executed at the same time. Regardless of the time difference of the two solutions, either strategy does not guarantee any control over the end-effector motion, resulting in a safety issue. On the contrary, in the proposed DP technique, the path is defined in the workspace and the movements of both the arm and the slide are planned together: a collision-free safe motion of both the end-effector and the whole kinematic chain is guaranteed, together with a final posture that is at least as stiff as the one obtained with the traditional approach.

In general, it should be expected that the benefits of the proposed techniques are much more evident when the assembly operations require lateral motions along the fuselage panel or coverage or more complex geometries. For instance, let us consider the assembly operations around a window of the fuselage. In [23], we show what the movement of the arm and the slide would be if the trajectories from one hole to the other, along the window perimeter, were planned with the proposed DP algorithm. The slide would follow the manipulator for each hole to be drilled so as to minimize the global joint motion and allows for less elongated postures of the arm when reaching lateral holes. On the contrary, by fixing the slide position, the manipulator must elongate to reach all the holes, to the detriment of stiffness. In addition, due to the higher joint displacements, the time required to execute the path is about three times higher than dynamic programming.

4 Conclusions

Robotized solutions in large industrial plants are typically characterized by the presence of slides on which robots are mounted to increase their workspace. This leads to the introduction of kinematic redundancy which, however, is not efficiently handled and not exploited to satisfy typical requirements of aerospace manufacturing that are very demanding and sometimes not achievable by the common industrial robots. An example of such solutions is given by the LABOR project which provides a system to make autonomous assembly operations of fuselage panels by using two cooperating robots placed on slides. Since strict safety, stability, accuracy and efficiency requirements exist, we proposed a methodology that retrieves optimized trajectories by exploiting the kinematic redundancy provided by the system itself. Joint space trajectories that satisfy the requirements above are generated in the allotted planning time. In particular, we planned safe motions for the robots by minimizing the joint displacements, and maximizing the stiffness at the working pose. At the same time, we avoided collisions, self-collisions and joint limits. We employed a discrete dynamic programming algorithm, characterized by a high degree of flexibility and adaptability to different scenarios. This is the main strength of the proposed technique as it allows to tackle different situations with different robots, trajectories and panels, by only changing, for example, the cost function and the constraints. Moreover, a suitable parametrization of the algorithm allows to achieve the desired performance and comply with the time requirements.

We have seen that the LABOR cell is provided with two robots working together to perform assembly operations. We expect that the workcell efficiency can be further improved if trajectories were jointly planned for the two robots at the same time. It is, therefore, our plan to extend the framework to cooperating scenarios, which will be the subject of future research.

Acknowledgments. This work has been funded by the European Commission under the CleanSky 2 project LABOR (GA n. 785419), with Leonardo S.p.A. as Topic Manager.

References

1. E. Laudante, A. Greco, M. Caterino, M. Fera, Human robot interaction for improving fuselage assembly tasks: a case study, Appl. Sci. **10** (2020) 5757
2. A. Bruni, E. Concettoni, C. Cristalli, M. Nisi, Smart inspection tools in robotized aircraft panels manufacturing. In: *Proceedings of the IEEE 5th International Workshop on Metrology for AeroSpace (MetroAeroSpace), Torino, Italy*, 2019, p. 649–654
3. K. Zhou, G. Ebenhofer, C. Eitzinger, U. Zimmermann, C. Walter, J. Saenz, L.P. Castano, M.A.F. Hernandez, J.N. Oriol, Mobile manipulator is coming to aerospace manufacturing industry. In: *Proceedings of the IEEE International Symposium on Robotic and Sensors Environments (ROSE), Timisoara*, 2014, p. 94–99
4. A. Campomaggiore, M. Costanzo, G. Lettera, C. Natale, A fuzzy inference approach to control robot speed in human-robot shared workspaces. In: *Proceedings of the 16th International Conference on Informatics in Control, Automation and Robotics, SCITEPRESS – Science and Technology Publications*, 2019, p. 78–87
5. M. Costanzo, G.D. Maria, G. Lettera, C. Natale, D. Perrone, A multimodal perception system for detection of human operators in robotic work cells. In: *Proceedings of the IEEE International Conference on Systems, Man and Cybernetics (SMC), Bari, Italy*, 2019, p. 692–699
6. D. Massa, M. Callegari, C. Cristalli, Manual guidance for industrial robot programming, Ind. Robot. **42** (2015) 457–465
7. The LABOR project. www.labor-project.eu
8. E. Ferrentino, P. Chiacchio, On the optimal resolution of inverse kinematics for redundant manipulators using a topological analysis, J. Mech. Robot. **12** (2020) 3
9. B. Siciliano, L. Sciavicco, L. Villani, G. Oriolo, Robotics-Modelling, Planning and Control (Springer-Verlag, London, 2009)
10. E. Ferrentino, P. Chiacchio, Redundancy parametrization in globally-optimal inverse kinematics. In: Advances in Robot Kinematics 2018, Springer International Publishing, 2018, 47–55

11. S. Garnier, K. Subrin, K. Waiyagan, Modelling of robotic drilling, Procedia CIRP **58** (2017) 416–421
12. M. Ahmadi, M. Jaber, F. Tang, High-performance multi-body collision detection for the real-time control of a CTS system, Trans. Can. Soc. Mech. Eng. **29** (2005) 163–177
13. A.P. Pashkevich, A.B. Dolgui, O.A. Chumakov, Multiobjective optimization of robot motion for laser cutting applications, Int. J. Comput. Integr. Manuf. **17** (2004) 171–183
14. T. Yoshikawa, Manipulability and redundancy control of robotic mechanisms. In: *Proceedings of the IEEE International Conference on Robotics and Automation, St. Louis, MO, USA*, 1985
15. A. Ajoudani, N.G. Tsagarakis, A. Bicchi, On the role of robot configuration in Cartesian stiffness control, in *Proceedings of the IEEE International Conference on Robotics and Automation (ICRA), Seattle, WA*, 2015, p. 1010–1016
16. R. Dubey, J.Y.S. Luh, Redundant robot control using task based performance measures, J. Robo. Syste. **5** (1988) 409–432
17. D. Busson, R. Bearee, A. Olabi, Task-oriented rigidity optimization for 7 DOF redundant manipulators, IFAC-PapersOnLine **50** (2017) 14588–14593
18. E. Ferrentino, P. Chiacchio, A topological approach to globally-optimal redundancy resolution with dynamic programming, in *ROMANSY 22 - Robot Design, Dynamics and Control, Springer International Publishing* (2018) 77–85
19. A. Dolgui, A. Pashkevich, Manipulator motion planning for high-speed robotic laser cutting, Inter. J. Produc. Resea, **47** (2009) 5691–5715
20. J. Gao, A. Pashkevich, S. Caro, Optimization of the robot and positioner motion in a redundant fiber placement workcell, Mechanism and Machine Theory **114** (2017) 170–189
21. F. Storiale, E. Ferrentino, P. Chiacchio. (2020). Redundancy resolution for joint displacements minimization and stiffness maximization, https://youtu.be/lorD5UEwsfs
22. F. Storiale, E. Ferrentino, P. Chiacchio. (2020). Redundancy resolution for stiffness maximization at the working pose, https://youtu.be/34hrGI5F12Q
23. F. Storiale, E. Ferrentino, P. Chiacchio. (2020). Redundancy resolution for stiffness maximization with large workspace and complex pattern geometries, https://youtu.be/yebIW6fVKLc

Cite this article as: Federica Storiale, Enrico Ferrentino, Pasquale Chiacchio, Planning of efficient trajectories in robotized assembly of aerostructures exploiting kinematic redundancy, Manufacturing Rev. **8**, 8 (2021)